University College London

Department of Physics & Astronomy

Black Hole Jet Simulation and Images

Research Thesis

Samuel Lai

Supervised by:
Dr. Ziri Younsi and Prof. Kinwah Wu

Degree Course:
MSc Astrophysics

August 21, 2019

Contents

1 Abstract

In April 10, 2019, The Event Horizon Telescope (EHT) released to the public a reconstructed image of the black hole at the center of galaxy M87 (M87*) with data gathered using sub-millimeter wavelength Very-Long Baseline Interferometry (sub-mm VLBI). In a series of six papers published to The Astrophysical Journal Letters, astronomers discussed the observation methods, image reconstruction procedure, geometric models of the image, comparison against simulation, and more. Simulations of black hole accretion dynamics are governed by general-relativistic magnetohydrodynamics (GRMHD), typically using the Advection-Dominated Accretion Flow (ADAF) model in the Radiatively Inefficient Accretion Flow (RIAF) regime. By combining data from GRMHD under Standard and Normal Evolution (SANE) with general-relativistic radiative transfer (GRRT), synthetic images of M87* were produced. The synthetic images discussed in the series of EHT papers use purely thermal electron distributions which are unable to reproduce the large-scale extended jet emission features observed for M87* at low frequencies. In this research thesis, I modify the GRRT code, BHOSS, to include non-thermal power-law emissivity and absoptivity. These electrons are inserted into the jet sheath region of the black hole accretion and synthetic images are produced. The differences between the purely thermal electron model and the hybrid model which includes a population of non-thermal electrons in the jet are investigated in this thesis. I also show that the hybrid distribution of electrons greatly increases the jet emission and enlarges the size of the radio image, while the thermal model has a brighter compact flux.

2 Introduction

2.1 Background

In 1915, Einstein published a set of equations describing the mutual interaction of the curvature of spacetime with mass and energy (Einstein, 1916). Today, this set of equations, known as the Einstein Field equations, can be written in condensed tensor form as

$$G_{\mu\nu} + \Lambda\, g_{\mu\nu} = \frac{8\pi G}{c^4} T_{\mu\nu}, \tag{1}$$

where $G_{\mu\nu}$ is the Einstein tensor, Λ is the cosmological constant, $g_{\mu\nu}$ is the metric tensor, G is the gravitational constant, c is the speed of light, and $T_{\mu\nu}$ is the energy-momentum tensor. The Einstein tensor $G_{\mu\nu}$ is defined by

$$G_{\mu\nu} = R_{\mu\nu} - \frac{1}{2} R\, g_{\mu\nu}, \tag{2}$$

where $R_{\mu\nu}$ and R are the Ricci curvature tensor and scalar respectively. An exact solution to Einstein's field equations, other than the trivial Minkowski solution, was found soon after publication using simplifying symmetry assumptions. The Schwarzschild metric, proposed in 1916 by Karl Schwarzschild, described the gravitational field around a non-rotating, spherically symmetric, and uncharged mass (Schwarzschild, 1916). In the coordinates of (t, r, θ, ϕ) and metric signature of [-,+,+,+], the Schwarzschild line element has the form

$$ds^2 = -\left(1 - \frac{r_s}{r}\right) c^2 dt^2 + \left(1 - \frac{r_s}{r}\right)^{-1} dr^2 + r^2 \left(d\theta^2 + \sin^2\theta\, d\phi^2\right), \tag{3}$$

where r_s is the Schwarzschild radius and has the value given by $r_s = 2\, r_{\mathrm{g}}$. The gravitational radius is defined as $r_{\mathrm{g}} \equiv GM/c^2$. For the Schwarzschild metric to differ significantly from the Minkowski metric, the ratio r_s/r must be large. For most known astrophysical applications at the time, the ratio is extremely small; thus, this solution was treated as a mathematical curiosity for much of the early-20th century.

Over forty years later in the mid-20th century, the concept of a black hole as a region of space from which nothing could escape was developed using the Schwarzschild metric (Finkelstein, 1958). In 1963, the solution for a rotating, uncharged body was found (Kerr, 1963). Furthermore, the discovery of gravitationally collapsed neutron stars showed the astrophysical relevance of highly compact objects like black holes (Shklovsky, 1967). Since then, observational inferences from independent paths of scientific inquiry have provided compelling evidence for the existence of such ultra-compact objects which do not shine. Tracing stellar orbits around the Milky Way Galactic Center showed the gravitational influence of a massive, highly dense object at the center of the Milky Way, which has physical parameters inconsistent with any realistic stellar cluster (e.g., Ghez et al., 1998). Highly efficient accretion disk radiation from Active Galactic Nuclei (AGNs) matched predictions made for rotating black holes (e.g., Bian and Zhao, 2003). In 2016, the Laser Interfermeter Gravitational-Wave Observatory (LIGO) utilized multi-messenger astronomy with gravitational waves and observed the waveform signature predicted for black hole merger events (Abbott, 2016). Despite the observational inferences, it was said that there was still no unambiguous proof that these objects are black holes rather than an extra dense, pressure-supported dark star (Falcke, Melia, and Agol, 2000). However, an image reconstruction of the supermassive black hole at the core of galaxy Messier 87 (M87) was produced and released recently by the Event Horizon Telescope (EHT) in April 2019, providing evidence for the existence of astrophysical structures which match the properties predicted for black holes. The images from the EHT are reproduced in Fig. 1.

The central roughly circular depression in brightness with a flux ratio of ≥ 10 shows the predicted black hole shadow, which is the gravitationally lensed image of the region of space bounded by unstable photon orbits. Surrounded by an asymmetric bright photon ring, its angular size is roughly $42 \pm 3\,\mu$as, which is consistent with the size expected based on mass estimations from gas-dynamical models (al., 2019). These radio-wave observations in 230 GHz frequency have provided powerful evidence that the active galactic nuclei (AGN) in the centre of galaxies are powered by supermassive black holes rather than alternative pressure-supported mass distributions. Based on the image, the model parameters fitted to the image estimate the

M87* mass to be $M_{\rm bh} = (6.5 \pm 0.7) \times 10^9 M_\odot$. Another primary source which is observable by the EHT is Sagittarius A* (Sgr A*), the black hole in the center of the Milky Way. Although it is significantly closer compared to M87*, it is also three orders of magnitude smaller and its dynamical timescale can be measured in minutes instead of days. By coincidence, it is also roughly three orders of magnitude closer and thus its angular size as it appears on the sky is roughly the same as M87*. The time variability of Sgr A* makes it a more challenging target to observe. Furthermore, viewing Sgr A* requires telescopes to observe through the interstellar medium in the spiral arms along the plane of the Milky Way. These additional scattering effects have to be accounted for and subtracted in the image reconstruction process. Nevertheless, the recently released M87* reconstructed image shows that direct studies on black hole event horizon scales are not just theoretically possible, but physically realizable.

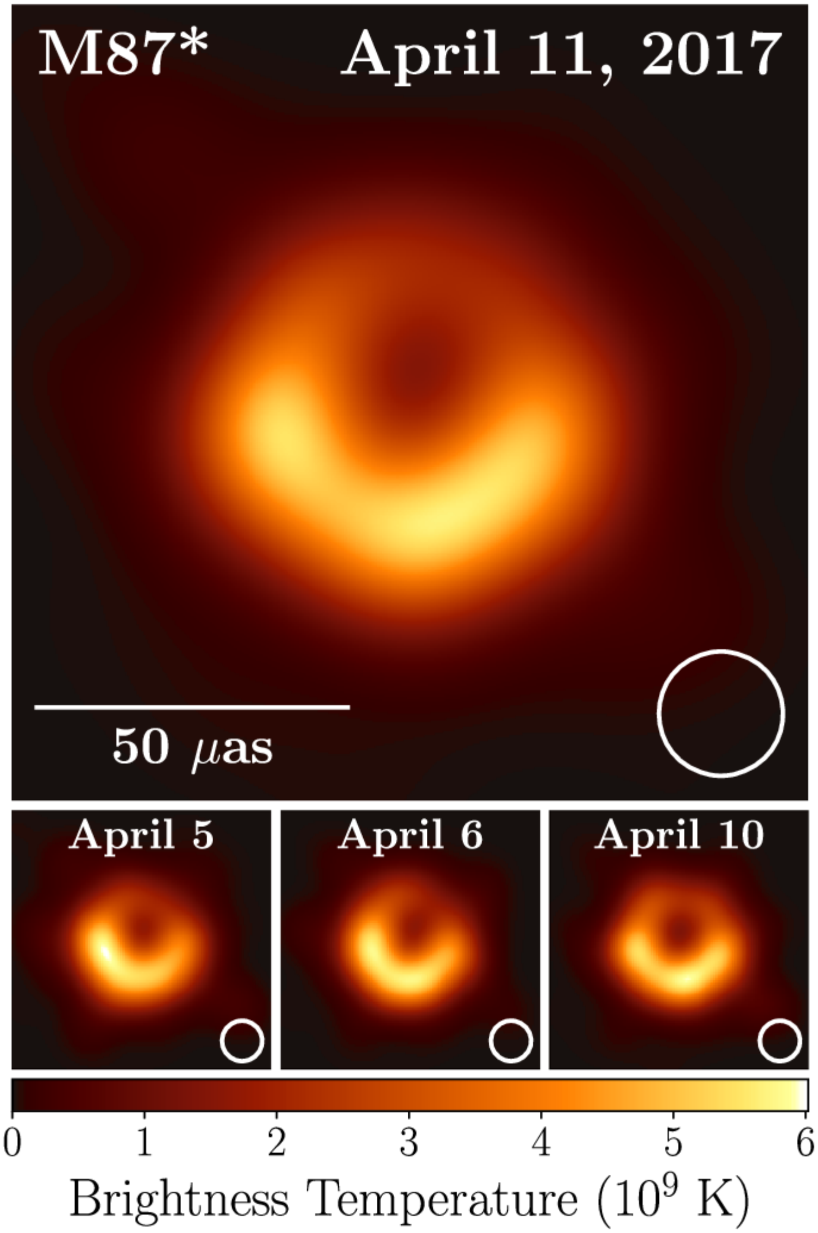

Figure 1: *Image reconstruction of M87* taken on four different days, showing some evolution on that six-day time period. The beam size is indicated by the hollow white circle on the bottom right. Figure was obtained from the first paper of the EHT collaboration (al., 2019).*

2.2 Astrophysical Black Holes

Due to the no-hair theorem, black holes can be categorised by three externally observable physical quantities: mass, spin, and charge (Israel, 1968). Mass is an essential property to the black hole, but since the spin and charge can vary, there are four classifications and corresponding metrics of black holes as indicated in Table 1.

	No Spin (J = 0)	Spin (|J| > 0)
Uncharged (Q = 0)	Schwarzschild	Kerr
Charged (Q ≠ 0)	Reissner-Norström	Kerr-Newman

***Table 1:** Black hole solutions of the Einstein field equations categorised by charge and spin.*

Though the non-spinning Schwarzschild metric is the first general vacuum solution of Einstein's field equations proposed which describes a black hole, angular momentum J and spin are known to be ubiquitous in astrophysical bodies. Since black holes are theorised to have formed from stellar gravitational collapse, it is expected for black holes to retain angular momentum from their progenitor star. Charged black holes are likely to be short-lived in nature, because the surrounding plasma in the accretion disk will quickly neutralise the black hole charge. Therefore, the most astrophysically relevant solution is the Kerr black hole where the magnitude of spin is non-zero $|\mathrm{J}| > 0$ (Bardeen, Press, and Teukolsky, 1972). The Kerr black hole line element in Boyer-Lindquist coordinates is (Cunningham and Bardeen, 1973)

$$\begin{aligned} \mathrm{ds}^2 = & -(1 - 2Mr/\Sigma)\,\mathrm{dt}^2 - (4\mathrm{Ma\,r}\sin^2\theta/\Sigma)\,\mathrm{dt}\,\mathrm{d}\phi \\ & + (\Sigma/\Delta)\mathrm{dr}^2 + \Sigma\,\mathrm{d}\theta^2 + (\mathrm{r}^2 + \mathrm{a}^2 + 2\mathrm{Ma}^2\sin^2\theta/\Sigma)\sin^2\theta\,\mathrm{d}\phi^2, \end{aligned} \tag{4}$$

where Σ and Δ are functions defined by

$$\Sigma \equiv r^2 + a^2\cos^2\theta, \qquad \Delta \equiv r^2 - 2M\,r + a^2. \tag{5}$$

The dimensionless spin parameter a is the angular momentum per unit mass defined as $a \equiv cJ/(GM^2)$, where J is the angular momentum and M is the black hole mass. A non-spinning Schwarzschild black hole has a spin parameter of $a = 0$ and the Kerr metric reduces to the Schwarzschild metric, while a maximally spinning black hole has a spin parameter $a = 1$. Superspinning black holes where $a > 1$ form naked singularities with important theoretical implications in general relativity, such as a violation of causality, but they have yet to be observed (Chakraborty, Kocherlakota, and Joshi, 2017).

The event horizon of the Kerr black hole is defined for the point of divergence in the metric when $\Delta = 0$. The solution for r in Eqn. 5 defines the event horizon radius,

$$r_{\mathrm{EH}} \equiv M + (M^2 - a^2)^{1/2}, \tag{6}$$

where the positive root was taken. This event horizon is a coordinate singularity rather than a physical singularity as it can be removed by transforming the metric into a different set of coordinates. The Kerr physical singularity manifests as a ring of zero thickness located on the equatorial plane determined by the spin axis (Visser, 2007). Another critical radius defined by the Kerr metric is the static limit, which is located where the temporal diagonal component, g_{tt}, vanishes. At this point, time-like word-lines outside the static limit change into space-like world-lines within. Using Eqn. 4, the g_{tt} component vanishes when $(\Sigma - 2Mr) = 0$. The positive root of r defines the radius of the static limit,

$$r_{\mathrm{SL}} \equiv M + \left(M^2 + a^2\,\cos^2\theta\right)^{1/2}, \tag{7}$$

which is also the outer boundary of the ergosphere. Within the ergosphere, spacetime is dragged along the black hole's direction of rotation and photon geodesics are forced to co-rotate with the black hole. This rotational frame-dragging is called the Lense-Thirring effect (Thirring, 1918).

From the principle of least action, the general Lagrangian can be written for any given metric,

$$\mathcal{L} = \frac{1}{2}g_{\mu\nu}\dot{x}^{\mu}\dot{x}^{\nu}, \tag{8}$$

where $g_{\mu\nu}$ denotes a metric element and Greek indices are used to represent four components. The dotted terms such as $\dot{x}^{\mu}$ represent a derivative with respect to an affine parameter chosen to parameterise the path of the photon or particle. Noether's theorem states that there is an associated conservation law whenever the Lagrangian remains invariant against modifications of a quantity. In general relativity, symmetries in the geometry of spacetime which preserve the metric are expressed as Killing vectors with a vanishing Lie derivative (D'Inverno, 1992). For the Kerr metric, the t and ϕ vectors are killing vectors associated with the conserved quantities,

$$E = -p_{\mathrm{t}}, \qquad L = p_{\phi}, \tag{9}$$

where E is the total energy, and L is the angular momentum parallel to the spin axis. For a quantity, q, the generalised momentum, p_{q}, is defined by Lagrangian mechanics, such that $p_{\mathrm{q}} = \partial\mathcal{L}/\partial\dot{q}$. Two other conserved quantities in the Kerr metric are the particle rest mass and the Carter constant. The rest mass, m, is defined by the contraction of the four-momentum, $p^{\mu}p_{\mu} = -m^2$, and is invariant under transformation. The Carter constant, Q, expresses a higher order symmetry (Carter, 1968) and is defined as

$$Q = p_{\theta}^2 + \cos^2\theta\, \left[a^2\left(\mathrm{m}^2 - \mathrm{p}_{\mathrm{t}}^2\right) + \mathrm{p}_{\phi}^2\mathrm{csc}^2\theta\right], \tag{10}$$

describing a precise term which is quadratic in linear momenta added onto the total angular momentum (Rosquist, Bylund, and Samuelsson, 2009). In the case when $\theta = \pi/2$ and $a = 0$, the Carter constant reduces to the square of the orbital angular momentum. Using Euler-Lagrange formalism, equations of motion governing motion along geodesics around Kerr black holes can be found. Prograde and retrograde orbits are represented by the upper and lower signs (ie. ±) respectively in the following equations of motion:

$$\begin{aligned}
\Sigma\frac{dr}{d\lambda} &= \pm(V_{\mathrm{r}})^{1/2},\\
\Sigma\frac{d\theta}{d\lambda} &= \pm(V_{\theta})^{1/2},\\
\Sigma\frac{d\phi}{d\lambda} &= -(a\,E - L/\sin^2\theta) + \mathrm{a\,T}/\Delta,\\
\Sigma\frac{dt}{d\lambda} &= -a\,(a\,E\sin^2\theta - \mathrm{L}) + (\mathrm{r}^2 + \mathrm{a}^2)\mathrm{T}/\Delta,
\end{aligned} \tag{11}$$

where $\lambda = \tau/m$ is the affine parameter. The motion along the r and θ components are written in terms of effective potentials defined as

$$\begin{aligned}
V_{\mathrm{r}} &\equiv T^2 - \Delta\,[m^2r^2 + (L - a\,E)^2 + Q],\\
V_{\theta} &\equiv Q - \cos^2\theta[\mathrm{a}^2\,(\mathrm{m}^2 - \mathrm{E}^2) + \mathrm{L}^2/\sin^2\theta],
\end{aligned} \tag{12}$$

where $T \equiv E(r^2 + a^2) - a\,L$. Circular orbits are defined to have a constant radius along the orbital path such that $dr/d\lambda = 0$. Combining Eqn. 11 and Eqn. 12, the total energy and angular momentum can be solved for circular orbits:

$$\begin{aligned}
E/m &= \frac{r^{3/2} - 2M\,r^{1/2} \pm aM^{1/2}}{r^{3/4}\left(r^{3/2} - 3M\,r^{1/2} \pm 2aM^{1/2}\right)^{1/2}},\\
L/m &= \frac{\pm M^{1/2}\left(r^2 \mp 2aM^{1/2}\,r^{1/2} + a^2\right)}{r^{3/4}\left(r^{3/2} - 3M^{1/2}\,r^{1/2} \pm 2aM^{1/2}\right)^{1/2}}.
\end{aligned} \tag{13}$$

The value of these two conserved quantities are only real if $\left(r^{3/2} - 3r^{1/2} \pm 2a\right) > 0$. Thus, there is a region of space near a Kerr black hole in which circular orbits do not exist for particles, while massless particles are able to maintain unstable orbits on the boundary (Bardeen, Press, and Teukolsky, 1972). The radius to the boundary of unstable photon orbits, r_{ph}, is

$$r_{\mathrm{ph}} = 2M\left\{1 + \cos\left[\frac{2}{3}\cos^{-1}\left(\mp\mathrm{a}\right)\right]\right\}, \tag{14}$$

where the upper and lower sign ∓ indicate that the radius is dependent on whether the photon orbits are prograde or retrograde. The unstable photon orbit boundary is important because it defines the observable edge of the Kerr black hole. The black hole shadow is the gravitationally lensed image of the region of space bounded by these unstable photon orbits. An important critical radius for accretion dynamics is the innermost stable circular orbit (ISCO). The ISCO marks the inner radius of the black hole accretion disk and requires a stability condition that $V_{\mathrm{r}}''(r) \leq 0$. Using the spin parameter, the ISCO radius, r_{ISCO}, can be calculated from:

$$\begin{aligned} r_{\mathrm{ISCO}} &= M\left(3 + Z_2 \mp [(3 - Z_1)(3 + Z_1 + 2Z_2)]^{1/2}\right), \\ Z_1 &\equiv 1 + (1 - a^2)^{1/3}\left[(1 + a)^{1/3} + (1 - a)^{1/3}\right], \\ Z_2 &\equiv \sqrt{3a^2 + Z_1^2}. \end{aligned} \tag{15}$$

As the black hole spin increases, the retrograde ISCO increases towards 9 r_{g}, while the prograde ISCO radius and the radius of the unstable photon orbit decrease toward the event horizon radius.

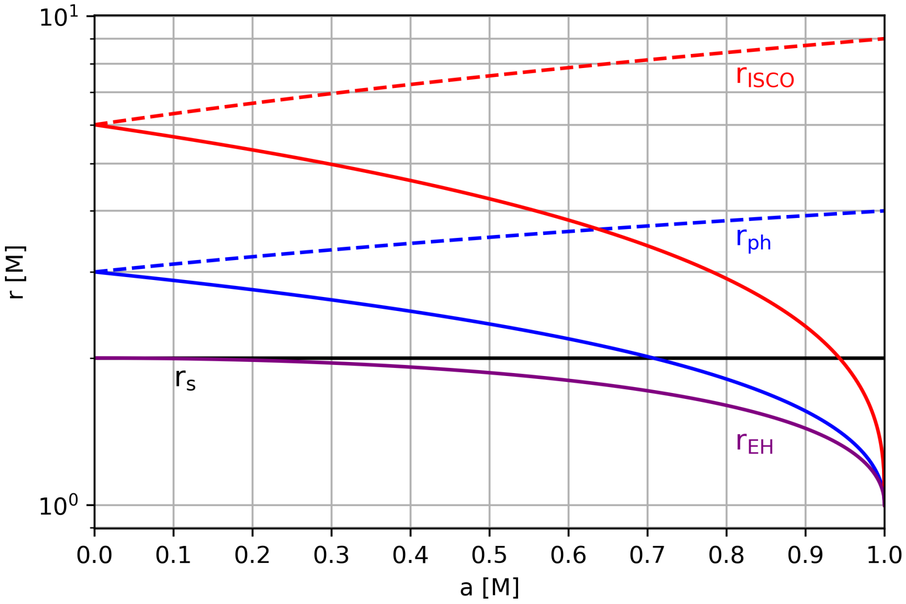

Figure 2: *Critical radii of a Kerr black hole separated into prograde (solid) and retrograde (dashed) orbits. The data for the figure was obtained from eqns. 6, 14, and 15.*

A spherically symmetric accreting system contains a balance between the gravitational force and outward radial pressure, such that the net force is described by (Frank, King, and Raine, 2002)

$$F_{\mathrm{net}} = \left(\frac{GM(m_{\mathrm{p}} + m_{\mathrm{e}})}{r^2}\right) - \frac{S\,\sigma_{\mathrm{T}}}{c}, \tag{16}$$

where S is the radiant energy flux and σ_{T} is the Thomson cross-section. The masses of the proton and electron are denoted by m_{p} and m_{e} respectively. Under spherical symmetry, the net force is only dependent on the radial parameter r and if the system consists of free protons and electrons, then forces are exerted on electrons through Thompson scattering. The luminosity of the object is related to the radiant energy flux S by $L = 4\pi r^2 S$ under spherical symmetry, and in hydrostatic equilibrium, the pressure force and gravitational force balances so that the net force is zero. Thus, the Eddington luminosity, or the maximum luminosity of the source in hydrostatic equilibrium, is described by

$$L_{\mathrm{Edd}} \equiv L = \frac{4\pi G M m_{\mathrm{p}} c}{\sigma_{\mathrm{T}}} \approx 3.2 \times 10^4 \left(\frac{M}{M_\odot}\right) L_\odot\,, \tag{17}$$

where $M_\odot$ and $L_\odot$ are the solar values of mass and luminosity. If the source luminosity exceeds the Eddington value, material will be lost by radiation outflow. The Eddington luminosity can be used to set the upper bound on radiation emitted from processes in the accretion disk surrounding Kerr black holes.

The luminosity can be related to the mass accretion rate by

$$L_{\mathrm{acc}} = \eta \dot{M} c^2, \tag{18}$$

where η is the nominal efficiency of converting accretion mass into energy and $\dot{M}$ is the mass accretion rate. Thus, assuming the highly efficient value of $\eta = 0.1$, the Eddington mass accretion rate is (Frank, King, and Raine, 2002)

$$\dot{M}_{\mathrm{Edd}} = \frac{10\, L_{\mathrm{Edd}}}{c^2}. \tag{19}$$

The thin disk accretion model is a reasonable approximation for high accretion rates above $\dot{M} \sim 0.01\, \dot{M}_{\mathrm{Edd}}$ (Quataert, 2003). In the case of $L \ll 0.1 \dot{M} c^2$, very little energy generated by accretion processes is converted into radiation, where this regime is called Radiatively Inefficient Accretion Flow (RIAF). Instead, most of the energy is stored as thermal energy, increasing the temperature of the accreting gas (e.g., Narayan and Yi, 1995; Svensson, 1999; Menou, 2005). In a two-temperature structure, most of the thermal energy is stored with hot ions which transfer the energy inefficiently to the radiating electrons. The dynamics of rotating accretion flow in RIAF is described by Advection-Dominated Accretion Flows (ADAFs). Most models, including the one used for this research thesis, use the RIAF state so that the flow structure is geometrically thick, and the radiative cooling time-scale is much longer than the viscous gas time-scale (Quataert, 2003). Under ADAF, the viscous energy is stored as thermal energy in the gas, which is then advected onto the black hole.

Although Kerr black holes aren't charged, magnetic field lines develop in the charged plasma of the accretion disk. In principle, rotational kinetic energy can be extracted from the spinning the black hole inside the ergosphere through the Blandford-Znajek process (Blandford and Znajek, 1977). In addition, there can be angular momentum transfer to accreting matter through the Penrose process as well (Penrose and M. Floyd, 1971). As a result, rotating black holes have strong magnetic fields which power the dynamics of accretion.

2.3 Black Hole Imaging

The black hole at the galactic core of M87, located (16.4 ± 0.5) Mpc away (Bird et al., 2010), was estimated from gas-dynamical models to have a mass of $M = (6.6 \pm 0.4) \times 10^9\, M_\odot$. With these parameters, the Schwarzschild radius, which marks the event horizon of a non-rotating black hole, is 6.3×10^{-4} pc. For an observer viewing from infinity, the photon capture radius of the Schwarzschild black hole is $R_{\mathrm{c}} = \sqrt{27}\, r_{\mathrm{g}}$ Thus, resolving the M87 supermassive black hole, M87*, at this scale requires an angular resolution $R \approx 41.2\, \mu$as, whereas resolving Sgr A*, the black hole at the Milky Way Galactic Centre, requires $R \approx 53\, \mu$as.

The diffraction-limited theoretical resolution of a telescope can be described by

$$R = k \frac{\lambda}{D}, \tag{20}$$

where $k = 1.22$ is a diffraction value through a circular aperture, λ is the wavelength of observation, and D is the diameter of the aperture. Since the EHT emulates a telescope with the size of the Earth's diameter $D \approx 12{,}742$ km, the maximum resolution of EHT is $R \approx 26\, \mu$as. Because the maximum baseline distances between North-South and East-West cardinal distances differ for the EHT array, the observing beam is elliptical. By correcting for the scatter broadening from the interstellar medium and taking into account the EHT telescope resolution, it was predicted in the early 21st century that both Sgr A* and M87 could be directly imaged (Falcke, Melia, and Agol, 2000).

The frequency chosen to observe M87* was the radio 230 GHz band, which is located near a local flux maximum in the spectral energy distribution. In addition, the 230 GHz frequency is within a region of high atmospheric transmission called the radio window (Schieven, 2018) and the source is optically thin at the mm wavelengths (Akiyama, 2019a). Together, these factors made the 230 GHz band a desirable choice of observational frequency for the EHT.

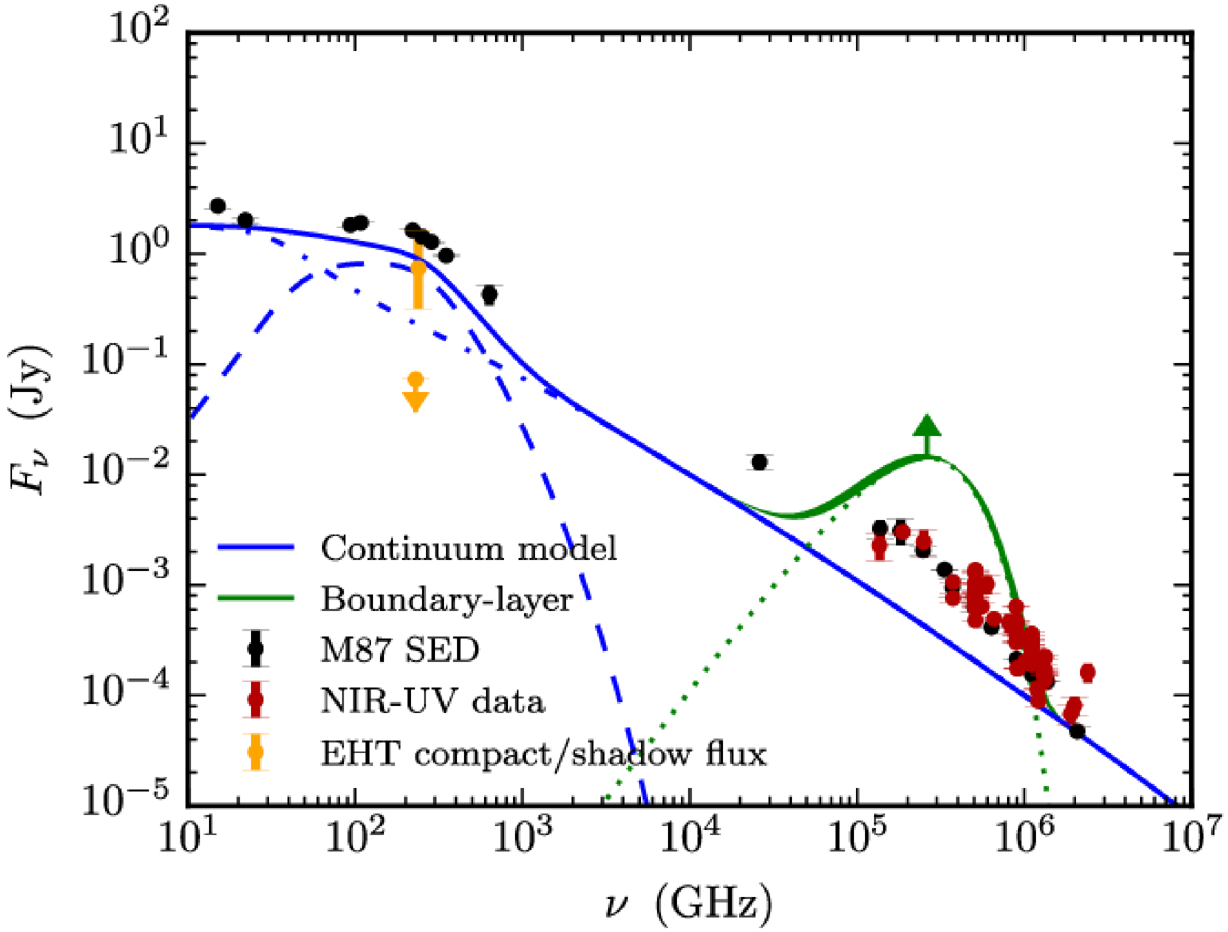

Figure 3: *The SED of M87 is indicated by the black data points. The observing frequency of the EHT at 230 GHz is close to the local flux maximum and the turnover point when the flux is beginning to decrease. The figure was obtained from Figure 20 of the sixth paper from the EHT collaboration (Akiyama, 2019d).*

To image M87*, the EHT employed sub-millimeter very-long baseline interferometry (VLBI) by correlating data from an array of independent radio observatories around the world to create a single high-resolution image. Measurements taken by the EHT were Fourier transformed and recorded in frequency space. For every pair of telescopes in the EHT array, a single frequency measurement could be made. As the Earth rotates, the baseline distance changes and these measurements formed elliptical tracks in the image's frequency plane until the entire frequency space of the image is sparsely sampled by the available EHT telescopes. Fig. 4 shows the sampling of M87* by the EHT telescopes over the four nights of observation.

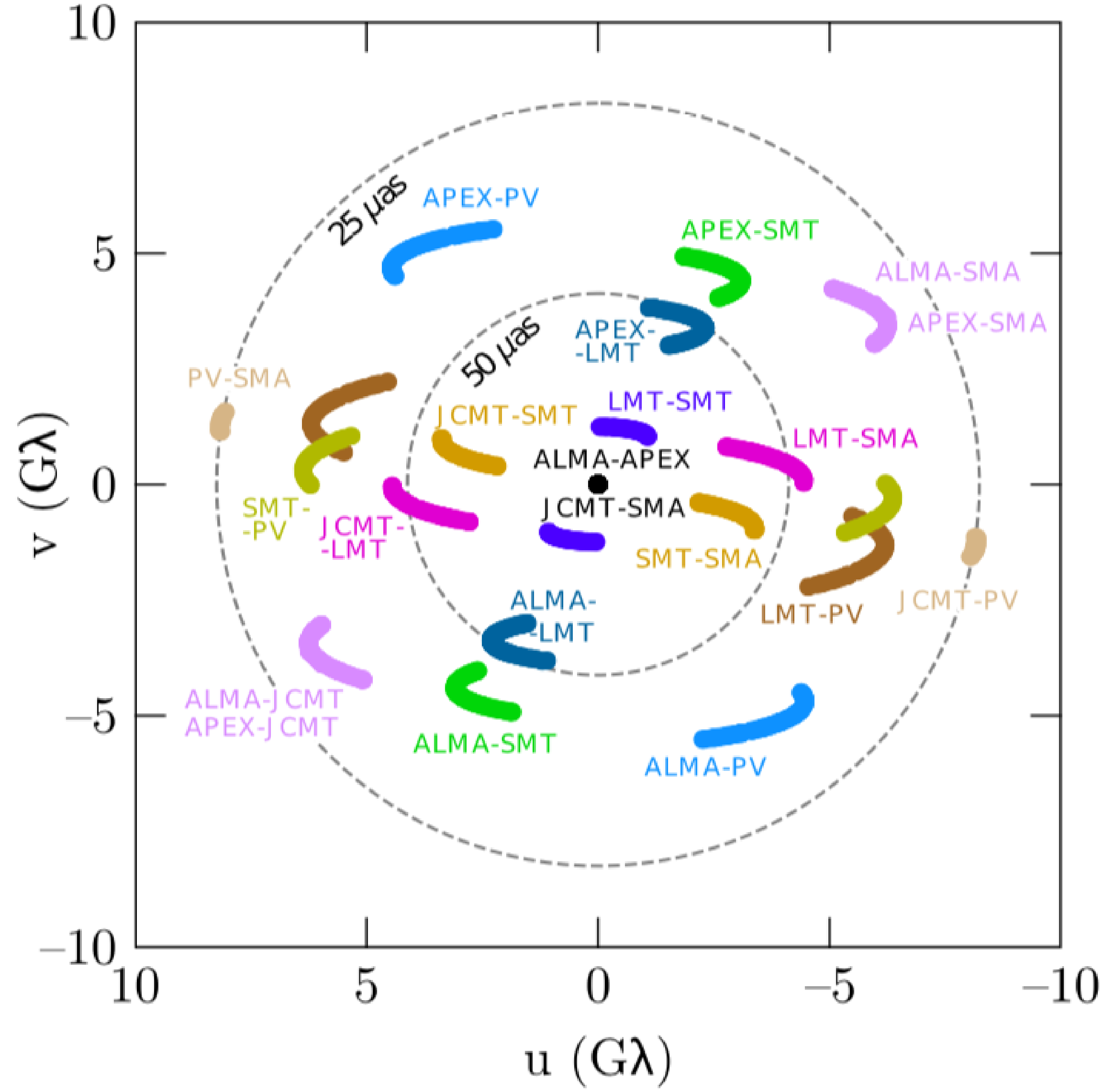

Figure 4: *Complete aggregate EHT coverage for M87 in Fourier space over the four separate nights of observation. The figure was obtained from Figure 11 of the second paper from the EHT collaboration (Akiyama, 2019a).*

The digital data from each telescope were correlated using the precise atomic clocks and calibrated according to the absolute phase of the signal. Large volumes of data were stored in hard drives and shipped from the global network of radio observatories to MIT Haystack Observatory and Max Planck Institute for Radio Astronomy to be correlated. Closure quantities, such as the closure phase and closure amplitude, are invariant of calibration terms and can be used to cancel out the error from the atmospheric phase and systematic gain (Bouman et al., 2016). Due to the sparse sampling of the observation in frequency space, the results of the inverse Fourier transform are not unique, such that there is an infinite number of images that can be obtained. In addition, models of the interstellar medium and atmospheric turbulence were required to correct for contaminating effects (Bouman et al., 2016; Johnson et al., 2017). The four EHT teams charged with reconstructing the image from the data worked independently and used two different imaging algorithms, CLEAN and Continuous High-resolution Image Reconstruction using Patch priors (CHIRP), which were tested using synthetic images. CHIRP was an algorithm first presented in 2016 which uses a Bayesian statistics inspired approach. The algorithm parameterises the continuous image with a discrete number of terms, accounts for a Gaussian noise distribution, and utilizes an iterative optimization framework for energy minimization, called the maximum entropy method (MEM) (Bouman et al., 2016). Under synthetic experimentation, it has demonstrated results with low signal-to-noise ratio (SNR). The final results of the four teams were averaged together to produce the image of the M87* released to the public on the 10th of April, 2019, represented in Fig. 1.

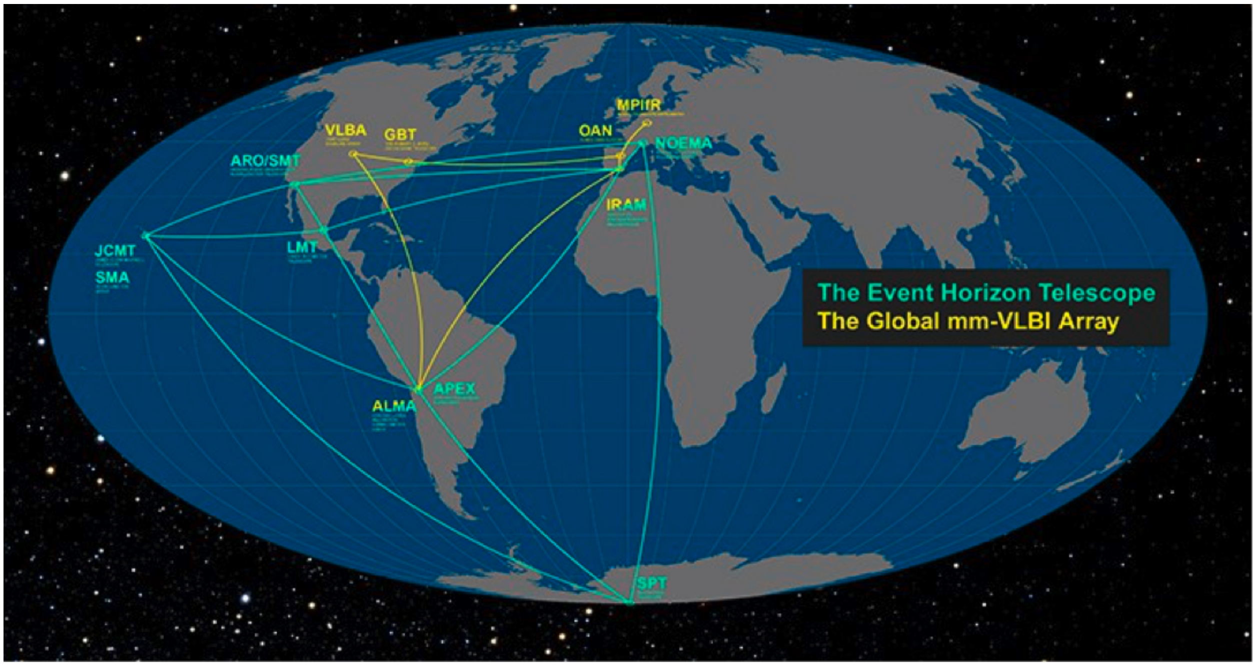

Figure 5: *Map of EHT array sites around the globe displayed on a Mollweide map projection. Credit: EHT Collaboration.*

Previous simulations of M87* incorporated the effects of disk-dominated thermal synchrotron radiation. However, the galaxy is well-known for its extended kiloparsec-scale relativistic jet which originates from the supermassive black hole (Davelaar et al., 2019). The objective of this research thesis is to use full three-dimensional general-relativistic magnetohydrodynamics (GRMHD) to simulate black hole accretion flow and general-relativistic radiative transfer (GRRT) and model the hybrid non-thermal synchrotron radiation produced by the jet-launching region of M87*. The differences between the thermal and hybrid non-thermal models will be discussed and synthetic images will be produced which capture these differences. The discussion will include four GRMHD snapshots in time and three observing frequencies. The time variability between snapshots will also be discussed and compared between frequencies. Furthermore, comparisons will be made against the EHT VLBI results in 230 GHz, Very-Long Baseline Array (VLBA) observations of M87* in 43 GHz, and Global Millimeter VLBI Array (GMVA) results in 86 GHz. In the upcoming chapters, the conservative equations which govern the general-relativistic magnetohydrodynamics (GRMHD) of the simulation will be introduced. Examples of the flow quantities for a near maximally-spinning black hole will be shown. Next, the general-relativistic radiative transfer (GRRT) formulation will be shown with a description of the two-temperature model and the thermal as well as non-thermal emissivities and absorptivities. Example photon trajectories will be ray-traced across the Kerr black hole geometry. In the penultimate chapter, synthetic M87* images will be created in the thermal and hybrid non-thermal models, showing similarities, differences, and time variability. The thesis body ends with a discussion of future EHT observations.

3 General-Relativistic Magnetohydrodynamics

Kerr black holes can be characterised by rotation alongside strong gravitational and electromagnetic fields. The structure of the accretion flow can be understood by adopting an ideal general-relativistic magnetohydrodynamical (GRMHD) model, which treats the plasma as a perfect electrically conductive fluid. Compared to semi-analytic models, the single fluid model doesn't require solving numerous individual equations of motion for each particle in the system. Instead, macroscopic quantities such as pressure, density, temperature, and magnetisation are used to describe the system. Simulating strongly magnetised astrophysical dynamics in general relativity is important in understanding the physics of compact objects such as black holes and neutron stars, since the strong magnetic field plays a crucial role in the formation and collimation of jets responsible for gamma ray bursts and accretion-powered pulsars (Shibata and Sekiguchi, 2005). GRMHD codes were developed in order to study astrophysical phenomena with high magnetic and gravitational fields evolving in dynamical spacetime. Ideal GRMHD assumes the presence of a single-component perfect fluid of ions with no distinctions between species. The perfect fluid has an ideal equation of state which depends on the adiabatic index, and can be characterised completely by the mass density in the rest frame. In this chapter, the conservative equations of GRMHD and the GRMHD data from the Black Hole Accretion Code will be discussed.

3.1 Equations of General-Relativistic Magnetohydrodynamics

The GRMHD simulation is a conservative scheme which proceeds by discrete time steps and updating a set of conserved variables. In a finite volume method, the conserved variables are calculated using fluxes across a meshed geometry (Porth et al., 2017). By the divergence theorem, volume integrals containing divergence terms are converted into integrals across the surface of the finite volume. Multi-dimensional Riemann solvers are used to convert the set of conserved variables back into primitive variables which describe the fluid. The following discussion is a description of the well-known equations of GRMHD written in conservative form to be used in numerical integration (Gammie, McKinney, and Toth, 2003). The speed of light $c = 1$ unless otherwise stated.

In a thermodynamic system, the ideal equation of state defines the relationship between the gas pressure P and the density of the gas ρ. A calorically perfect gas approximations assumes that the heat capacities are independent of the temperature. Under that approximation, the ideal equation of state is

$$P = (\gamma - 1)\rho e, \tag{21}$$

where the ratio of specific heats defines the adiabatic index, $\gamma = C_{\mathrm{p}}/C_{\mathrm{v}}$. For a non-relativistic monatomic fluid, $\gamma = 5/3$, and for a relativistic fluid, $\gamma = 4/3$. The internal energy per unit mass is represented by $e = C_{\mathrm{v}}T$, where T is the temperature of the gas.

The particle number and particle mass are conserved quantities which follow the conservation law

$$(nu^{\mu})_{;\mu} = 0\,, \tag{22}$$

where n is the particle number density and u^{μ} is the four-velocity. The semi-colon subscript represents a covariant derivative such that $V^{\nu}{}_{;\mu} = \nabla_{\mu}V^{\nu}$. The total energy and momentum written in the form of an energy-momentum tensor is also conserved

$$T^{\mu\nu}{}_{;\nu} = 0\,. \tag{23}$$

The fluid portion of the energy-momentum tensor depends on the internal energy U, pressure P, and density ρ,

$$T^{\mu\nu}_{\mathrm{fluid}} = (\rho + U + P)\, u^{\mu}u^{\nu} + Pg^{\mu\nu}, \tag{24}$$

while the electromagnetic part of the energy-momentum tensor is:

$$T^{\mu\nu}_{\mathrm{EM}} = b^2u^{\mu}u^{\nu} + \frac{1}{2}b^2g^{\mu\nu} - b^{\mu}b^{\nu}. \tag{25}$$

Including all fluid and electromagnetic components, the energy-momentum tensor can be written as

$$\begin{aligned} T^{\mu\nu}_{\mathrm{MHD}} &= T^{\mu\nu}_{\mathrm{EM}} + T^{\mu\nu}_{\mathrm{fluid}} \\ &= \left(\rho + U + P + b^2\right) u^\mu u^\nu + \left(P + \frac{1}{2}b^2\right) g^{\mu\nu} - b^\mu b^\nu. \end{aligned} \tag{26}$$

The electric field is neglected in the rest frame of the fluid due to its high conductivity. In Lorentz-Heaviside units, factors of 4π no longer appear in the equations and the magnetic field four-vector, b^μ, is defined as

$$b^\mu \equiv -\frac{1}{2}\epsilon^{\mu\nu\kappa\lambda} u_\nu F_{\lambda\kappa}, \tag{27}$$

where $F^{\mu\nu}$ represents the electromagnetic field tensor and $\epsilon^{\mu\nu\kappa\lambda}$ is the Levi-Civita tensor. The evolution of the electromagnetic field is governed by Maxwell's equations in conservative form. Written as the conservation of the Faraday tensor, it is:

$$F^{\mu\nu}{}_{;\mu} = 0. \tag{28}$$

Ideal GRMHD uses a simplification of the generalised Ohm's law which neglects resistivity, anisotropy, electron pressure, electron inertia, and the Hall term proportional to $J \times B$. Neglecting these terms, Ohm's law is written simply as

$$E + v \times B = 0. \tag{29}$$

3.2 Accretion Flow Structure and Dynamics

The Black Hole Accretion Code (BHAC) is used for the Kerr black hole accretion simulation. Details of its implementation are found in Porth et al., 2017. The equations of GRMHD are solved in arbitrary spacetime geometries using a refined and efficient finite volume method. The initial conditions of the simulation consist of the Fishbone-Moncrief magnetised torus supported by pressure and centrifugal forces (Fishbone and Moncrief, 1976). The initial structure is characterised by a rotational equilibrium distribution with constant angular momentum, while the magnetic field is derived from the vector potential $A_\phi \propto \mathrm{MAX}(\rho_0/\rho_{0,\mathrm{min}} - 0.2,\ 0)$ and follow contours of constant density with an additional constraint that the minimum plasma beta is 100 (Gammie, Shapiro, and McKinney, 2004). Magneto-rotational instability (MRI) develops after an initial perturbation of a purely poloidal magnetic field and provides the turbulent stresses for angular momentum transfer between particles which are connected by magnetic field lines (Balbus and Hawley, 1991). As a result, the magnetic field is amplified and drives accretion onto the black hole. Over time, a quasi-stationary equilibrium state is reached between the inflow and outflow rate of material. The poloidal magnetic field can lead to a configuration which resists further accretion of gas (Narayan et al., 2012). This case occurs when the magnetic flux reaches a maximum value and is termed a Magnetically Arrested Disk (MAD). In order to keep the accreting gas from becoming magnetically arrested, the initial seeded magnetic field is carefully arranged. Typically, the initial magnetic field for a MAD simulation is much greater so that the magnetic flux reaches its maximum value in a short amount of time. The case for Standard and Normal Evolution (SANE) is more extensively studied in existing literature, so this case is used for the GRMHD simulation. However, both models are useful for understanding accretion dynamics in astrophysical black holes.

The following images show the density, pressure, magnetic field strength, and magnetisation of the initial Fishbone-Moncrief torus used in the GRMHD simulations. The strength of the magnetic field is set according to the pressure such that

$$\beta \equiv 8\pi P_{\mathrm{gas}}/b^2 = 100, \tag{30}$$

where $b^2 = b_\mu b^\mu$ is the contraction of the magnetic field four-vector. The plasma beta β is defined as the ratio between the gas and magnetic pressure. In ideal GRMHD and frozen-in flow, the ratio indicates whether the motion of the magnetic field follows the plasma or vice versa. The thermal pressure is then perturbed by white noise with an amplitude of 4%, according to

$$P^* = P(1 + X_{\mathrm{P}}), \tag{31}$$

where X_p is a random, but uniformly distributed variable with amplitude between -0.02 and 0.02. In order to prevent the density and pressure from dropping to zero in the funnel region, the BHAC code utilizes floor models where if either $\rho < \rho_\mathrm{fl}$ or $P < P_\mathrm{fl}$, then the value is set to that of the floor. The floor values used by McKinney and Gammie, 2004 are $\rho_\mathrm{fl} = 10^{-5} r^{-3/2}$ and $P_\mathrm{fl} = 1/3 \times 10^{-7} r^{-5/2}$. A finite amount of matter is injected in the evacuated jet region to keep the hydrodynamic evolution viable.

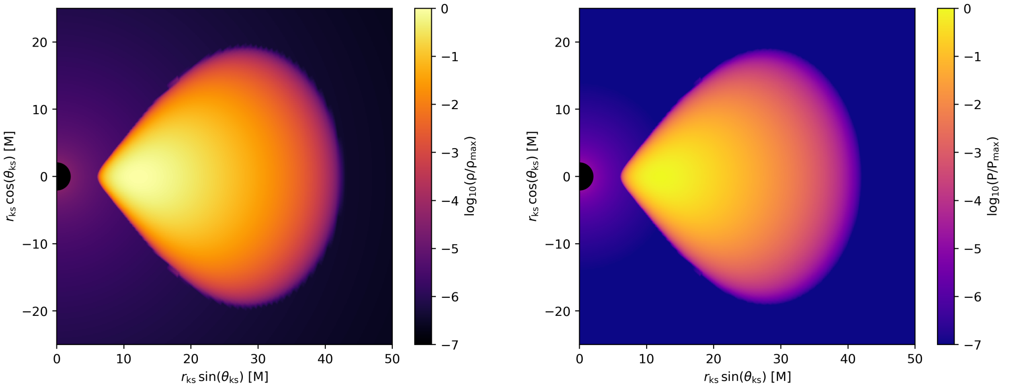

(a) ρ *(b) P*

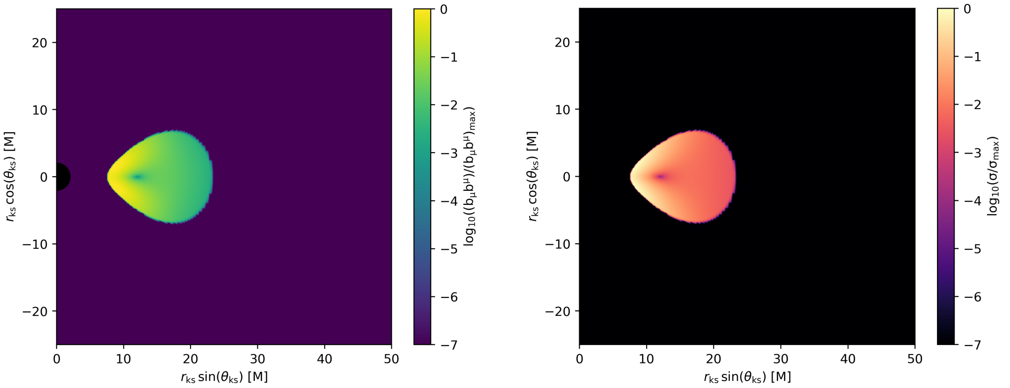

(c) $b_\mu b^\mu$ *(d) Magnetisation σ*

Figure 6: *Initial condition of the GRMHD simulation in Kerr-Schild coordinates, showing the Fishbone-Moncrief torus at $t = 0$. The single-slice density, pressure, magnetic field strength, and magnetisation data are shown in logarithmic scale. The magnetic field is poloidal and constrained to have a minimum plasma beta of 100. The black hole horizon is shown as a black disk. These snapshots were obtained from a simulation with BHAC.*

A set of quantities on the horizon-scale and on the global scale are used to describe the evolution of the accretion flow. All quantities are written in Kerr-Schild coordinates. Across the black hole horizon, the code mass flux is

$$\dot{M} := \int_0^{2\pi} \int_0^{\pi} \rho u^\mathrm{r} \sqrt{-g}\, \mathrm{d}\theta \mathrm{d}\phi \,, \tag{32}$$

where the stated quantities of density ρ and radial component of four-velocity u^r are evaluated at the event horizon. The following figure presents the mass accretion rate across the simulation time range. The GRMHD simulation begins at $t = 0$ and evolves until $t = 10000M$, where the time is related to the gravitational mass by $t = r_\mathrm{g}/c$. Snapshots of the simulation data are taken at every $\Delta t = 10M$ interval and the data is stored in UCL High Performance Computing (HPC) Myriad cluster.

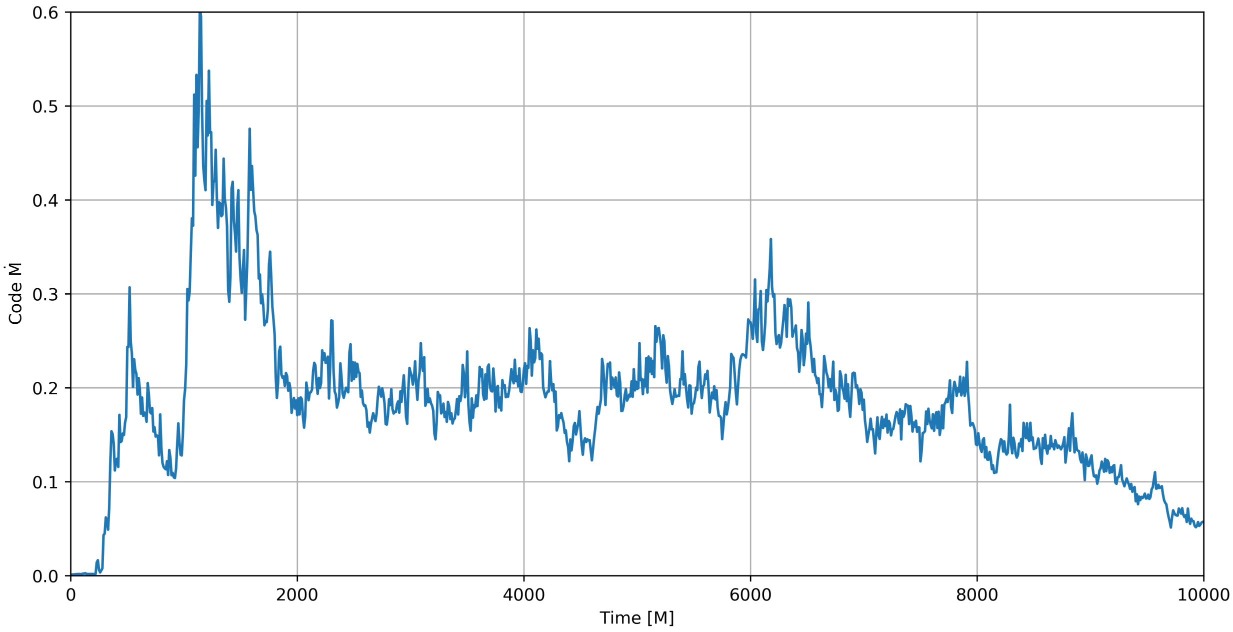

Figure 7: *Code mass accretion rate calculated with Eqn. 32 from the BHAC GRMHD data. The mass flux is evaluated at the cell closest to the outer horizon of the black hole* r_{h}*. At* $t \approx 6000M$*, the mass accretion rate decreases on average as is expected for SANE.*

In Fig. 7, the simulation starts with an initial equilibrium torus where the mass accretion rate is zero. Shortly after, magneto-rotational instability sets in, and the mass flux across the event horizon increases sharply before a feedback mechanism activates and causes the mass accretion rate to fluctuate around 0.2 in code units, which are scaled to the number of solar masses in a year multiplied by a free scaling parameter. The feedback mechanism suppressing mass accretion is caused by the build-up of magnetic pressure just outside the event horizon. Beginning at around $t = 6000M$, the mass accretion rate decreases steadily with time on average as is expected for an accreting cloud losing its mass to the black hole (Janiuk, Sukova, and Palit, 2018). From the figure, the data for the flow quantities before $t = 6000M$ are caused by the imposed simple, but unphysical initial conditions of the simulation, while the data after this cutoff time is physically meaningful. The mass accretion rate is scaled by the free scaling parameter such that the total compact flux density at 230 GHz within a $r \approx 40\,\mu$as range of M87* is 0.5 Jy at $t = 7000M$ for an observer at an inclination of $\theta_0 = 163°$. This value for the total compact flux density is within the range of observed fluxes from the observation of M87* by the EHT (Akiyama, 2019b).

The radial profile of flow variables in Kerr-Schild coordinates can be computed by averaging across the angular coordinates. For a quantity $q \in \{\rho, P, u^{\mathrm{r}}, \sqrt{b_\mu b^\mu}\}$, the disk-averaged flow variables is defined by

$$\bar{q}(r,t) := \frac{\int_0^{2\pi}\int_0^{\pi} q(r,\theta,\phi,t)\sqrt{-g}\,d\theta\,d\phi}{\int_0^{2\pi}\int_0^{\pi}\sqrt{-g}\,d\theta\,d\phi}, \tag{33}$$

where some calculations limit the θ integration range to $\theta_{\min} = \pi/3$ and $\theta_{\max} = 2\pi/3$ so that only material from the disk is taken into account. Instead, the hydrodynamical Bernoulli parameter, $-hu_{\mathrm{t}}$, is used where h is the specific gas enthalpy and u_{t} is the covariant time component of the four-velocity. The specific gas enthalpy h is calculated in the code by

$$h = 1 + \frac{\gamma}{\gamma - 1} P_{\mathrm{gas}}/\rho\,, \tag{34}$$

where the adiabatic index $\gamma = 4/3$ assuming ideal equation of state. In general, the Bernoulli parameter is a quantity which represents the sum of the kinetic energy, potential energy, and specific enthalpy. When a parcel of gas has a positive Bernoulli parameter, it is unbound and has the potential to reach infinity. A flow with negative Bernoulli parameter is bound (Penna, Kulkarni, and Narayan, 2013). The boundary between the thermal and non-thermal emission mechanisms in our model is $-hu_{\mathrm{t}} = 1.02$. This corresponds to a plasma velocity of $v = 0.2c$ (Moscibrodzka, Falcke, and Noble, 2016). This condition also sets the boundary between the disk and the jet for the purpose of the disk-averaged flow quantities.

Apart from the radial profile, azimuthally averaged flow variables are also used as a diagnostic to average out single-slice turbulence and visualise global scale events. These quantities are defined by

$$\bar{q}(r, \theta, t) \coloneqq \frac{\int_0^{2\pi} q(r, \theta, \phi, t) d\phi}{2\pi}, \tag{35}$$

where again, the hydrodynamical Bernoulli parameter is used to constrain quantities to within the disk. The primitive flow variables of gas pressure and density are combined together to form a proxy diagnostic of the ion temperature, Θ_{ion}, computed from

$$\Theta_{\mathrm{ion}} = P_{\mathrm{gas}}/\rho. \tag{36}$$

The magnetisation of a region represents the density of magnetic moments and is defined from primitive flow variables as

$$\sigma = b^2/\rho. \tag{37}$$

While in a quasi-stationary state, the flow variables can be used to identify distinct regions in the black hole accretion disk. The magnetised funnel can be identified by the minimum magnetisation $\sigma = 0.1$, while the disk is the region demarcated by the equalisation of gas and magnetic pressures $\beta = 1$. In addition, the jet sheath is identified by the region between the geometric Bernoulli criterion $u_{\mathrm{t}} = -1$ and the magnetised funnel criterion $\sigma = 1$. Although not the focus on this thesis, if the jet-disk boundary is defined as $\sigma = 1$, high-resolution runs of numerous different GRMHD simulations have shown that this boundary is very clearly defined between $\theta = 10^\circ$ and $\theta = 15^\circ$, where θ is the polar angle of the disk-jet boundary (Porth, 2019). The displayed data in the following figures use GRMHD simulations with a spin parameter of $a = 0.96875$, close to a maximally spinning Kerr black hole. Negative spin (retrograde) parameters describe anti-aligned disk angular momentum vector and black hole spin vector. Kerr black hole simulations with a negative spin show much larger emission regions than for positive spin or zero spin. AGN stochastic evolutionary models predict retrograde black holes with antiparallel angular momenta can be produced by misalignments caused by a kick from the initial progenitor supernova (e.g., Dauser et al., 2011; Volonteri et al., 2005). However, close to the black hole, misalignments will eventually evolve into one of the parallel or antiparallel stable configurations of angular momenta through the Bardeen-Petterson effect (Bardeen and Petterson, 1975). Nevertheless for the purpose of these models, assumptions have been made that the disk angular momentum and black hole spin vector are aligned on large scales, despite abundant evidence in existing literature for misaligned AGN accretion disks (e.g., Miyoshi et al., 1995).

The simulation time chosen to evaluate the flow quantities is the GRMHD snapshot at $t = 7000\,M$, although any time chosen after $t = 6000\,M$ is appropriate. This particular time is chosen because the code mass accretion rate is normalised so that the flux at $t = 7000\,M$ is 0.5 Jy.

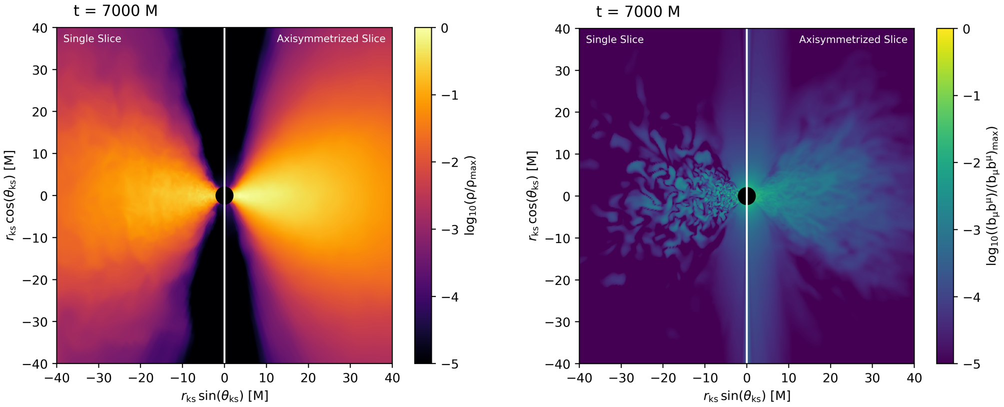

(a) Density *(b) Magnetic Field Strength*

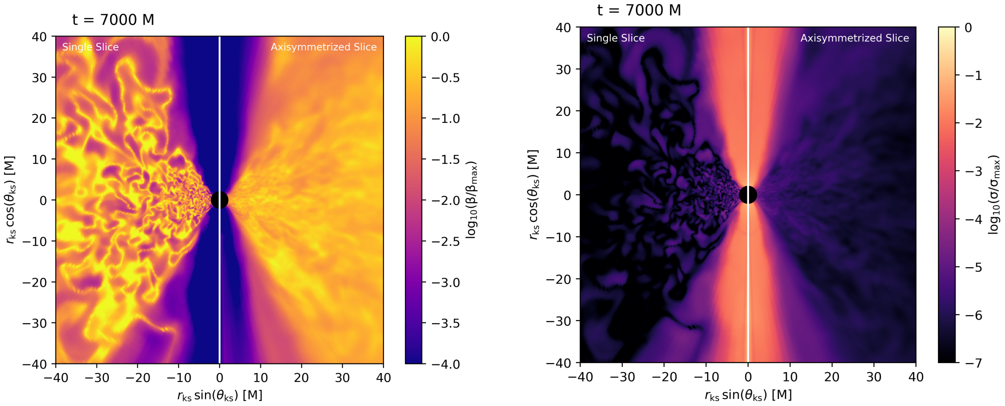

(c) Plasma Beta *(d) Magnetisation*

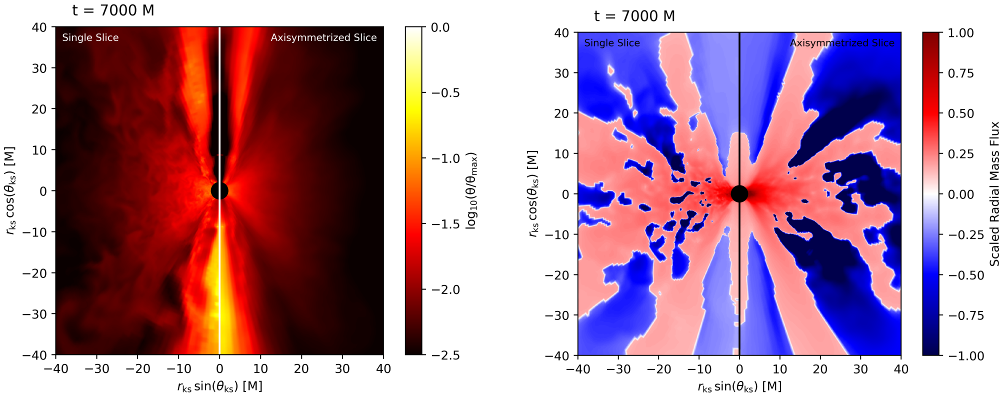

(e) Ion Temperature *(f) Mass Flux*

Figure 8: *Flow quantities calculated from BHAC GRMHD data at time $t = 7000M$. The data is shown in logarithmic scale as shown by the color bar and graphed in Kerr-Schild coordinates. The left side of each figure shows a single slice at $\phi = 0$ while the right side is azimuthally averaged. The event horizon of the black hole is depicted as a black disk and the white (or black) vertical line separates the single-slice quantities from the averaged quantities.*

In Fig. 8, the density, magnetic field strength, plasma beta, magnetisation, ion temperature, and mass flux are shown in Kerr-Schild coordinates and logarithmic scale. These values are chosen specifically to represent the state of the accretion structure and dynamics at the chosen time. The density (top left panel) shows the relative population of accretion plasma at various distances from the black hole. The jet funnel is evacuated and mostly dominated by the floor model for density. The magnetic field strength (top right panel) and magnetisation (middle right panel) shows how the jet funnel is a strongly magnetised region dominated by the magnetic field. The plasma rotation in the funnel is controlled by the black hole dragging magnetic field lines (Akiyama, 2019c). On each figure, the left image shows the turbulence in each slice, while the right axisymmetrised image shows how the turbulence averages out over the ϕ axis. The plasma beta (middle left panel) shows that in the plane of the disk, the plasma pressure is significantly greater than magnetic pressure, while the opposite is true for the jet funnel. Under ideal GRMHD, the magnetic fields are frozen-in to the fluid elements, so the plasma beta gives a look into the accretion dynamics responsible for motion and weighing the strength of the plasma pressure against magnetic pressure.. The ion temperature (bottom left panel) shows how the plasma is hottest in the funnel wall and near to the black hole. Nearest the black hole, the density of plasma rises and the increased friction produces the high temperatures. The temperature decreases as the distance from the center of the black hole increases. Because of the low density, the plasma temperature in the jet spine is arbitrarily determined by the floor model, hence the asymmetry between the jet and counter-jet (Moscibrodzka, Falcke, and Noble, 2016). The radial mass flux (bottom right panel) shows escaping matter in red and in-falling matter in blue. This shows the radial flow direction of accretion plasma in the vicinity of the black hole.

The figures are constructed from data retrieved from the GRMHD output files, where the data retrieval script was written in Fortran90. Then, the matplotlib module in Python2 was used to graph the data which was interpolated in two-dimensions using the mlab sub module function griddata. Since the GRMHD data is stored in cells equally spaced in Kerr-Schild coordinates, the data is mapped and then linearly interpolated onto an equally spaced Cartesian grid where each square cell has a side length of 0.1 M. The grid is then transposed and rotated 90 degrees to be displayed in the orientation shown in Fig. 8. For each quantity, a single slice of data evaluated at $\phi = 0$ is shown on the left, while the axisymmetrised slice is shown on the right. Quantities are scaled according to the single-cell maximum value in each image, where the single-slice and axisymmetrised slice are treated separately with their own respective maximum quantities. This remains true for the mass flux, except that negative flux values are scaled to the minimum value before the logarithm is applied and a negative sign is artificially placed after, such that $x = -\log_{10} \dot{M}/\dot{M}_{\rm min}$ for $\dot{M} < 0$. Then the reciprocal of the value is taken before the color scale is applied. Thus, red positive values represent out-flowing material and blue negative values represent in-flowing material, while higher colour saturation represents a greater mass flux magnitude.

3.2.1 Radial Profile

The radial profiles of flow variables can be obtained and averaged temporally using the following:

$$\bar{q}(r) := \frac{\int_{t_{\rm beg}}^{t_{\rm end}} \int_0^{2\pi} \int_0^{\pi} q(r,\theta,\phi,t)\sqrt{-g}\, d\theta\, d\phi}{(t_{\rm end} - t_{\rm beg}) \int_0^{2\pi} \int_0^{\pi} \sqrt{-g}\, d\theta\, d\phi}, \tag{38}$$

where the chosen quantities of $q(r, \theta, \phi, t)$ represents either the density, ion temperature, or magnetic field strength. The radial profile shows how these quantities change with distance from the black hole. We expect that the quantities decrease with a power-law relationship against the radial distance, which would appear as a straight line with a negative slope on a log-log scale plot. In Fig. 9, the three quantities are graphed together and scaled to their respective maximum values across simulation time, beginning from $t = 6000M$ to $t = 10000M$. The solid lines represent the mean quantity at that radius and the sheath shows the one sigma standard deviation over time. The dependence on radius is $\rho \propto r^{-3}$ far from the black hole and $\theta_{\rm ion} \propto r^{-1}$ as shown in the figure.

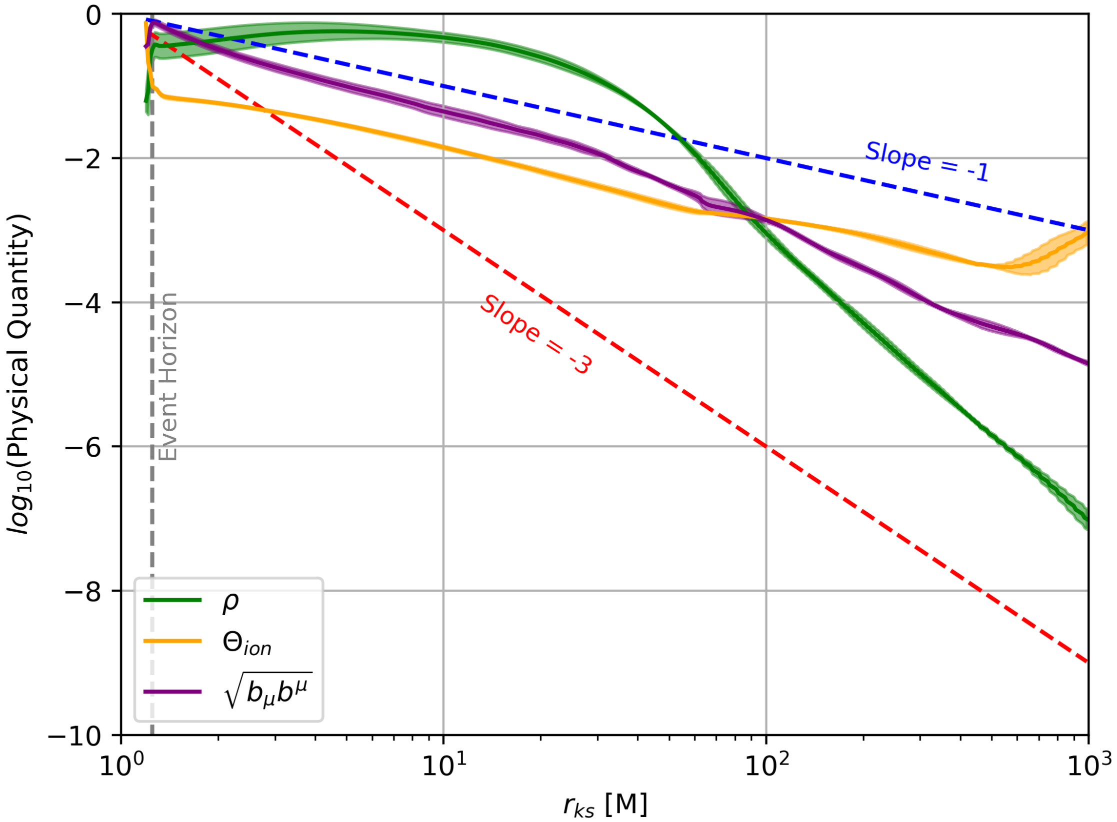

Figure 9: *Time-averaged radial profile of density, ion temperature, and magnetic field strength, where the solid lines show the mean quantity and the translucent bars show the one-sigma standard deviation. Each quantity is scaled with respect to their global maximum value. The radial axis is graphed in logarithmic scale and the event horizon is shown by the grey dotted line. The density follows a* r^{-3} *curve far from the black hole and the ion temperature follows a* r^{-1} *relationship.*

The magnetic field is approximately proportional to the inverse square of the radius or $\sqrt{b_\mu b^\mu} \propto r^{-2}$. The triple-point observed near $r_{\mathrm{ks}} = 100M$ is not physically significant as each value is scaled to their own respective maximum quantities with their own power law relationships, such that the y-intercept would have determined whether the quantities crossed at all. The data for the ion temperature also experiences a sudden increase near the furthest edge of the figure. This is likely due to the low density of plasma at those distances and is a non-physical result of the GRMHD initial conditions. The figures of this chapter are representations of the data which will be used in the coming chapters to solve for emission from the black hole.

4 General-Relativistic Radiative Transfer of M87*

The emission from the accretion flow in the vicinity of Kerr black holes are produced by accelerating charged particles (Luminet, 1979; Morgan et al., 2007). Depending on the opacity of the disk, the accretion can be classified into hot and cold classes. Hot accretion flows radiate with low radiative efficiency and are optically thin, while cold accretion is typically optically thick with high mass accretion rates (Yuan and Narayan, 2014). The ionized plasma influenced by magnetic fields around accreting black holes produce bremsstrahlung and synchrotron radiation. Since synchrotron radiation is a single-body process of an electron interacting with a magnetic field while bremsstrahlung is a two-body process with a quadratic dependence on the number density, it is expected that the emission from the bremsstrahlung process is insignificant compared to synchrotron emission at the observation frequencies of interest (Abramowicz and Fragile, 2013) due to the low number densities. Therefore, bremsstrahlung radiation is omitted in both thermal and non-thermal considerations of synchrotron radiation in later sections. Emission from inverse Compton scattering are also neglected, because Comptonized photons which have been up-scattered to higher energies become more relevant at higher frequencies. For low frequency observations made in the 43, 86, 230, and 345 GHz frequency bands, these photons are not considered.

The fast moving, high energy plasma in the strong gravitational field around Kerr black holes presents a challenge for the conventional radiative transfer formulation. The emission from the accreting gas and outflows is subject to relativistic dynamical effects, such as Doppler shifts, gravitational lensing, and time-dilation. General-relativistic radiative transfer (GRRT) was developed to keep track of radiation transport in the highly relativistic and strong gravitational field regime. The covariant formulation is derived from first principles such as the conservation of particle number and phase-space density (Younsi, Wu, and Fuerst, 2012). It is general with the ability to be applied to a wide range of astrophysical applications. The general covariant formulation can be reduced back to the conventional Newtonian form and can be applied to particles with or without mass. For the accretion emission around the strong gravitational fields and energetic plasma around Kerr black holes, the GRRT formulation will be used to present an accurate and consistent account of radiation transport.

Within this section, the two-temperature model between ions and electrons for synchrotron emission will be discussed. In addition, the covariant radiation transfer equation will be presented for applications in arbitrary spacetime geometry. Next, the thermal and non-thermal emissivities and absorptivities will be shown along with a discussion of the region where non-thermal electrons are to be placed. Finally, photon trajectories are calculated around the Kerr black hole by tracing null geodesics. Their tracks will be plotted in 3D along with two-dimensional projections which compare Schwarzschild and Kerr black hole null geodesics.

4.1 Electron Temperature Model

In synchrotron radiation, free electrons are accelerated by magnetic fields, which causes them to travel in circular or helical trajectories described by a characteristic Larmor frequency and radius (Rybicki and Lightman, 1986). For relativistic velocities, the Larmor angular frequency and radius are

$$\begin{aligned} \omega_{\mathrm{B}} &= \frac{eB}{\gamma m_{\mathrm{e}} c}, \\ r_{\mathrm{L}} &= \frac{\gamma m_{\mathrm{e}} c^2 \beta}{eB}, \end{aligned} \tag{39}$$

where $\beta \equiv v/c$ and $\gamma \equiv 1/\sqrt{1-\beta^2}$ are the typical velocity and Lorentz factor defined for relativistic applications. In comparison, the cyclotron frequency is defined as

$$\nu_{\mathrm{b}} = \frac{eB}{2\pi m_{\mathrm{e}} c}\,, \tag{40}$$

in the non-relativistic limit of $\gamma = 1$. Only the contribution of electrons to the radiation is considered because electrons experience greater accelerations and angular frequency in a tighter gyroradius due to their significantly lower mass $m_\mathrm{p}/m_\mathrm{e} \approx 1836$. The total power output radiated by an accelerated electron is described by the relativistic Larmor formula:

$$P = \frac{2e^2\gamma^6}{3c}\left[\dot{\beta}^2 - \left(\beta \times \dot{\beta}\right)^2\right]. \tag{41}$$

When applied to synchrotron radiation, the power output can be expressed as

$$P_\mathrm{syn} = \frac{4}{3}\sigma_\mathrm{T} c \beta^2 \gamma^2 U_\mathrm{B} \sin^2\alpha, \tag{42}$$

where U_B represents the magnetic energy density and α is the pitch angle between the velocity of the electron, β, and the direction of the magnetic field vector.

In the two-temperature model, most of the thermal energy in ADAF dynamics is stored in the protons, but protons inefficiently exchange energy with the electrons. Thus, protons and electrons are described by different temperatures. However, protons and electrons are assumed to be thermally coupled by a ratio described by (Akiyama, 2019c)

$$\frac{T_\mathrm{p}}{T_\mathrm{e}} = \frac{R_\mathrm{high}\,\beta^2 + 1}{\beta^2 + 1}, \tag{43}$$

where R_high is the only free parameter in the prescription of the temperature ratio since β is determined by the GRMHD simulation data. In low β regions such as the jet funnel, $T_\mathrm{e} \approx T_\mathrm{p}$, whereas in the mid-plane of the disk where β is high, $T_\mathrm{e} \approx T_\mathrm{p}/R_\mathrm{high}$. Deviations in the R_high parameter can introduce additional structures inside and outside the photon ring (Akiyama, 2019c). However, time-averaged MAD models are nearly independent on the value of this free parameter, but SANE images in contrast are highly dependent on R_high. When the value is low, additional structures show extended emission outside the photon ring, but when the value is high, the jet funnel wall contributes to the emission from the photon inner ring (Akiyama, 2019c).

The parameter $R_\mathrm{high} = 10$ was chosen to form the relation between ion and electron temperature. While this assumption is adequate for the accretion disk due to sufficient time to thermalise in slow accretion flows, the assumption is expected to break down for the highly-magnetised and high velocity region of relativistic jets near the Kerr black hole poles. For black holes such as Sgr A*, large scale jets are not observed and observations fit the predictions for disk-dominated models (Issaoun, 2019). However, for the black hole at the centre of M87, an extended plasma jet is observed and additional considerations are required. Some models such that the one found in Moscibrodzka and Falcke, 2013 use a single dimensionless temperature model for electron temperature inside the jet. This model is capable of reproducing the flat radio spectrum of jets in simulations, but as will be discussed in more detail in a later section, the jet funnel region will be excluded from emission. Thus, the flat radio core model is not used in this thesis.

4.2 Radiative Transfer

The specific intensity, I_ν, varies along the length of a ray,

$$\frac{dI_\nu}{ds} = -\alpha_\nu I_\nu + j_\nu, \tag{44}$$

depending on the emission and absorption coefficients j_ν and α_ν respectively (Rybicki and Lightman, 1986). These coefficients may be expressed in terms of the Einstein coefficients, which modify the transition probability per unit time of absorption B_{12}, spontaneous emission A_{21}, and stimulated emission B_{21}. Using a two-level system described by the subscripts 1 and 2, and a frequency-dependent line profile $\phi(\nu)$, the emission coefficient is

$$j_\nu = \frac{h\nu_0}{4\pi} n_2 A_{21} \phi(\nu)\,, \tag{45}$$

while the absorption coefficient is

$$\alpha_\nu = \frac{h\nu}{4\pi} n_1 B_{12} \phi(\nu)\,, \tag{46}$$

where n_1 and n_2 are the number densities of atoms in states 1 and 2. By defining the optical depth as $d\tau_\nu = \alpha_\nu ds$ and the source function as $S_\nu \equiv j_\nu/\alpha_\nu$, the radiative transfer equation can be written as

$$\frac{dI_\nu}{d\tau_\nu} = -I_\nu + S_\nu, \tag{47}$$

where the source function S_ν can also be rewritten in terms of the Einstein coefficients

$$S_\nu = \frac{n_2 A_{21}}{n_1 B_{12} - n_2 B_{21}}. \tag{48}$$

The Einstein relations connect the properties of the Einstein coefficients using detailed radiation balance. When the number of transitions per unit time into and out of a state are equal, then

$$\begin{aligned} g_1 B_{12} &= g_2 B_{21}, \\ A_{21} &= \frac{2h\nu^3}{c^2} B_{21}, \end{aligned} \tag{49}$$

where g_n is the statistical weight of the n state. Using Einstein relations, the following generalized Kirchhoff's law is obtained: (Rybicki and Lightman, 1986)

$$S_\nu = \frac{2h\nu^3}{c^2}\left(\frac{g_2 n_1}{g_1 n_2} - 1\right)^{-1}. \tag{50}$$

If the source function is constant, the specific intensity at optical depth τ_ν has an analytical solution:

$$I_\nu(\tau_\nu) = S_\nu + \left(I_\nu(0) - S_\nu\right) e^{-\tau_\nu}. \tag{51}$$

However, because the source function is not constant in practice, the differential equation must be solved numerically. To be applied to arbitrary spacetime geometry, the radiative transfer equation must be written in covariant form. For photons and particles with zero mass, the GRRT equation can be written as (Younsi, Wu, and Fuerst, 2012)

$$\frac{d\mathcal{I}}{d\lambda} = -k_\beta u^\beta \Big|_\lambda \left(-\alpha_{0,\nu} I_\nu + \frac{j_{0,\nu}}{\nu^3}\right)\,, \tag{52}$$

where $\mathcal{I} = I_\nu/\nu^3$ is a Lorentz-invariant intensity. The four-momentum of the massless particle is denoted by k_α. Both $\alpha_{0,\nu}$ and $j_{0,\nu}$ coefficients are evaluated in the local rest frame of the fluid as indicated by the "0" subscript. For the following discussions of thermal and non-thermal emission processes, the "0" subscript will be dropped from the emissivity and absorptivity coefficients.

4.2.1 Thermal Emission Processes

The synchrotron emissivity of a relativistic electron at a particular velocity is given by (Rybicki and Lightman, 1986)

$$j_\nu(\gamma,\theta) = \frac{\sqrt{3}e^2}{2c} \nu_{\mathrm{b}} \sin\theta\, F(x)\,, \tag{53}$$

where γ is the relativistic Lorentz factor and $F(x)$ is a function defined by

$$F(x) \equiv x \int_x^\infty K_{5/3}(t)\, dt\,, \tag{54}$$

where $K_{5/3}$ is the modified Bessel function of order 5/3. The substituted dimensionless variable $x \equiv \nu/\nu_{\mathrm{c}}$, where the relativistic cyclotron frequency is $\nu_{\mathrm{c}} \equiv (3/2)\gamma^2 \nu_{\mathrm{b}} \sin\theta$. The total emissivity at a particular given angle θ of a thermal distribution of electrons is calculated by integrating the emissivity from Eqn. 53 across the Maxwellian distribution of velocities, obtaining

$$j_{\nu,\mathrm{th}}(\theta) = \frac{N_{\mathrm{th}} e^2}{\sqrt{3} c K_2(1/\theta_{\mathrm{e}})} \nu I \left(\frac{x_{\mathrm{M}}}{\sin\theta} \right) , \tag{55}$$

where

$$x_{\mathrm{M}} \equiv \frac{2\nu}{3\nu_{\mathrm{b}} \theta_{\mathrm{e}}^2}, \tag{56}$$

and a new function is defined:

$$I(x_{\mathrm{M}}) \equiv \frac{1}{x_{\mathrm{M}}} \int_0^\infty z^2 \exp(-z) F \left(\frac{x_{\mathrm{M}}}{z^2} \right) dz \,. \tag{57}$$

The total thermal synchrotron emissivity across all angles can be obtained by integrating the expression in Eqn. 55 across an angular distribution of electron velocities. The simplest case of which is an isotropic distribution. Without going into the full derivation, an approximate expression for the thermal synchrotron emissivity is cited from Leung, Gammie, and Noble, 2011, which is

$$j_\nu = N_{\mathrm{e}} \frac{\sqrt{2} \pi e^2 \nu_{\mathrm{s}}}{3 K_2(1/\theta_{\mathrm{e}}) c} \left(X^{1/2} + 2^{11/12} X^{1/6} \right)^2 \exp\left(-X^{1/3} \right) , \tag{58}$$

where $\nu_{\mathrm{s}} \equiv (2/9) \nu_{\mathrm{c}} \theta_{\mathrm{e}}^2 \sin\theta$ with θ representing the angle between the magnetic field vector and the electron velocity, K_2 is the modified Bessel function of 2nd order, θ_{e} is the dimensionless electron temperature, and N_{e} is the electron density. In the semi-relativistic case, the parameter $X = (2kT/3\gamma_0)^{1/2}$, where $\gamma_0 = (4\nu kT/3\nu_{\mathrm{b}} \sin\theta)^{1/3}$. This reduces simply to $X = (2\nu/\nu_{\mathrm{b}})$ for a non-relativistic gas (Petrosian, 1981). The approximate expression is accurate to within 0.2% over the frequencies of interest (Leung, Gammie, and Noble, 2011).

By Kirchhoff's law of thermal emission which applies in local thermodynamic equilibrium (LTE), the number density ratio $\frac{n_1}{n_2} = \frac{g_1}{g_2} \exp\left(\frac{h\nu}{kT} \right)$ such that the absorptivity is related to the emissivity by

$$\alpha_{\nu,\mathrm{th}} = j_{\nu,\mathrm{th}} / B_\nu(T), \tag{59}$$

where $B_\nu(T) = \left(2h\nu^3/c^2 \right) \left[\exp(h\nu/kT_{\mathrm{e}}) - 1 \right]^{-1}$ denotes the source function of a blackbody with temperature T. Using these emission and absorption coefficients to solve the radiative transfer equation numerically along the photon geodesics derived from the Kerr metric, images of the thermal radiation from the black hole accretion disk may be obtained. Later sections show thermal images made using parameters of M87* which can be compared against the EHT observations in Fig. 1.

4.2.2 Non-Thermal Emission Processes

The total emissivity of electrons which obey a power-law distribution is obtained by averaging the expression from Rybicki and Lightman, 1986 across all angles, resulting in (Ozel, Psaltis, and Narayan, 2000)

$$j_{\nu,\mathrm{pl}} = C_{\mathrm{pl}}^{\mathrm{j}} \eta \frac{e^2 N_{\mathrm{th}}}{c} a\left(\theta_{\mathrm{e}}\right) \theta_{\mathrm{e}} \nu_{\mathrm{b}} \left(\frac{\nu}{\nu_{\mathrm{b}}} \right)^{(1-p)/2} , \tag{60}$$

where the efficiency, η, is taken to be $\eta = 0.1$ and the power law index used is $p = 2.3$. The number density of electrons in a power-law distribution, N_{pl}, is related to the thermal population, N_{th}, by

$$N_{\mathrm{pl}} = \eta a(\theta_{\mathrm{e}}) \theta_{\mathrm{e}} (p-2) N_{\mathrm{th}} \,, \tag{61}$$

where the coefficient $a(\theta_{\mathrm{e}})$ is derived from the dimensionless electron temperature θ_{e} and can be approximated by

$$a(\theta_{\mathrm{e}}) \approx \frac{6 + 15\theta_{\mathrm{e}}}{4 + 5\theta_{\mathrm{e}}}, \tag{62}$$

with less than a 2% error for all temperatures. The coefficient $C^{\mathrm{j}}_{\mathrm{pl}}$ is dependent on the power law index p by

$$C^{\mathrm{j}}_{\mathrm{pl}} = \frac{3^{\mathrm{p}/2}\sqrt{\pi}}{4}\,\frac{(p-1)(p-2)}{(p+1)}\,\frac{\Gamma[(p/4)+(19/12)]\Gamma[(p/4)-(1/12)]\Gamma[(p/4)+(5/4)]}{\Gamma[(p/4)+(7/4)]}, \tag{63}$$

where $\Gamma[x]$ denotes a gamma function of the value x. Because the emission is non-thermal, Kirchhoff's law can not be used to relate the emissivity and the absorptivity by the blackbody source function. Thus, the corresponding absorption coefficient in the power-law distribution is (Ozel, Psaltis, and Narayan, 2000)

$$\alpha_{\nu,\mathrm{pl}} = C^{\alpha}_{\mathrm{pl}}\eta\frac{e^2 N_{\mathrm{th}}}{c}\,a\left(\theta_{\mathrm{e}}\right)\theta_{\mathrm{e}}\nu_{\mathrm{b}}\left(\frac{\nu}{\nu_{\mathrm{b}}}\right)^{(p+3)/2}\nu^{-1}, \tag{64}$$

where the coefficient C^{α}_{pl} is

$$C^{\alpha}_{\mathrm{pl}} = \frac{3^{\mathrm{p}/2}\sqrt{3\pi}}{8}\,\frac{(p-1)(p-2)}{m_{\mathrm{e}}}\,\frac{\Gamma[(3p+2)/12]\Gamma[(3p+22)/12]\Gamma[(6+p)/4]}{\Gamma[(8+p)/4]}. \tag{65}$$

The ratio between the non-thermal and thermal emissivities is (Ozel, Psaltis, and Narayan, 2000)

$$\frac{j_{\mathrm{pl}}}{j_{\mathrm{th}}} = \eta C^{'}_{\mathrm{pl}}a(\theta)K_2\left(\frac{1}{\theta}\right)\theta\left(\frac{\nu}{\nu_{\mathrm{b}}}\right)^{-(p+1)/2}x_{\mathrm{M}}^{1/6}\exp(1.9x_{\mathrm{M}}^{1/3}), \tag{66}$$

where

$$C^{'}_{\mathrm{pl}} = \frac{\sqrt{3}C_{\mathrm{pl}}}{4}, \tag{67}$$

and other quantities are defined as before. This ratio, which is dependent on the expressions for x_{M}, θ_{e}, and ν_{b}, can be calculated to determine whenever the non-thermal emission dominates over the thermal emission when $j_{\mathrm{pl}}/j_{\mathrm{th}} > 1$ and the opposite case for $j_{\mathrm{pl}}/j_{\mathrm{th}} < 1$. Since the emission is optically thin at the higher frequencies, this ratio also depends sensitively on the power-law index given by p. When η is small, the thermal emission dominates over non-thermal emission at frequencies which correspond to the thermal peak of the spectrum.

In non-thermal models of M87* emission, the non-thermal electrons are placed in the region of the black hole bounded by the hydrodynamical Bernoulli parameter, $-hu_{\mathrm{t}} > 1.02$, as previously mentioned. Below the Bernoulli parameter, only thermal synchrotron emissivity and absorptivity are applied. Fig. 10 shows the hydrodynamical Bernoulli parameter $-hu_{\mathrm{t}} = 1.02$ contour in black and the dimensionless magnetisation $\sigma_{\mathrm{min}} = 0.1$ contour in green. The minimum magnetisation of the jet marks the extent of the jet funnel and only the emission with lower magnetisation than the jet minimum is considered. If no minimum magnetisation is imposed, the models show extremely large luminosities which exceed measurements of M87* at all frequencies (Chael, Narayan, and Johnson, 2019). The area to the right of the green magnetisation contour have a low enough value of magnetisation to be considered for thermal or non-thermal emission. In the right panel, bluer regions represent thermal electrons while red regions consist of non-thermal electrons. Altogether in the non-thermal model, power-law electrons are inserted in between the green and black contours. Close to the black hole, the non-thermal emitting region is small, but at larger scales, there is a much larger emitting region for non-thermal electrons, which matches the observed result from synthetic images. In later discussions, the effect of non-thermal emission is shown to be significant at large scales, while the hybrid model which includes non-thermal electrons is nearly indistinguishable from the purely thermal model on small angular scales.

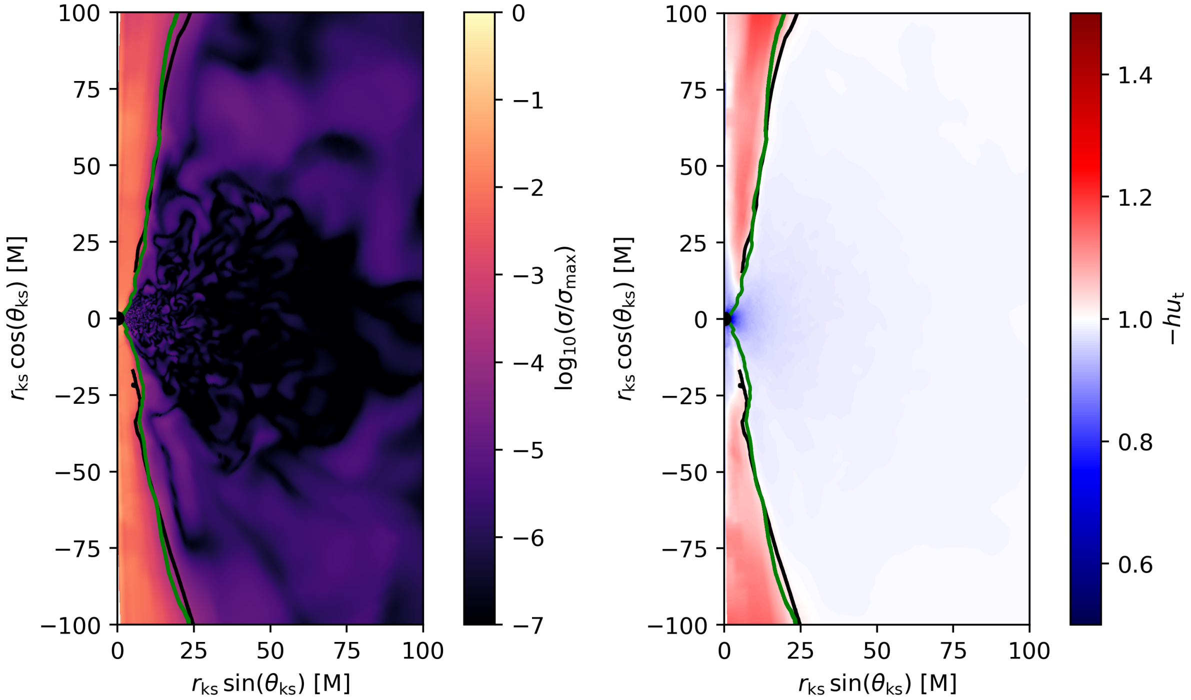

Figure 10: *The left panel shows the magnetisation in logarithmic scale while the right panel shows the hydrodynamical Bernoulli parameter in linear scale. Both figures use GRMHD data at* $t = 7000\,M$ *represented in Kerr-Schild coordinates. The solid black line is determined by* $-hu_t = 1.02$ *while the green line represents the minimum dimensionless magnetisation for the jet funnel where* $\sigma = 0.01$*. GRRT is considered when the magnetisation is below the minimum for the jet and the hydrodynamical Bernoulli parameter is above 1.02.*

Shown in Fig. 10, the space between the two contours defined by the hydrodynamical Bernoulli parameter and the minimum magnetisation consists is where the non-thermal electrons are placed in the non-thermal model of GRRT emission. In the thermal model, those electrons are assumed to radiate thermally as with the electrons from the disk. The radiation from the highly magnetised region of the funnel is ignored from GRRT considerations. The excised region is all of the jet funnel area to the left of the green contour. The next section traces null geodesics around the Kerr black hole to show the photon trajectories which are considered for radiation transport.

4.3 Photon Geodesics and Ray-Tracing

Since photons travel across arbitrary spacetime geometry in null geodesics, it is necessary to solve the GRRT equations along these trajectories. The geodesic equation is

$$\frac{d^2x^\mu}{ds^2} + \Gamma^\mu{}_{\alpha\beta}\frac{dx^\alpha}{ds}\frac{dx^\beta}{ds} = 0\,, \tag{68}$$

where s is a scalar parameter of the motion and $\Gamma^\mu{}_{\alpha\beta}$ are Christoffel symbols which are functions of the metric. As before, Greek indices indicate four components which can take on the values in the range [0, 3], and the summation convention is used for repeated indices. The Christoffel symbols are defined by

$$\Gamma^{\mathrm{a}}{}_{\mathrm{bc}} = \frac{1}{2}g^{\mathrm{ad}}(g_{\mathrm{cd,b}} + g_{\mathrm{bd,c}} - g_{\mathrm{bc,d}}), \tag{69}$$

using the comma to indicate a partial derivative with respect to a coordinate with the index,

$$g_{\mathrm{ab,c}} = \frac{\partial g_{\mathrm{ab}}}{\partial x^{\mathrm{c}}}. \tag{70}$$

The following images show the photon geodesics in vacuum around a black hole of spin $a = 0.9375$. The photons are regularly spaced parallel rays which travel in the positive y direction. Any deviations from parallel trajectories are due to the curved spacetime in the black hole vicinity.

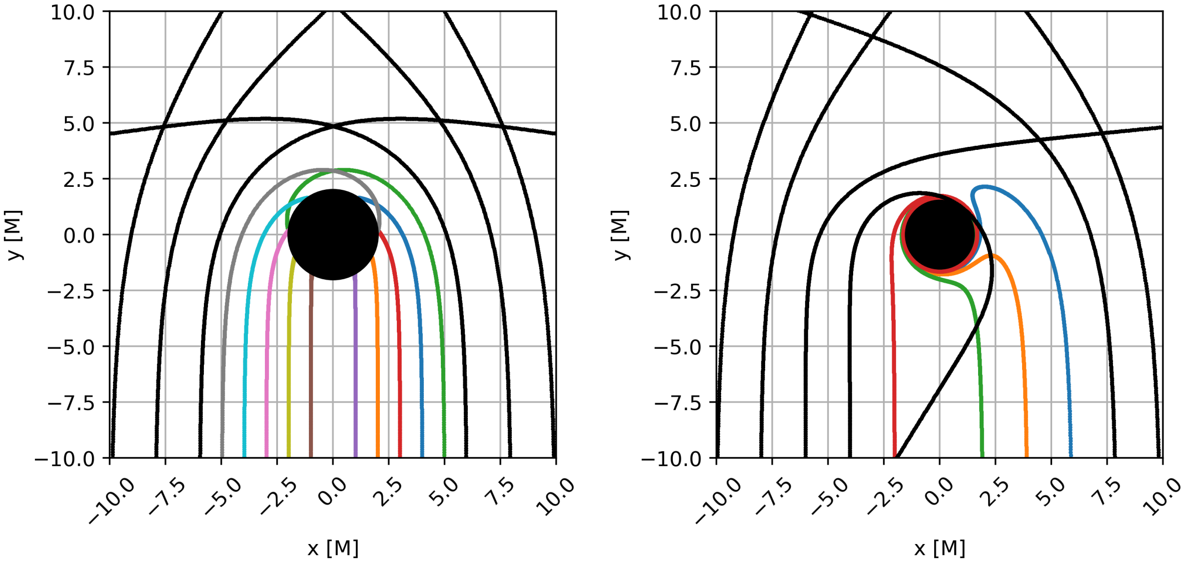

Figure 11: *The figure shows a two-dimensional plot of photon trajectories around a Schwarzschild (left) and Kerr (right) black hole. The Kerr black hole spin parameter is* $a = 0.9375$. *The central solid black circle indicates the extent of the black hole event horizon. Coloured paths represent captured photons and black paths represent photons which can escape to infinity. The left panel shows symmetric trajectories while the right panel depicts the asymmetry of geodesics as a result of black hole spin. In addition, the Lense-Thirring effect is shown, where incoming photons from the counter-rotating direction are dragged into the same direction of rotation as the black hole within the ergosphere. These trajectories were computed from the vacuum integration of geodesics around the black hole spacetime geometry as part of the GRRT routine.*

Fig. 11 shows two-dimensional plots of photon trajectories around a Schwarzschild black hole on the left panel and a Kerr black hole on the right panel. Fig. 12 shows a three-dimensional plot of photon orbits around a Kerr black hole. In both figures, the black hole event horizon is indicated by the solid black disk and the Kerr black hole spin parameter is $a = 0.9375$. In the right panel of Fig. 11, the Kerr black hole is rotating in the clockwise direction. Inside the ergosphere defined by Eqn. 7, photon trajectories are dragged into the co-rotating direction of the black hole by the Lense-Thirring effect. For the Schwarzschild black hole, $a = 0$ and the static limit is coincident with the black hole event horizon. Thus, the trajectories are symmetric across the left and right sides of the black hole. In these figures, the observer is placed at a radius of $r = 1000\, r_{\mathrm{g}}$ away from the black hole. In Fig. 12, the coloured trajectories terminate at the event horizon. The region of space which makes up the boundary between captured and escaping photons defines the photon sphere, which is seen by the distant observer as a shadow cast by the black hole (e.g., Luminet, 1979; Falcke, Melia, and Agol, 2000). Although there are analytical solutions to the black hole shadow shape (Grenzebach, Perlick, and Lämmerzahl, 2014), the shadow can be recovered numerically by ray-tracing many captured photon trajectories and systematically moving the ray origin radially outward in small intervals until the photon is no longer captured. Using this method, the shape of the black hole shadow can be computed numerically to the desired precision. The properties of the shadow depend sensitively on the black hole mass, spin, and the observer's orientation with respect to the black hole spin axis

(Takahashi, 2004). Thus, black hole shadows may be used to infer physical properties of the black hole. The asymmetry of the shadow contains information on the black hole spin parameters, while the angular size of the shadow depends on the observer inclination as well as black hole mass and distance. If the shadow is resolved in detail, it is possible to use a geometric models to provide an estimate for the black hole spin. For a detailed discussion regarding the black hole shadow's properties as well as the information that can be obtained from an accurate geometric model of the shadow, refer to my MSc literature review on the topic.

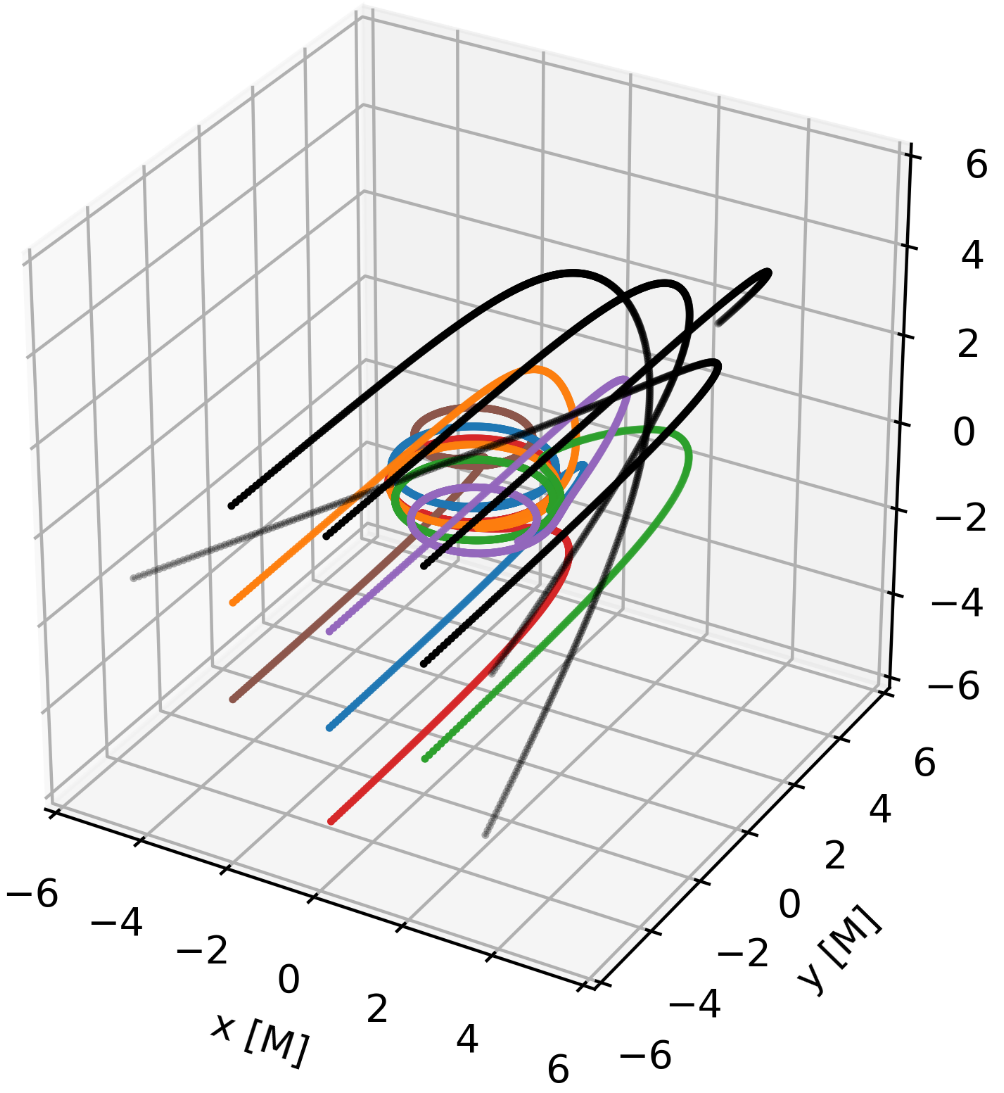

Figure 12: *The figure shows a three-dimensional plot of photon trajectories around a spinning black hole with spin parameter* $a = 0.9375$ *(close to maximal spin). Coloured paths represent captured photons which terminate at the event horizon and black paths represent photons with the potential to escape to infinity. The photons originate from an equally spaced grid travelling parallel along the positive* y *direction. These trajectories were calculated from the vacuum integration of geodesics around the black hole spacetime geometry as part of the GRRT routine.*

5 Synthetic M87* Images

Ray-traced synthetic images of M87* are obtained by the integration of photon geodesics with radiation transport around the Kerr black hole curved spacetime. To produce images of the black hole, geodesic equations of motion are computed in tandem with the GRRT equations (e.g., Younsi, Wu, and Fuerst, 2012). To simplify the calculation, the fast-light approximation is used, where the GRMHD simulation is effectively frozen in time when the GRRT equations are solved. This assumption is reasonable for M87* because the time scale of the black hole evolution is slow compared to the time taken for light to travel across. In the non-thermal model, the non-thermal electrons are placed inside the region bounded by the hydrodynamical Bernoulli parameter and jet funnel minimum magnetisation. See Fig. 10 for the excluded regions as well as the thermal and non-thermal separation. The observing frequency, electron number density, electron temperature, and magnetic field strength are used to determine the emission and absorption coefficients. The GRRT code BHOSS (Younsi, 2019) was used to produce the images in this research thesis. The GRMHD data referred to when running BHOSS is stored in a specially allotted research data storage area provided by UCL HPC. The BHOSS code is submitted in UCL Myriad, which is designed to run high throughput jobs on a single node rather than jobs that require multi-node parallel computing. At each step in affine parameter with BHOSS, a decoupled version of the GRRT differential equation is solved. Similar to how the photon vacuum geodesics were determined in Figs. 11 and 12, photon trajectories are reverse ray-traced from the observer at $r = 1000\, r_{\rm g}$ to the black hole. The jet funnel region is excised from radiation transport as GRRT is only considered in regions where the dimensionless magnetisation is lower than the minimum of the jet funnel as the density of plasma within the funnel is often dominated by the floor model. Thus, the two temperature ADAF model may be used throughout the GRRT simulation. It is important to note for the non-thermal synthetic images that numerical errors from photons passing through the jet spine can be caused by issues with the Riemann problem while inverting conserved variables into primitive variables.

GRMHD data from a Kerr black hole with $a = 0.96875$ under SANE is used at times $t > 6000M$. Specifically, the times chosen to run the GRRT code are $t = [6570, 7020, 7790, 8090]\, M$ as they are periods which reflect local maxima and minima in 230 GHz flux for an observer with inclination angle of $\theta_0 = 163^\circ$. An explanation for how these times were chosen is in Section 5.4. All images run with the GRRT code were chosen to be run at a resolution $W = 2048$ pixels to remain consistent. The GRMHD data from these specific time snapshots were used to generate both thermal and non-thermal synthetic images so that the models can be compared directly. In the post-processing procedure, images were rotated to correspond to $\phi = 288^\circ$ East of North as was observed for M87*. Since the images were originally square, the image size had to be confined within a new width equal to $w' = w(\cos(\phi_{90}) - \sin(\phi_{90}))$, where w' is the new width of the image and w is the original width. In this context, ϕ_{90} represents the angle of rotation from the nearest multiple of 90 degrees. In this case, $\phi_{90} = 18^\circ$, thus images had to shrink by a factor of ~0.64, and the effective resolution of each image decreases to $W \approx 1315$ pixels. This result is consistent for all following thermal and non-thermal images regardless of the original width. The consistent treatment of the images will allow a one-for-one pixel correspondence which is advantageous for computing the thermal and non-thermal image difference in Section 5.3.

Physical parameters of M87* were used to scale the GRRT results appropriately in agreement with the EHT results. The distance to M87* was set as $d = 16.9 \times 10^6\, \mathrm{pc}$ and the mass of the black hole was $M_{\rm bh} = 6.2 \times 10^9\, \mathrm{M}_\odot$. While displaying the synthetic images, the mass and distance to M87* were used to convert the original linear scale measured in gravitational radii to the more observationally relevant microarcsecond scale using the conversion factor $r_{\rm g} = 3.80335\, \mu\mathrm{as}$ for M87*. In addition, code units were calculated for the light-crossing time-scale, characteristic mass density, number density, and Eddington accretion rate based on the M87* parameters. Furthermore, the adiabatic gamma parameter used for the ideal equation of state is $\gamma = 4/3$. The adiabatic gamma parameter is used to calculate the specific enthalpy, which is important in determining whether emission is to be considered thermal or non-thermal.

5.1 Thermal Model

The first case to consider is when all of the emission is thermal. The following images are ray-traced synthetic created using M87* parameters at 230 GHz. The 230 GHz frequency band is significant as it was the observation frequency of the EHT used for producing the M87* image released in April 2019. The data was chosen to be displayed in a linear scale normalised to the value of the maximum flux in each image. The two left panels are local maxima in flux and show flaring events, while the two right panels are local minima. In all four images, the majority of the flux is confined within 40 μas of the black hole center. Recalling that the maximum theoretical resolution of the EHT is $R \approx 26\,\mu$as, the event horizon scale emission of M87* can be resolved. Although there is some plasma obscuring the black hole shadow, an accurate geometric model of its size and asymmetry can be used to constrain the black hole mass and spin as discussed in my research essay. The EHT results show the M87* images in linear scale with brightness temperature instead of flux. Converting from flux to brightness temperature is relatively straightforward, using the expression:

$$T_{\mathrm{b}} = \frac{h\nu}{k_{\mathrm{b}}} \ln^{-1}\left(1 + \frac{2h\nu^3}{F_\nu c^2}\right), \tag{71}$$

where h is the Planck's constant, and k_{b} is the Boltzmann constant. The specific flux at a frequency ν represented by F_ν. In the Rayleigh-Jeans regime where $h\nu \ll k_{\mathrm{b}}T$, the expression can be Taylor expanded and simplified such that

$$T_{\mathrm{b}} = \frac{F_\nu c^2}{2k_{\mathrm{b}}\nu^2}. \tag{72}$$

The brightness temperature represents the temperature of a blackbody radiating in thermal equilibrium which outputs the same observed intensity of the source. Displaying the data in units of brightness temperature is common practice in radio astronomy; however, in the discussion of this research thesis, the data will be normalised with respect to the cell with the maximum value. Therefore, the results will be dimensionless in the range of [0, 1], showing relative rather than absolute quantities. The flux maximum is shown in the images to provide context.

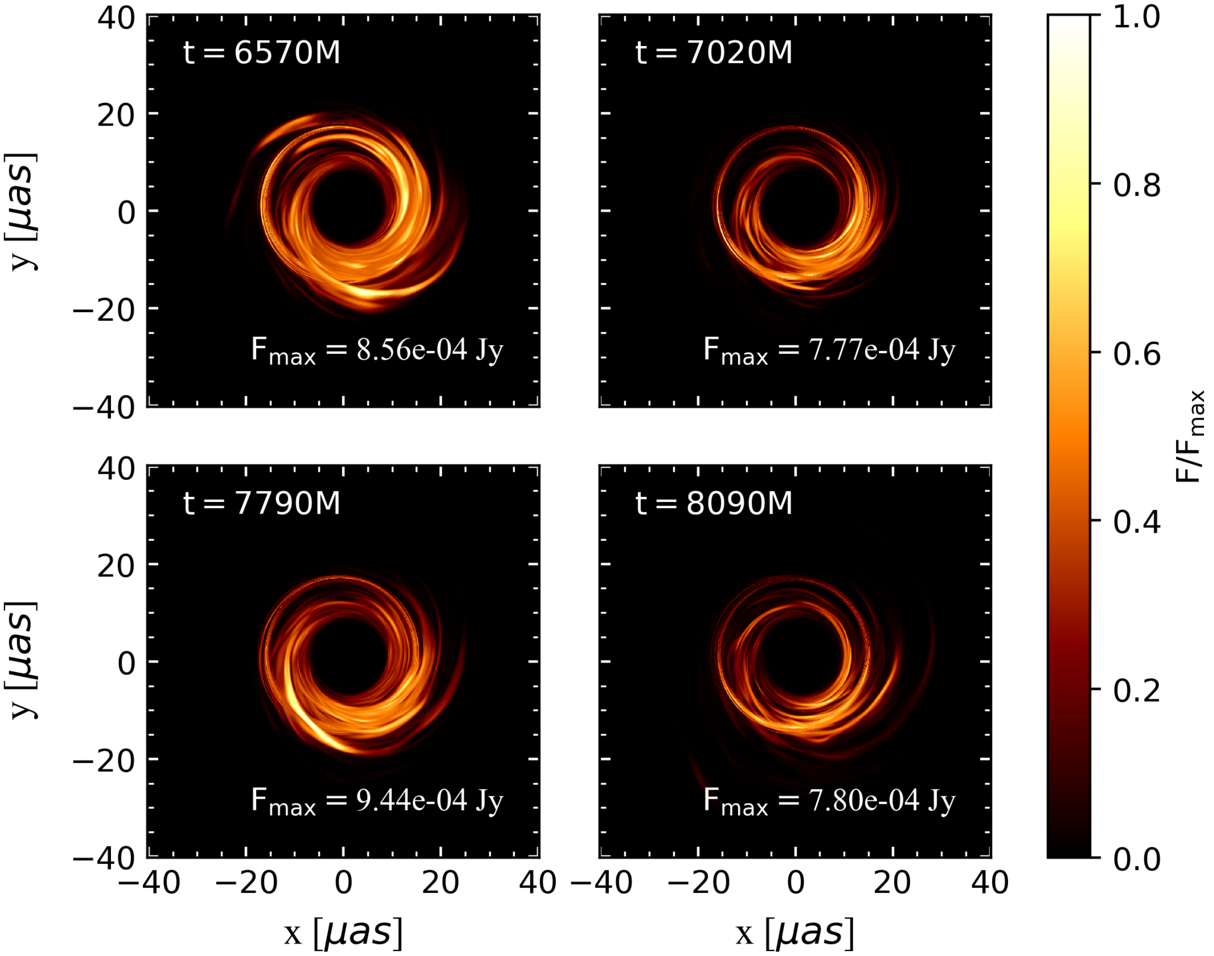

Figure 13: *Ray-traced thermal images of M87* at 230 GHz shown in linear scale. Each image is scaled to the respective flux maximum of that image, where the value of the flux maximum is displayed on the image.The two left panels are local flux maximums showing flaring events and extended features, while the two right panels are local flux minimums. The difference is also reflected in the value of* $F_{\max}$.

A prominent feature in all four panels of Fig. 13 is a bright photon ring surrounding the dark black hole shadow. The bright photon ring represents the gravitationally lensed image of the photon sphere. The incoming light ray from the photon ring, when traced back to the black hole, approaches the bound photon orbit region asymptotically (Gralla, Holz, and Wald, 2019). These photons have orbited the black hole many times before escaping on its way to the observer. Emission from the photon ring is enhanced when optically thin matter forms an emission region close to the unstable bound photon orbits. Over several orbits passing through the emission region, the brightness increases. Distinct from the photon ring is the lensing ring, which consists of light rays that intersect the plane of the disk twice, whereas photon ring consists of light rays which have had three or more such intersections. Outside the lensing ring, the emission travels directly to the observer, but within the lensing ring, the back of the black hole's disk is superimposed with the direct emission. The brightness enhancement factor of the lensing ring typically 2.05 times the brightness of the local environment (Gralla, Holz, and Wald, 2019).The appearance of these two rings are highly dependent on the specifics of the emission mechanism. Furthermore, because the observer is inclined with respect to the black hole angular momentum vector, the difference in brightness between the top and bottom sections of the photon ring are due to relativistic Doppler boosting. The difference in plasma velocity with respect to the observer which governs the intensity ratio between the top and bottom sections of the photon ring is determined by the observer inclination.

When displaying the image in linear scale at 230 GHz, the difference between the thermal and non-thermal models is nearly indistinguishable. The non-thermal 230 GHz synthetic images are displayed in Fig. 17. One of the reasons shown in Fig. 14 is that the frequency is very close to the thermal spectral peak of M87* where most of the radiation can be accounted for thermally. Compared to a purely thermal model, power-law electrons have two primary effects on the spectral model. In the low frequency regime, there is a shoulder of optically thick emission. At high frequencies, there is an extended tail of optically thin emission. In both regions, the power-law emissivity emissivity is greater than the thermal emissivity, that is the emissivity ratio defined earlier $j_{\mathrm{pl}}/j_{\mathrm{th}} > 1$. The non-thermal luminosity can be up to two orders of magnitude greater than the thermal model within the low frequency shoulder and the difference is even more pronounced in the high frequency tail. In between the two regimes, the thermal emission is the dominant radiation mechanism (Ozel, Psaltis, and Narayan, 2000).

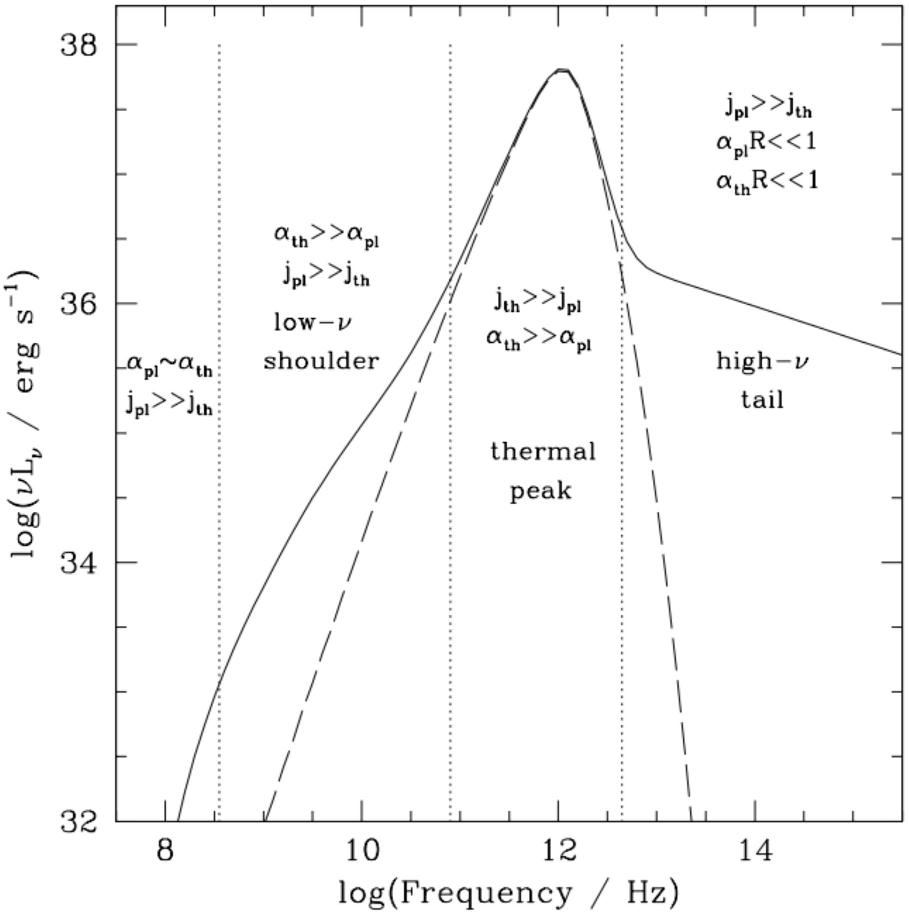

Figure 14: *Spectral model of a hybrid population of thermal and non-thermal electrons shown for $p = 3.5$ and $\eta = 0.01$. The dashed line represents the spectral shape of a purely thermal model while the solid line shows the hybrid model spectral shape. In the low frequency regime, the non-thermal emissivity contributes to the emission, resulting in a "shoulder", while in the high frequency regime, the non-thermal emission contributes to a long power-law tail in the spectral model. Near the thermal peak, the thermal electrons account for the majority of emission. Figure is obtained from Ozel, Psaltis, and Narayan, 2000.*

Another reason that the difference between the two models might be qualitatively unobservable is that in linear scale, most of the observable flux is within $r = 50\,M$ of the black hole, where the radiative power of thermal and non-thermal electrons does not differ significantly. At larger radii, the non-thermal model is known to have much greater radiative power (Chael, Narayan, and Sadowski, 2017). As part of the discussion of Fig. 10, the non-thermal emitting region was shown to increase at larger angular scales. Thus, in order to observe the differences between the thermal and non-thermal models, GRRT simulations were run in the 43 GHz frequency and emission was graphed in a logarithmic scale. The scale size of the image under VLBI is proportional to the inverse of the frequency. Also at the lower frequencies, the accretion disk is optically thick such that we are unable to observe as deeply into event-horizon scale emission as with frequencies at the higher end of the radio spectrum as 230 GHz. Naturally as the frequency decreases to 43 GHz, the width of the image has to be expanded to observe larger-scale structures. The 43 GHz frequency is also important as the Very Long Baseline Array (VLBA) has already gathered data in this frequency over seventeen years, which shows long extended kilo-parsec scale jet features for M87* (Craig Walker et al., 2018). These lower frequency observations can be used to study the structure and dynamics of black hole jets.

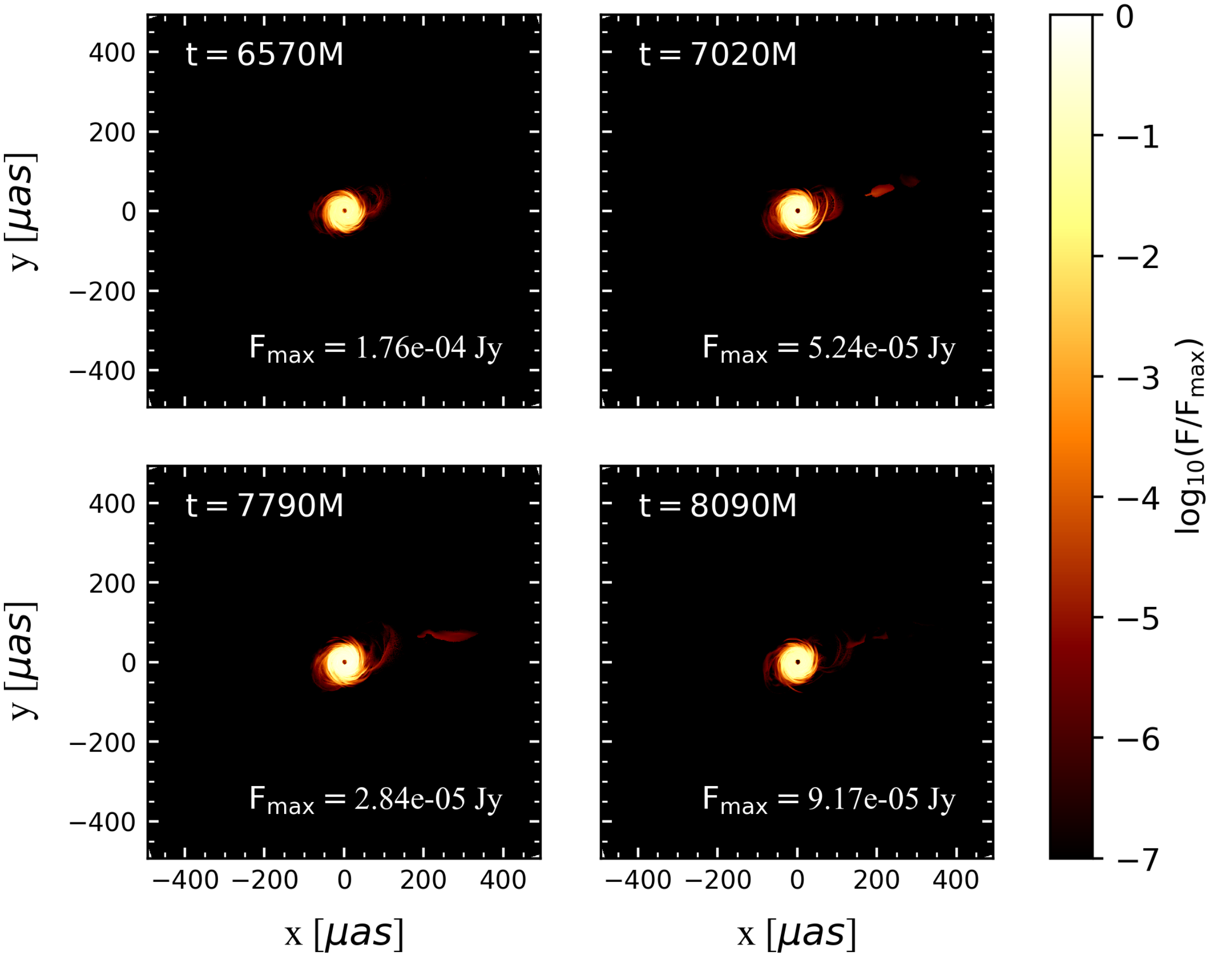

Figure 15: *Ray-traced purely thermal synthetic images of M87* in 43 GHz shown in logarithmic scale. Each image is scaled to the respective flux maximum of that image. Although nearly imperceptible, the larger, more predominant jet is on the right side of each image, while the counter-jet is on the left. Some of the brighter streaks within the jet are features from the jet spine, which are the result of numerical error in the simulation.*

Fig. 15 shows that most of the emission in a thermal SANE model of M87* is confined in within a relatively small angular scale. The jet is the slightly extended emission feature on the right side. Some features of the jet spine appear as bright streaks detached from the compact emitting region, which are the non-physical result of numerical error in the simulation. In the non-thermal model discussion, a corresponding image will be produced for a non-thermal model which shows a much brighter jet. In a later section, the two models will be compared by computing the difference between the 43 GHz images. These results will be compared against the actual VLBA observations.

Another interesting frequency band is 86 GHz, which has been used to observe both Sgr A* and M87*. Emission at this frequency is resolvable with the Global Millimeter VLBI Array (GMVA). In a paper published in January 2019, observations of Sgr A* in 86 GHz made by combining GMVA and Atacama Large Millimeter/submillimeter Array (ALMA) data constituted the first time the scattering broadening effects were sub-dominant to the intrinsic structure of the black hole (Issaoun et al., 2019). These results were used to estimate the morphology of the 86 GHz radio emission as well as the black hole asymmetry. In Fig. 16, synthetic images of M87* in 86 GHz are shown.

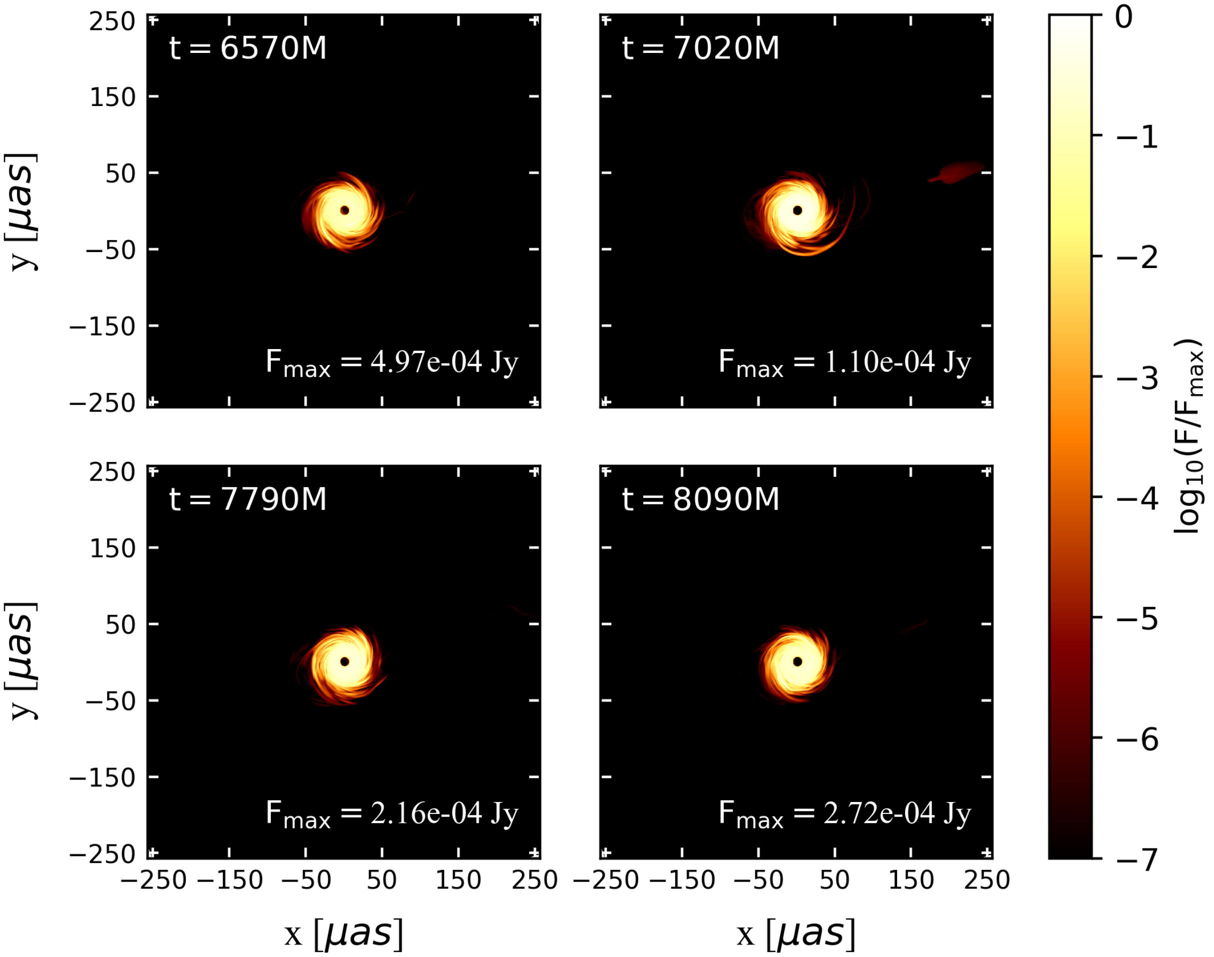

Figure 16: *Ray-traced purely thermal synthetic images of M87* in 86 GHz shown in logarithmic scale. Each image is scaled to the respective flux maximum of that image. Numerical errors from the jet spine are visible from the jet near the edge of the image in the top right panel.*

Like Fig. 15, most of the emission from the thermal synthetic image of M87* at 86 GHz is confined within a small angular region close to the black hole. In both figures, features from the jet are masked by the much brighter emission from the disk, despite the logarithmic scaling of the data. Non-thermal synthetic images at 86 GHz will also be made and compared against GMVA observations.

From these results, it's apparent that the purely thermal GRRT is appropriate for disk-dominated models or black holes without extended jet emission such as Sgr A*. Most of the emission and emitting area is confined within 50 μas of the black hole with M87* parameters, which is approximately equivalent to ~13 M. However, the diffraction-limited resolution of an interferometer scales with the inverse of the frequency such that at 43 GHz, the beam size of EHT is approximately $R = 139\,\mu$as, which is insufficient to resolve M87* if all of its emission features were confined within 50 μas as the thermal model shows. However, in reality, M87* shows kilo-parsec scale jets which have been successfully observed at low frequencies by the VLBA. These observations have been used to study the helical structure of M87* jet flow, polarisation, and magnetic field geometry. Data from the VLBA show that the M87* jet has a wide opening angle at its base with bright edges, while its overall shape is parabolic (Craig Walker et al., 2018). These jets are created by a rapid acceleration of electrons to high Lorentz factors by the magnetic field. In order to account for their emission, the simulation must switch to placing non-thermal electrons within the jet funnel region.

5.2 Hybrid Non-Thermal Model

In the previous section, it was argued that frequencies other than 230 GHz were required to observe emission where the non-thermal and thermal emissivity ratio is greater than unity. Fig. 14 shows a typical hybrid spectral model for $p = 3.5$ and $\eta = 0.01$. Mentioned in the previous section, the parameters used to calculate non-thermal emissivity and absorptivity use a lower power law index with a greater efficiency, $p = 2.3$ and $\eta = 0.1$. These two changes combined increases the non-thermal contribution to emission across all frequencies (Ozel, Psaltis, and Narayan, 2000). Furthermore, at a power law index of $p = 2.3$, the power law tail at high frequencies can extend to much greater luminosities than the thermal peak. Although interesting for high frequency observation, only radio frequencies are considered in this thesis.

Corresponding with Fig. 13, images are produced in 230 GHz using the non-thermal emission model at the same simulation times for direct comparison.

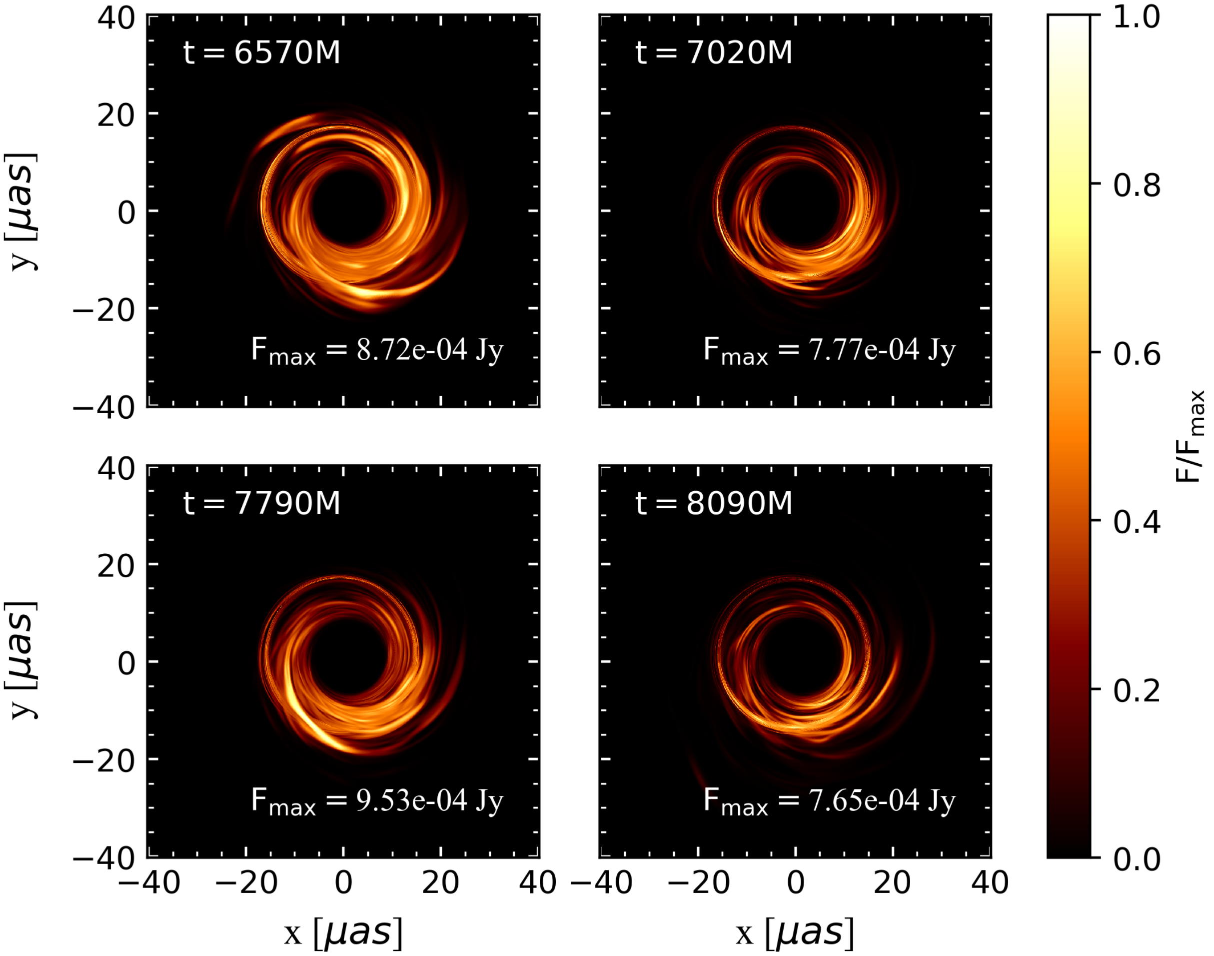

Figure 17: *Ray-traced non-thermal synthetic images of M87* in 230 GHz shown in linear scale. Each image is scaled to the image's respective flux maximum.*

Comparing Fig. 17 against Fig. 13 qualitatively, it may be difficult to determine whether there are any differences aside from the slight modification in the value of the flux maximum for times 6570 M, 7790 M, and 8090 M. Otherwise, most of the emission features inside and outside the photon ring appear to be unchanged when using the non-thermal model. At 230 GHz, most of the emission can be accounted for thermally and at scales of $\pm 40\mu$as, the non-thermal emitting region is small as electrons require some time to be accelerated and become part of the non-thermal population.

When the GRRT code is run at 43 GHz, the difference becomes observable, especially at such large angular scales when the non-thermal emitting area increases. Comparing Fig. 18 against Fig. 15, we find that although both images are shown in the same logarithmic scale with the same depth, the non-thermal jet is significantly larger and more powerful than the thermal jets. The difference between the jet and counter-jet is also apparent in the jet size and opening angle. Worth noting is that although each image is scaled to its own flux maximum, the maximum value between the thermal and non-thermal corresponding snapshots are within the same order of magnitude, which means that the jet emission from the non-thermal model is real and not the product of the normalisation procedure. Furthermore, because of the much lower plasma density in the non-thermal emission region compared to the disk, only a small proportion of the electrons are considered for non-thermal emission. However, even if less than one percent of electron energy is in the non-thermal electrons, the luminosity at large scales can be up to two orders of magnitude greater than the purely thermal model (Ozel, Psaltis, and Narayan, 2000).

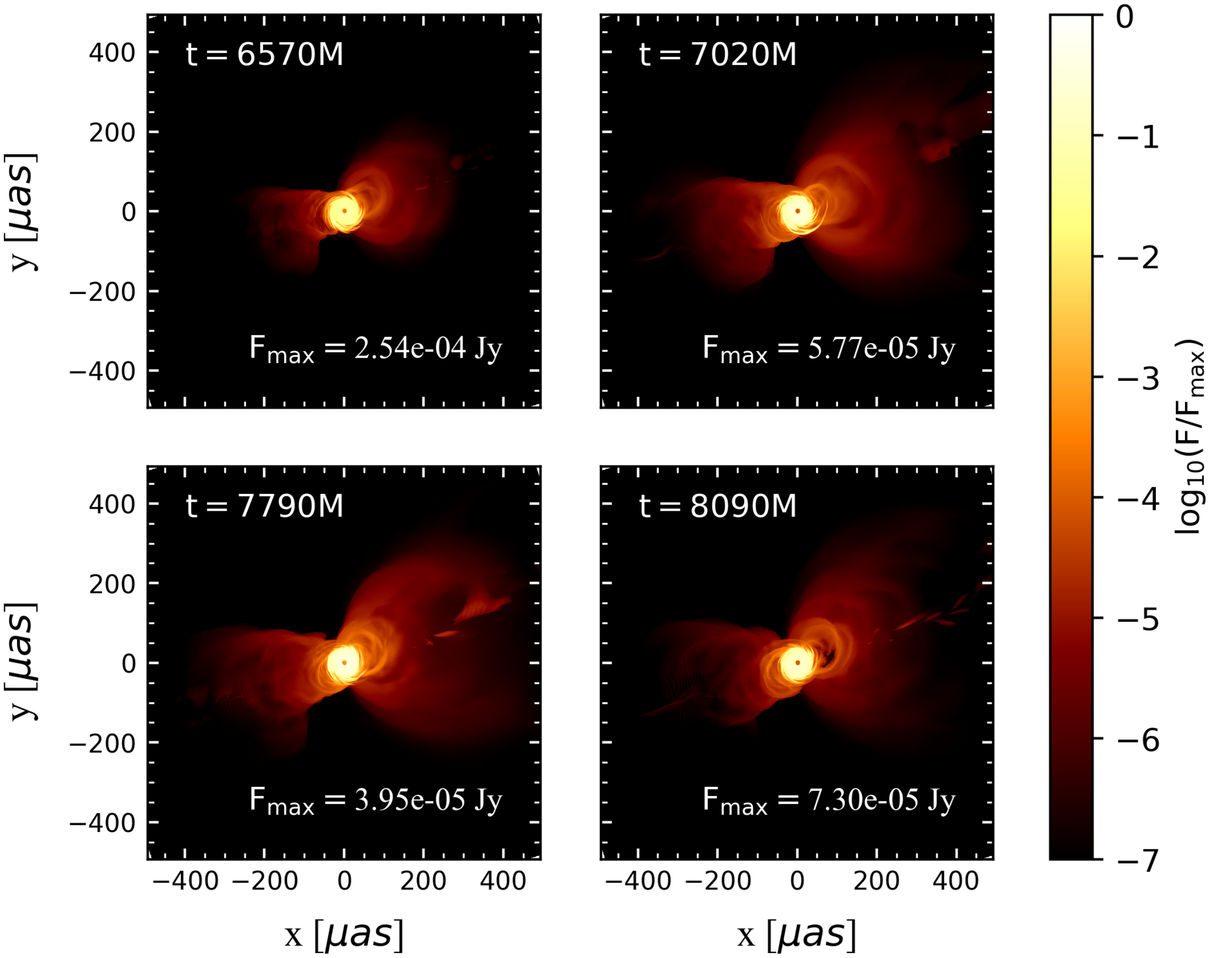

Figure 18: *Ray-traced non-thermal synthetic images of M87* in 43 GHz shown in logarithmic scale. Each image is scaled to the respective flux maximum of that image. The larger, more predominant jet is on the right side of each image, while the counter-jet is on the left. Some of the brighter streaks within the jet are features from the jet spine, which may be the result of numerical error in the simulation.*

In Fig. 18, the jet on the right side of each image and the counter-jet on the left side of each image are extended features which can be seen in logarithmic scale and expanded image width. The jet shape is roughly parabolic in this simulation. Some features of the jet spine which appear as bright streaks in the jet can be dismissed as numerical errors in the simulation. Under the SANE model, the jet simulations have a narrower opening angle than observed for M87*. Furthermore, the measured jet power is several orders of magnitude lower than observation. Evidently, the SANE model is insufficient in describing the origin of the powerful jets. Under the MAD model, magnetic flux builds up against the black hole, which suppresses the rate of accretion and launches powerful jets from the build-up of magnetic pressure. The MAD models show wider opening angles and significantly greater jet power, similar to the observed results. Thus, it is thought that M87* has a magnetically arrested disk close to its core (Chael, Narayan, and Johnson, 2019).

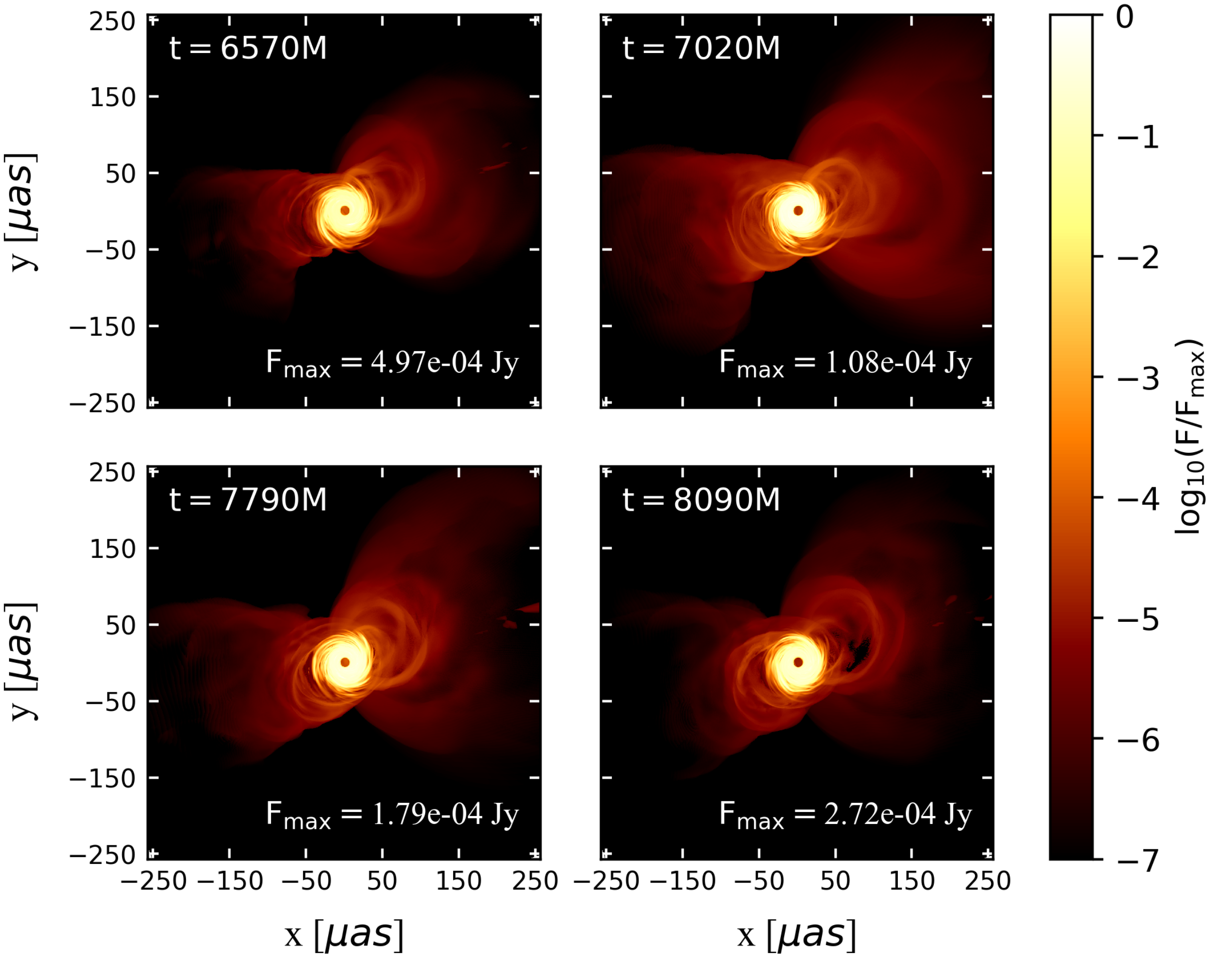

Figure 19: *Ray-traced non-thermal synthetic images of M87* in 86 GHz shown in logarithmic scale. Each image is scaled to the respective flux maximum of that image.*

As with images created at 43 GHz, the jet is an important component of emission at 86 GHz in the non-thermal model. At 86 GHz, the EHT beam size is roughly $R = 70\,\mu$as, which is not deep enough to resolve horizon-scale emission. However, this frequency has been used to measure the intrinsic unscattered source structure of Sgr A* by subtracting the effects of interstellar scattering. Previous analysis of observations from GMVA found Sgr A* to have a major axis size of $120 \pm 32\,\mu$as and symmetric morphology with an axial ratio close to unity. These results represent the most stringent constraints for the morphology of Sgr A* to date, as EHT observations at 230 GHz have yet to be released for this source (Issaoun, 2019). Moreover, it was shown that the emission from Sgr A* matches several disk-dominated models. For M87*, the jet is an important feature which is elongated up to parsec distances. Forward and reverse fast-mode MHD shocks could be responsible responsible for intrinsic motions within the jet. The MHD shock model can also be used to explain the efficiency of diffusive shock acceleration via the first-order Fermi acceleration process (Nakamura and Meier, 2014). However, these kinetic processes have to be considered in a non-ideal GRMHD model.

Although there are many qualitative differences between the thermal and hybrid non-thermal images at 43 GHz and 86 GHz, a more quantitative approach is taken by stacking the images and computing the difference. The following section reviews the method and discusses the differences in detail.

5.3 Thermal and Non-Thermal Difference

The difference between the thermal and non-thermal models was computed by stacking the images cell-by-cell and subtracting the value in the non-thermal cell from the thermal cell. This is possible because the resolution, rotation, and width of each image was kept consistent between the thermal and non-thermal GRRT simulation. As with the radial mass flux image in the bottom right panel of Fig. 8, after taking the difference between the two images, negative flux values are scaled to the minimum value before the logarithm is applied and a negative sign is artificially placed after, such that $x = -\log_{10} \dot{M}/\dot{M}_{\min}$ for $\dot{M} < 0$. Positive values are scaled to the flux maximum and there is no artificially imposed negative sign. The reciprocal of the value is taken before the color scale is applied. Thus, because non-thermal is subtracted from thermal before converting into a normalised logarithmic scale, excess non-thermal synchrotron emission is shown in red (positive values) and excess thermal model emission is shown in blue (negative values).

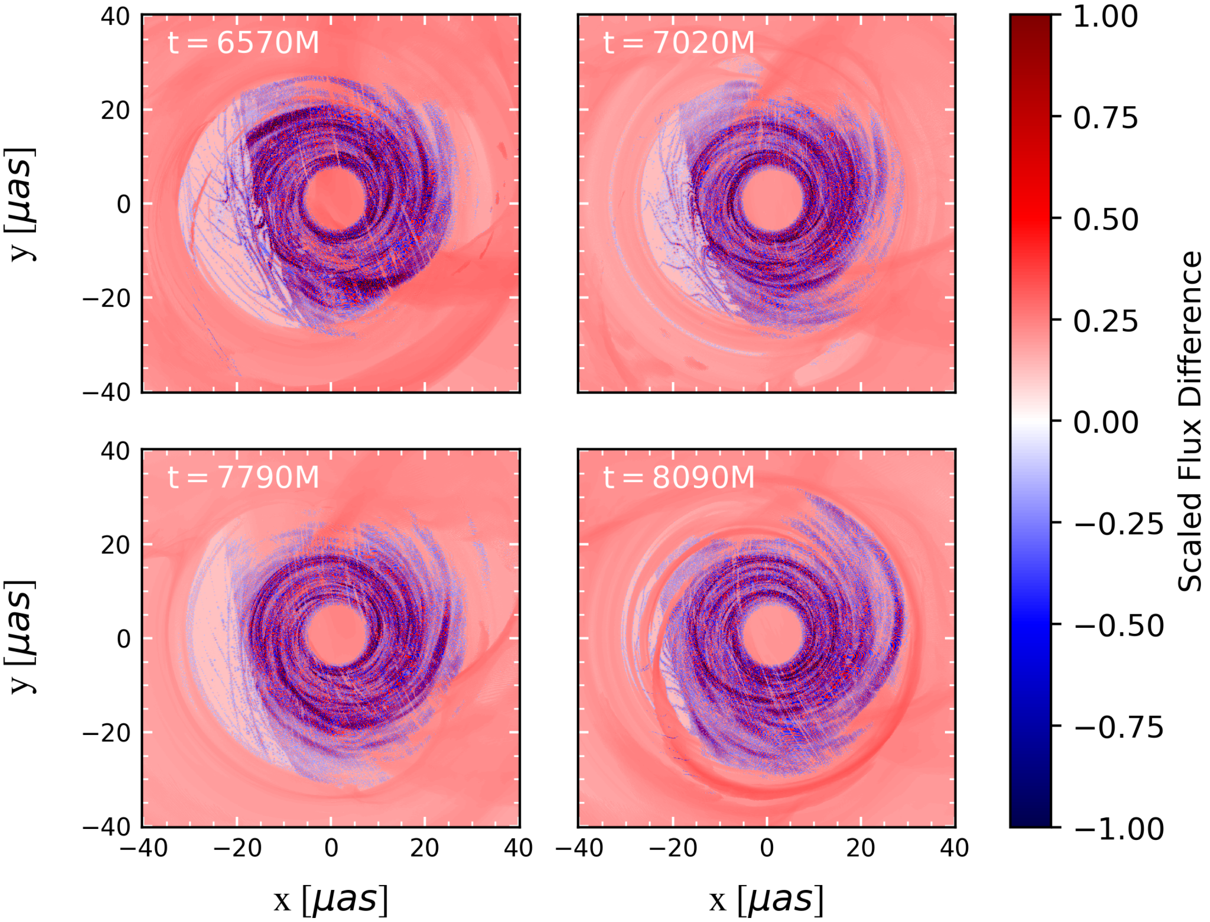

Figure 20: *Difference between the ray-traced thermal and non-thermal images of M87* observed in 230 GHz shown in logarithmic scale. Blue areas represent regions where thermal emission dominates while red areas represent greater non-thermal radiation.*

Although the thermal and non-thermal images had next to no visible differences in the linearly-scaled images, it is clear from Fig. 20 that the thermal emission is stronger than non-thermal emission in most of the area within 20 μas of the black hole, while non-thermal emission dominates beyond 20 μas. From the GRMHD formulation for jets powered by black hole spin, a stagnation surface is predicted where the non-thermal energetic electrons are injected (Pu et al., 2017). In the inflow region, matter cooled by radiative losses and adiabatic cooling falls into the black hole. Within the outflow region, the non-thermal electrons cool quickly due to radiative losses and mechanical cooling until the contribution to the synchrotron emission becomes insignificant further away from the stagnation surface, leading to a finite emitting region. Observing characteristics of the stagnation surface on event horizon scales would be strong evidence for the GRMHD jet model. At the 40 μas image width of M87* observed in 230 GHz, the thermal emission is compact and dominant over the non-thermal emission with $j_{\rm pl}/j_{\rm th} < 1$. However, the effects from even a small proportion of non-thermal electrons can be seen at larger angular scales, where the intensity of thermal emission drops sharply and the remaining non-thermal emission is dominant.

An important remark to make is that electron acceleration mechanisms are not captured by the ideal GRMHD-based simulation (Davelaar et al., 2019). MHD shocks mentioned previously can be an alternative acceleration mechanism, but the non-thermal electrons are located in a region where these shocks are known to be less efficient (Sironi, Petropoulou, and Giannios, 2015). When there is electron acceleration at work, the emission region becomes optically thinner and smaller. Furthermore, the accretion rate and jet power decreases.

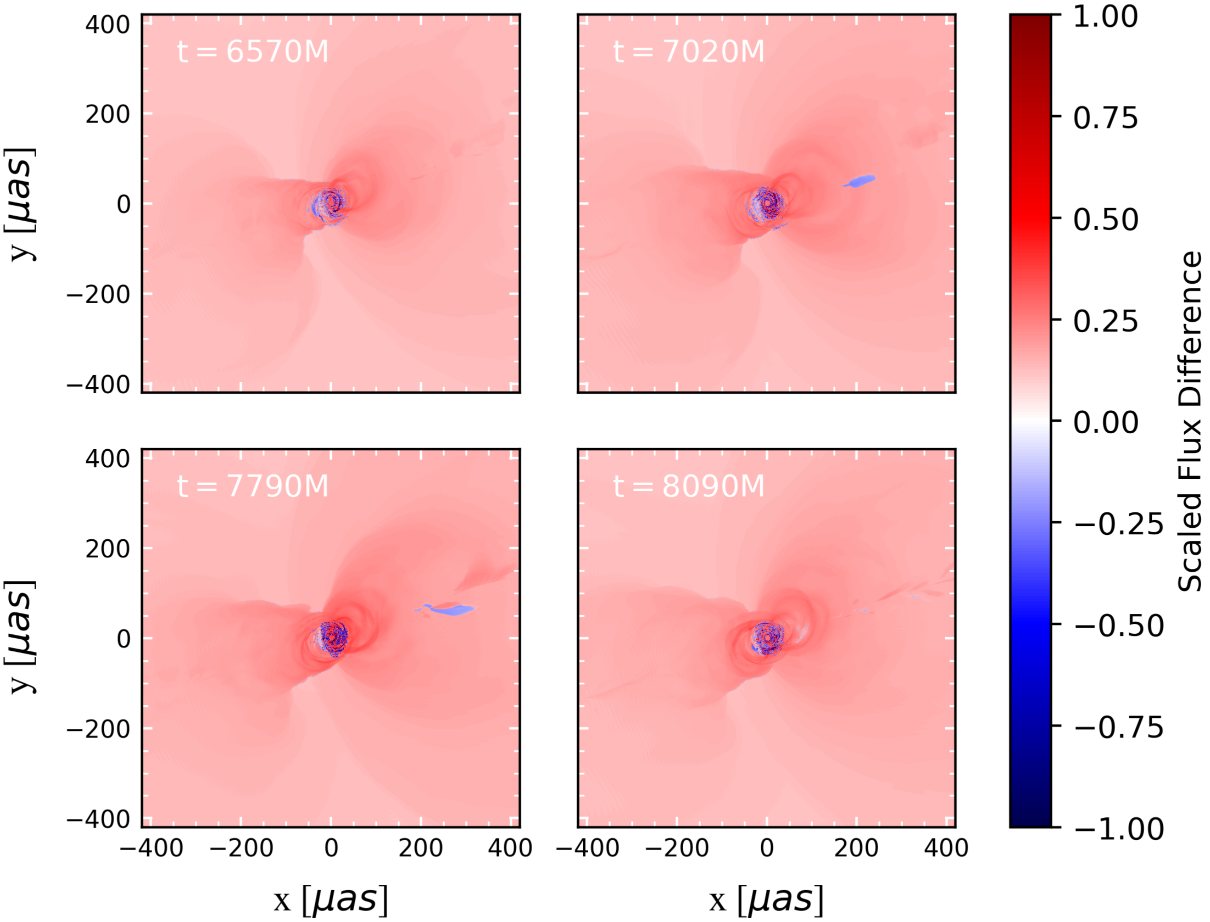

Figure 21: *Difference between the ray-traced thermal and non-thermal images of M87* observed in 43 GHz shown in logarithmic scale. Once again, features from the jet spine can be ignored. Blue areas represent regions where thermal emission dominates while red areas represent greater non-thermal radiation. On smaller scales close to the black hole, the thermal emission is greater than the non-thermal emission, but the non-thermal emission dominates on larger scales.*

In Fig. 21, the stacked difference between Fig. 15 and Fig. 18 is shown, representing the difference between the thermal and non-thermal model at 43 GHz. At small scales close to the black hole, thermal emission is greater than non-thermal emission as shown by the sparse blue region. This result is analogous to Fig. 20. Within compact regions, the thermal models show greater flux density than non-thermal models. However, radiation from the jet, which also overlaps the disk emission on small scales, has much greater radiative power in the non-thermal model. At large scales, radiation from the thermal model is insignificant as shown in Fig. 15, as the thermal emitting region has a finite compact size where the intensity of its radiation drops sharply. Therefore, the non-thermal emission dominates far from the black hole. Non-thermal electrons are required to explain large-scale jets and extended emission regions around accreting black holes. EHT observations at this frequency will have a beam size of roughly $R = 139\,\mu$as, which will confine the thermal-dominated emission within one pixel of observation. Thus, 43 GHz observation can be useful in measuring morphology of large-scale structures created by non-thermal emission, but its utility in observing disk-dominated thermal AGNs is limited. VLBA observations of M87* show a jet beam with resolution 0.43×0.21 mas. The jet is also brightened at the limb, which is not observed in these simulations (Craig Walker et al., 2018). The intensity at the center of the jet can be less than half the intensity of the bright edges. In addition, a region has been observed far from the black hole at 0.5 mas to 2 mas which accelerates particles to mildly superluminal apparent speeds. These are angular sizes which are beyond the width of the image.

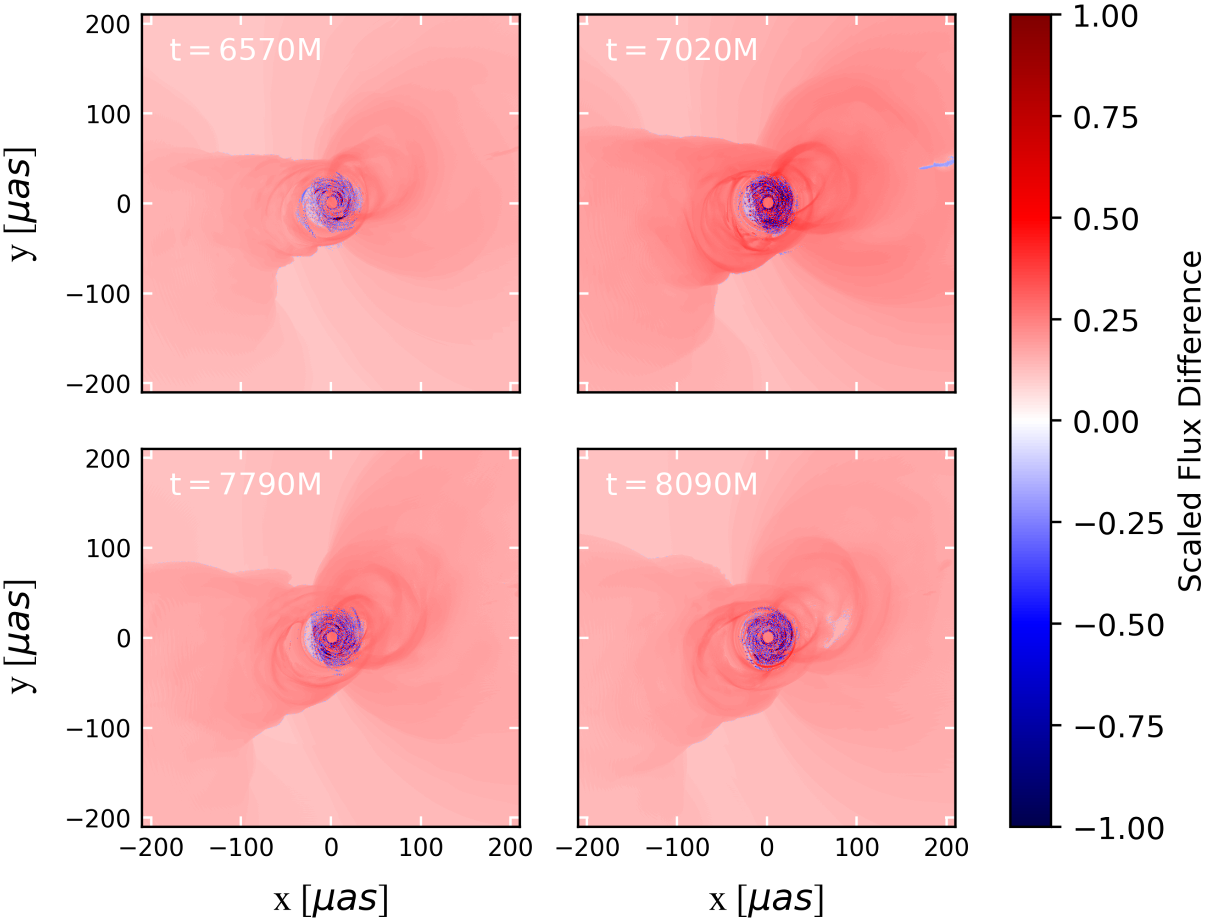

Figure 22: *Difference between the ray-traced thermal and non-thermal images of M87* observed in 86 GHz shown in logarithmic scale. Blue areas represent regions where thermal emission dominates while red areas represent greater non-thermal radiation.*

As with Fig. 21, the image difference at 86 GHz shown in Fig. 22 shows a large-scale non-thermal jet structure with compact thermal emission. While there is observable excess synchrotron radiation at large scales visible in 86 GHz, the effects of non-thermal particles is especially useful in accounting for high energy excess visible in some AGN sources (Romero, Vieyro, and Vila, 2010). The accretion of plasma with large rotational energy from the black hole results in powerful relativistic collimated outflows launched from the stagnation region near the black hole (Bosch-Ramon, 2008; Pu et al., 2017). The existence of the counter-jet shows that the M87* is two-sided when it is launched, which provides evidence against one-sided flip-flop jet models. The brightness ratio between the jet and counter-jet is useful as a measure of the Doppler boosting, which gives a measure of the jet speed. Furthermore, the difference in jet morphology can be related to fundamental dynamical features within the jet and surrounding medium (Craig Walker et al., 2018). GMVA observations of M87* at 86 GHz are consistent with an unseen jet spine, where most of the emission originates from the jet sheath as with the model used here. Furthermore, analysis of the GMVA observations found the jet base opening angle can be as large as $127^\circ \pm 22^\circ$, with the diameter of the jet base between 30 μas to 41 μas, values which are comparable to the diameter of the innermost stable circular orbit. Using this result, it can be inferred that most of the jet launching zone is within the jet sheath of the inner accretion disk. The center to limb ratio obtained in 86 GHz is approximately 0.4, but relative brightness of the center compared to the limb generally increases at longer wavelengths, which suggests that edge-brightening effects are driven by more than the velocity gradient across the jet. Instead, intrinsic differences such as the magnetic field strength and composition in the plasma and jet sheath play a role in the limb-brightening mechanism (Kim et al., 2018).

The comparison of the synthetic images against characteristics shown in actual observations show some of the limitations of ideal GRMHD, which does not consider MHD shocks, electron acceleration mechanisms, cooling, etc. However, the manifestation of the black hole jet powered by strong magnetic fields with the introduction of non-thermal electrons shows that GRMHD is capable of simulating real astrophysically relevant and observable phenomenon despite its various assumptions and limitations. On top of being able to produce synthetic images in frequencies which have already been observed, it is possible to use this model to predict images in frequencies yet to be observed. The GRMHD and GRRT code is used to predict images in the 345 GHz frequency in Section 5.5. Thus, comparison between actual observations and the self-consistent GRMHD and GRRT treatment can be used to refine the models, while the models themselves have the predictive capabilities to investigate physical phenomenon even beyond what may be observable with the limitations of current technology.

As a summary, the following grid of synthetic images show the thermal, non-thermal, and image difference figures, where the left-most panel was created from a purely thermal model and the right-most panel is the image difference. The rows correspond to images of equal time.

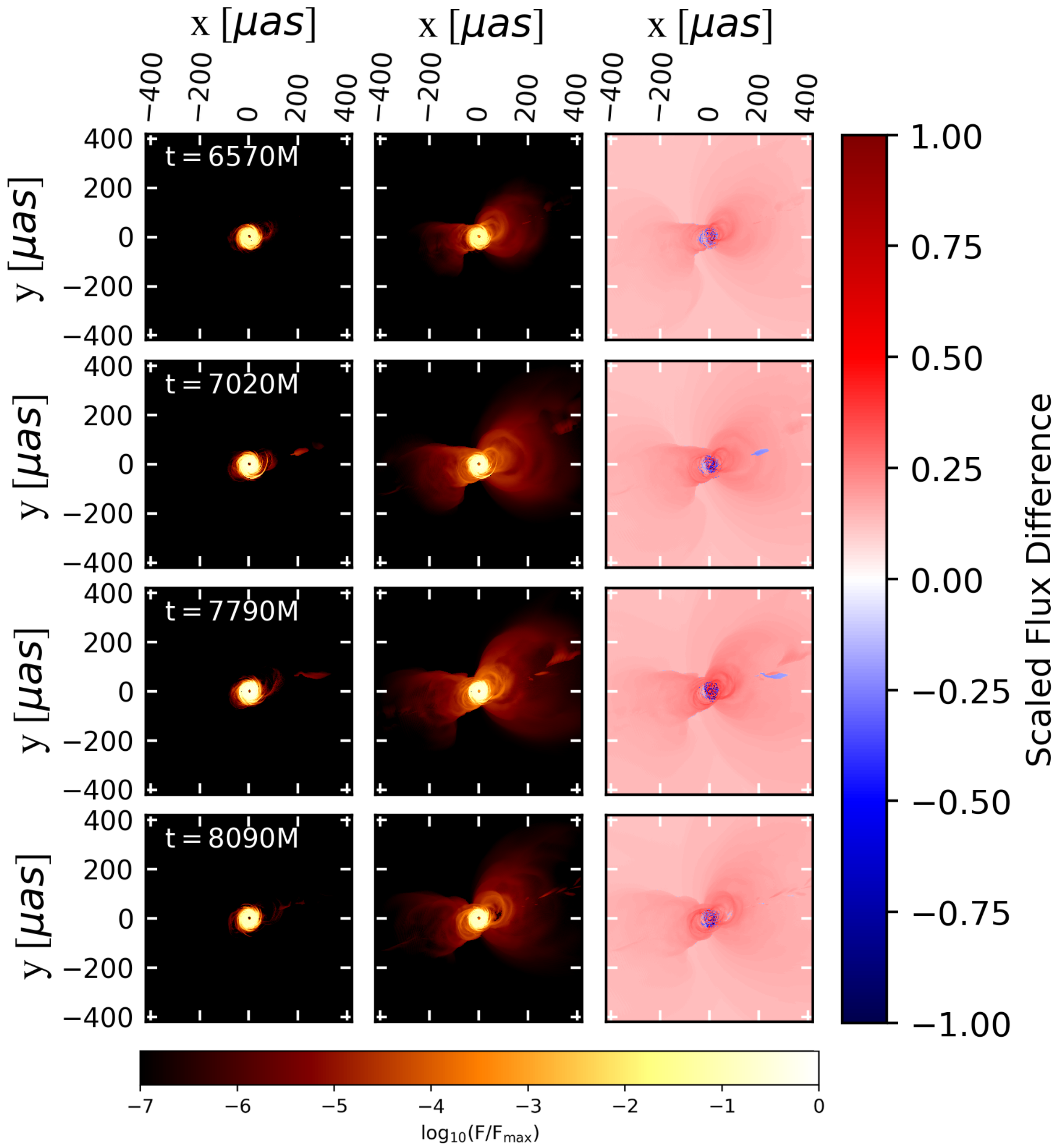

Figure 23: *Summary plot for 43 GHz frequency showing the thermal, non-thermal, and difference images together for all four times. Each row of panels share the same time. The thermal and non-thermal images are scaled according to the horizontal color bar while the image difference plot is scaled according to the vertical color bar.*

In the beginning of the section, it was mentioned that the times chosen to create synthetic images were flux maxima and minima in 230 GHz. In the next section, there is a discussion on the time variability within the thermal and non-thermal models separated by frequency.

5.4 Time Variability

The total specific flux is calculated by summing the flux in each cell from the output of GRRT, keeping in mind that the flux is calculated for an observer located $r = 1000\, r_{\rm g}$ away from the black hole at an observer inclination angle of $\theta_0 = 163°$. Using w as the width of the image, the total specific flux is calculated across the image by

$$F_{\nu,\rm tot} = \sum_{\rm x=0}^{\rm w} \sum_{\rm y=0}^{\rm w} F_\nu(x, y), \tag{73}$$

where $F_\nu(x, y)$ is the specific flux of a single cell. The value for the total flux density is dependent on the location of the observer, specifically the inclination angle. Although the total flux is also dependent on the width of the image, as long as most of the emission features are confined inside the image, then the total flux density represents an accurate representation of the compact flux measured from observation. The thermal and non-thermal images shown in the previous sections show representative images from which the total flux density is computed. In Fig. 15, at an image width of 40 μas, all of the visible thermal emission features in linear scale is confined inside the image dimensions. Knowing that the thermal emission drops sharply beyond its intrinsic source size, including emission outside 40 μas will not change the total flux. One subtlety is that the flux is calculated across the original width of the image w rather than the reduced width $w' \approx 0.64w$. However, given that the brightness outside the reduced width are typically two or more orders of magnitude dimmer than the typical brightness of emission features regardless of thermal or non-thermal model, accounting for these extra cells does not significantly overestimate the total flux represented in the images shown in Sections 5.1 and 5.2.

The shape of the light curve in Fig. 24 can be compared against the mass accretion rate over time in Fig. 7. The corresponding discussion for the mass accretion rate variability argued that between $t = 0$ and $t = 6000M$, the values displayed are the unrealistic results of the imposed Fishbone-Moncrief torus initial conditions. The data shown in the light curve is consistent with that conclusion, as the flux density varies sporadically before settling into a decreasing function of time on average as is expected for SANE. As such, all GRRT images in the previous section have used $t > 6000M$.

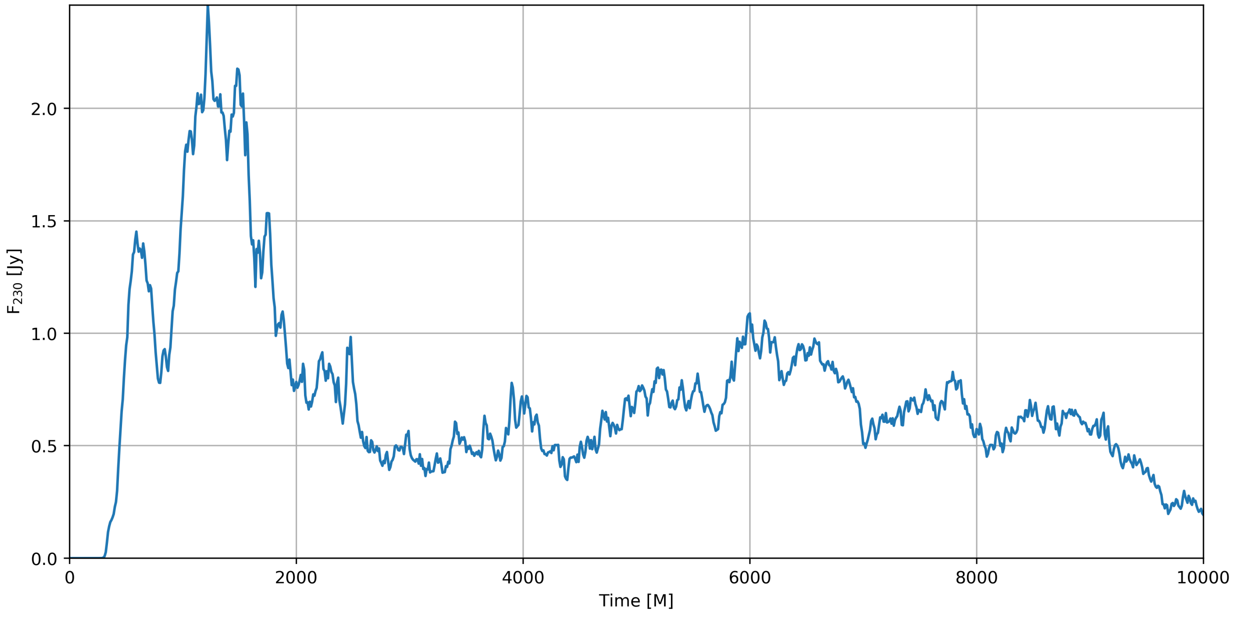

Figure 24: *Full light curve over simulation time for the purely thermal model at 230 GHz observed at* $\theta_0 = 163°$*. The flux density is scaled so that at* $t = 7000M$ *the value is 0.5 Jy.*

EHT results of M87* measured compact flux values between 0.42 Jy and 1.14 Jy on April 5 and 6. The flux was also measured to be between 0.56 Jy and 1.21 Jy on April 10 and 11 (Akiyama, 2019b). To normalise the simulation flux density to the observed results, the code mass accretion rate value has been scaled such that the flux at $t = 7000$ M is 0.5 Jy. The time and value were chosen specifically after the simulation has reached equilibrium and the flux between $t = 6000$ M to $t = 10000$ M is consistent with the observed values. Fluctuations at $t > 6000M$ show time variability which are the result of observable flaring events. Particularly prominent local maxima can be found at times $t = [6570, 7790]\,M$ and their following local minima are $t = [7020, 8090]\,M$. In Fig. 25, the range of $6000\,M < t < 10000\,M$ is shown in greater detail.

Realistically, large flares from black holes are thought to be caused by electron acceleration and heating, initiated by magnetic reconnection events in the core region which releases magnetic energy and carries an outburst of plasma (Khiali, Gouveia Dal Pino, and Sol, 2015). However, magnetic reconnection and electron acceleration are non-ideal effects of GRMHD which are not present in this simulation. The light curve shows that both low-level continuous variability and strong flaring occurs even without magnetic reconnection, MHD shocks, or electron acceleration. The first aspect which governs light curve variability is the mass accretion rate. Large variations in flux are correlated with peaks and troughs in the mass accretion rate as shown by comparing Fig. 7 with Fig. 24, although small-scale variability is much more pronounced in the mass flux. The mass accretion rate fluctuation is caused by turbulence which disrupts the balance between the gravitational pull of the black hole and the magnetic and plasma pressure. Small continuous variability in flux at the sub-mm regime over short time-scales can be attributed to the turbulent accretion flow (Porth, 2019). As shown in the synchrotron power as well as the thermal and non-thermal emissivities, the observed flux is dependent on the pitch angle between the plasma flow and magnetic field vector. Emission is maximised when the electrons trajectory is perpendicular to the magnetic field. This occurs randomly within the turbulent accretion plasma and can generate small detectable variations in flux.

At lower radio frequencies, the time variability is not as pronounced as with 230 GHz. Between $t = 6570\,M$ and $t = 8090\,M$ the flux decreases only 6% in 43 GHz and 1% in 86 GHz, whereas the difference was closer to 54% in 230 GHz. The total flux density also does not change considerably between thermal and non-thermal models. In all scenarios, the total flux density changes by less than 0.5%. Using Fig. 23 as reference, the non-thermal model shows extended jet emission over the purely thermal model, but the total intensity from the source is conserved. From the image difference, it can be seen that by changing the emissivity in the jet sheath from thermal electrons to non-thermal electrons, the flux is redistributed from the central compact region shown in the thermal image to the jet and even beyond the outer edges of the image width. This redistribution of flux and energy is shown by the blue core and red extended emission at large angular scales in the image difference panels, where blue represents greater thermal emission while red represents greater non-thermal emission. The similarity in total flux between the thermal and non-thermal models is mostly the result of two model considerations. First, the thermal electrons are replaced in the jet sheath by the non-thermal electrons instead of an injection of non-thermal electrons. Second, the non-thermal power-law emissivity is considered on its own, rather than added onto the thermal emissivity. Thus, the emission from the disk is purely thermal and the emission from the jet sheath is purely non-thermal, such that the population of thermal and non-thermal electrons do not mix. Table 2 summarizes the results for the thermal and non-thermal models at the three frequencies and four snapshots in time. The fluxes are displayed down to three significant figures of precision.

	F_{43} (Jy)	F_{86} (Jy)	F_{230} (Jy)
t = 6570 M	0.140/0.140	0.326/0.327	0.979/0.979
t = 7020 M	0.134/0.134	0.277/0.278	0.492/0.492
t = 7790 M	0.130/0.130	0.293/0.294	0.831/0.831
t = 8090 M	0.131/0.131	0.322/0.323	0.453/0.453

Table 2: *Total flux density values for the three frequencies (43, 86, 230 GHz) and four separate times (6570, 7020, 7790, 8090 M). In each cell, the value on the left represents the thermal flux density and the value on the right is the flux density for the non-thermal images.*

In Fig. 25, similar structures can be observed between adjacent local maxima and minima in flux density at 230 GHz. Unlike the images generated in the previous discussions, the panels in this figure are all scaled according to a single normalisation value, which is the flux maximum cell of the GRRT image taken at the $t = 7790\,M$ snapshot with the value 9.53×10^{-4} Jy. Then, the flux value is converted into brightness temperature. The flaring events and the flux minima are are marked by the solid red lines. Corresponding emission features which extend beyond the photon ring can be seen between the sequential maximum and minimum snapshots, where the image for the flux maximum shows larger and brighter emission regions as a result of the flaring. For the three frequencies discussed, these flaring structures can only be seen in the high end of the radio spectrum at 230 GHz as the flux density at 43 GHz and 86 GHz remains relatively constant between all four snapshots in time. Fluxes at these frequencies are sometimes called quiescent flux because the time variability is minimal.

Variability timescales are an important aspect to consider for observation. Since M87* is much larger than Sgr A*, variability occurs in days rather than light minutes, allowing it to be observed across a single day without significant worry of changes due to rapid variability. Furthermore variability timescales across radio, ultraviolet, and X-ray light curves can be used to study the energy loss mechanisms and source size of relativistic electron distributions (Harris et al., 2009).

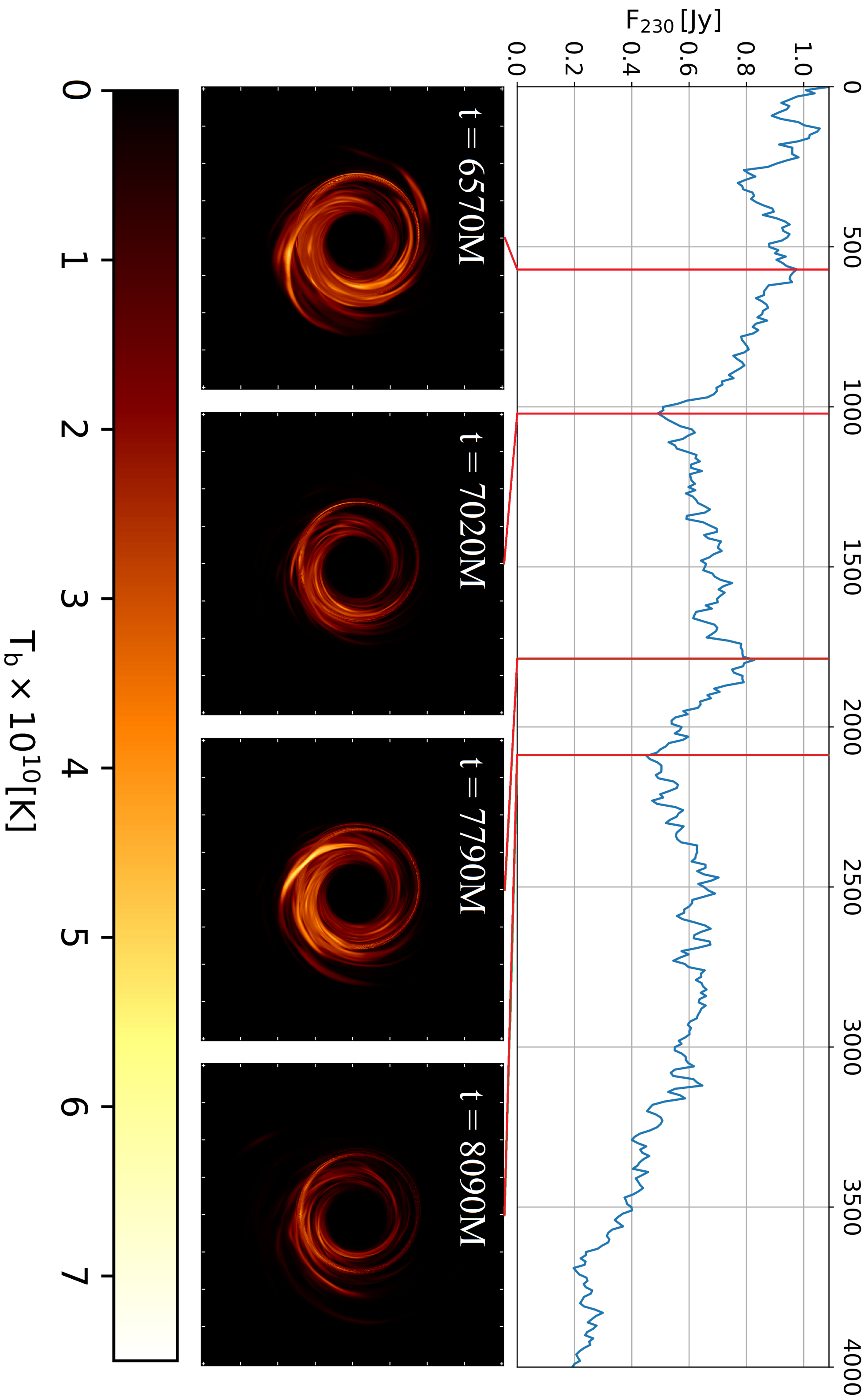

Figure 25: *Light curve beginning at time where $t_0 = 6000\,M$ for a purely thermal model at 230 GHz observed at inclination angle $\theta_0 = 163°$. The stretched light curve improves the visibility of the time variability in flux density. Images were produced at the times which correspond to local maxima and minima and shown with the light curve.*

5.5 Long Term - 345 GHz Observations

Future observations are planned for VLBI in the 345 GHz frequency band. At higher frequencies, the intrinsic size of emission decreases and becomes more optically thin, allowing observations to provide a deeper view of event horizon scale accretion flow. Additionally, the resolution of the images given by $R \propto \lambda/D$ will improve compared to 230 GHz (17 μas compared to 26 μas). Effects of scatter broadening from interstellar electrons will also be reduced by a factor of 2 compared to 230 GHz observations (Doeleman, 2008). At low frequencies, such as 86 GHz, scatter broadening effects dominate the measured intrinsic size of the black hole. At higher frequencies, the accretion plasma does not obscure the view of the black hole shadow. A VLBI reconstructed image in 345 GHz band will contribute a more accurate model of the black hole shadow, which can be used to more tightly constrain the mass and spin of the black hole. Resolving deeper structures will allow us to probe information about the accretion structure and dynamics closer to event-horizon scales.

Presuming the synchrotron model, the spectral energy density for both Sgr A* and M87* turn over at mm wavelengths, which indicates that photons from deep within the gravitational well can escape and that the accretion is optically thin (Akiyama, 2019a). Unlike M87*, Sgr A* has its turnover point at a higher frequency such that observations at 345 GHz are closer to the spectral energy density peak than 230 GHz. Thus, for Sgr A*, not only will the image resolution improve and the scatter broadening effects reduce, but the source is even more optically thin at 345 GHz. However, for M87*, 345 GHz observations are located after the turnover point in the SED as indicated by Fig. 3. Although the same resolution and scatter broadening benefits apply, the source becomes optically thick. When it comes to observing M87*, a balance needs to be struck between the advantages of pushing to higher frequency and the disadvantages in optical depth.

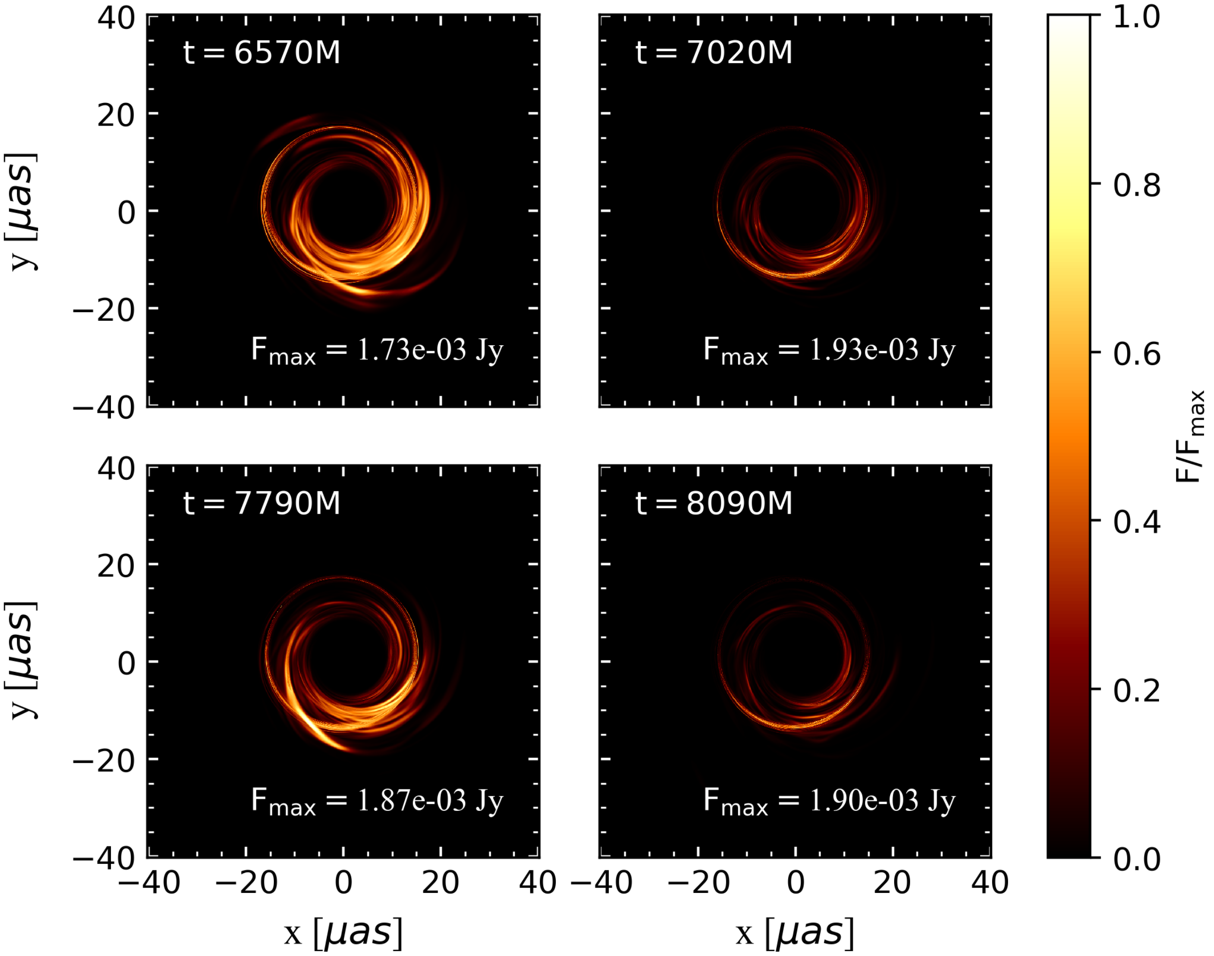

Figure 26: *Ray-traced purely thermal synthetic images of M87* in 345 GHz shown in linear scale. Each image is scaled to the respective flux maximum of that image.*

In increasing order of simulation time, the total flux of these thermal images are [1.133, 0.386, 0.861, 0.307] Jy. Like observations in the 230 GHz frequency, the time variability is much more pronounced, where the flux deviation from $t = 6570\,M$ to $t = 8090\,M$ is almost 73%. However, the flux maximum is nearly enhanced by a factor of 3 compared to their respective 230 GHz images, while the total flux is not considerably different. Instead, the size of the emission regions has decreased and features such as the inner photon ring appear sharper in the image. In addition, there is less plasma obscuring the photon ring. Beam-convolved simulations show that 345 GHz images are significantly less blurred compared to 230 GHz images (Ricarte and Dexter, 2015). Although 345 GHz is located after the turnover point in the M87* SED, observations in the 345 GHz frequency will improve the EHT geometric models of the black hole shadow, providing more precise estimates of the black hole mass and spin parameter. Since the process of reconstructing the EHT image depends on the underlying model used for the black hole, it is important that observations can be made which probe the black hole structure in more than one frequency. Together, the additional data from the 345 GHz can resolve degeneracies in model parameters found between the accretion flow, jet, and photon ring structure which will improve the underlying model.

6 Remarks and Conclusion

The discussion in this thesis was motivated by the recent EHT results on M87*, which captured 230 GHz frequency data and reconstructed an image from an inverse transform of sparse data in Fourier space. These images have allowed for new measurements of black hole mass and spin, independent of gas-dynamical models and stellar orbital trajectories. However, one deliberate limitation in the EHT papers is that only thermal electrons were considered in their models and while thermal electrons can account for most of the observed millimeter wavelength emission, non-thermal electrons are required to explain the power-law tail at high frequencies and low frequency shoulder (Akiyama, 2019c). The non-thermal electrons were emitted because the role of non-thermal electrons in producing the observable compact emission is not yet settled. One of the ways in which the source morphology can be modified by including non-thermal electrons is the lower overall mass accretion rate, which can decrease the visibility of the approaching jet (Dexter, McKinney, and Agol, 2012). In this thesis, non-thermal electrons were injected into the GRRT models without consideration of radiative cooling effects, which have to be treated separately, in order to study a simplified phenomenological model of the non-thermal emission features.

Beginning with Einstein's Field equations to modern day, the properties and characteristics of astrophysically relevant black holes were discussed. Using the no-hair theorem for externally observable characteristics, these uncharged, rotating black holes are called Kerr black holes. Various critical radii of the Kerr black hole were derived from the Kerr metric written in Boyer-Lindquist coordinates. Most relevant to observational efforts and accretion dynamics, the innermost stable circular orbit (ISCO) defines the inner edge of the accretion disk and the radius to the boundary of unstable orbits defines the black hole shadow. An accreting black hole emits radiation with a luminosity that's related to the mass accretion rate by a nominal efficiency parameter. The Eddington luminosity and mass accretion rate define the upper limits on these values. Most black holes are modelled with a two-temperature structure in radiatively inefficient accretion flow (RIAF) and advection dominated accretion flow (ADAF) regimes. The magnetic field is advected into the event horizon by the plasma flow (Akiyama, 2019c), while most of the thermal energy is stored in hot ions which transfer the energy inefficiently to the radiating lower mass electrons. Also shown are two models of black hole accretion evolution: standard and normal evolution (SANE) and magnetically arrested disk (MAD). Under the MAD regime, the advection of magnetic fields into the black hole reach a saturation point in magnetic flux which suppresses mass accretion rate and creates powerful magnetic energy densities which can accelerate plasma away from the black hole in jets. This research thesis only considers GRMHD models under SANE.

The general theory and plausibility behind black hole imaging was also discussed, including why mm wavelengths were ideal for observing M87* and how the EHT is capable of resolving structures on the event-horizon scale. The image was reconstructed using CHIRP and CLEAN algorithms by four independent research teams. After averaging the images together, the EHT result was released to the public on the 10th of April, 2019.

The GRMHD data used is generated by the black hole accretion code (BHAC) (Porth et al., 2017) with a prograde spin parameter $a = 0.96875$. It uses an efficient mesh-based finite volume method with the conservative scheme defined by the well-known equations of GRMHD. The simulations update a set of conserved variables which are calculated as fluxes across the arbitrary spacetime meshed geometry. Then, Riemann solvers are used to recover the primitive variables from the conserved quantities. For initial conditions, a Fishbone-Moncrief rotational equilibrium torus is set up using a constant angular momentum. A weak magnetic field is imposed such that the simulation undergoes SANE for long time periods and the magnetic flux does not saturate. The value of the purely poloidal magnetic field across the initial condition space is determined by the plasma beta. As the simulation begins, the thermal pressure is perturbed by a white noise so that magneto-rotational instability (MRI) develops, which amplifies the magnetic field and powers the accretion dynamics through angular momentum transfer between particles. After some time, a quasi-stationary equilibrium state is reached between the in-flow and out-flow of material. Furthermore, in order to keep the hydrodynamical evolution viable, floor models were imposed in the jet funnel to prevent the density and pressure from dropping to zero. As the simulation develops, snapshots were saved every

$\Delta t = 10\,M$ from $t = 0$ to $t = 10000\,M$.

Using the GRMHD data, flow quantities were calculated in single slices and axisymmetrised slices to show the state of accretion dynamics in time. It was determined from the code mass accretion rate that the simulation becomes real after $t = 6000\,M$, at which point it was assumed that there were no lasting effects from the unrealistic initial conditions. The code mass accretion rate was normalised to create a GRRT image with 0.5 Jy total flux density for an observer at $\theta_0 = 163°$. Flow quantities of density, magnetic field strength, plasma beta, magnetisation, ion temperature, and mass flux were calculated and graphed for the $t = 7000\,M$ slice, which shows the general behaviour of accretion plasma in the black hole vicinity. Also numerical errors resulting from the floor model for density were shown and discussed. By averaging the axisymmetrised data across the θ coordinate and time, the radial profile was constructed for the density, ion temperature, and magnetic field strength, which showed that across the disk, the density follows a r^{-3} relationship far from the black hole, the ion temperature is proportional to r^{-1} and the magnetic field strength is approximately proportional to r^{-2}.

In the GRRT discussion, synchrotron emission was shown to be dominant over Compton scattering and Bremsstrahlung emission at the frequencies of interest. The radiative transfer theory based on Einstein coefficients was discussed and the covariant form of the radiative transfer equation was provided for massless particles. Later, the thermal and non-thermal emissivity and absorptivity coefficients were given. It was decided that the region where the non-thermal electrons were placed must satisfy the magnetisation condition $\sigma < 0.1$ and the hydrodynamical Bernoulli condition $-hu_\mathrm{t} > 1.02$, whereas thermal electrons were considered for GRRT wherever $\sigma < 0.1$ is true, which excises the jet spine and most of the jet funnel from emission. The photon trajectories around black holes was calculated using null geodesics to show how the photons will travel from the black hole to the observer, who is placed at $r = 1000\,r_\mathrm{g}$.

Using the GRMHD data and GRRT considerations in the fast-light approximation, synthetic images were created using BHOSS (Younsi, 2019) with M87* parameters to simulate observed images. Thermal and hybrid non-thermal images were generated for three different frequencies (43 GHz, 86 GHz, 230 GHz) and four time snapshots (6570 M, 7020 M, 7790 M, 8090 M). These specific frequencies were chosen because observations of M87* have already been made by VLBA in 43 GHz, GMVA in 86 GHz, and EHT in 230 GHz. Furthermore, the time snapshots were chosen because at 230 GHz, an observer at $\theta_0 = 163°$ observes flux maxima and minima at those specific simulation times. In general, the thermal images shows compact flux and emission close to the event horizon scale, whereas non-thermal images showed large-scale jets extending beyond the event horizon scale. There was some discussion on how the image width and resolution were kept consistent so that the thermal and non-thermal images could be subtracted cell-by-cell. Then, the image difference was discussed and the general phenomenological results were compared against real observation. The SANE model was not able to account for the wide opening angle and high radiative power of the jet. Furthermore, there were no limb-brightening features which could be observed in the synthetic images. In order for these models to more closely align with observation, the effects of electron acceleration, cooling, and magnetically arrested disks have to be considered.

An analysis of time variability showed that the fluxes at 43 GHz and 86 GHz were in a quiescent state, while the flux maximum and minimum was observable in the 230 GHz frequency. It was also shown that the overall flux density difference between the thermal and non-thermal model was insignificant, showing that replacing thermal electrons with non-thermal electrons in the sheath redistributes flux from the compact source to the jet. In addition, linearly-scaled images were produced which depicted the flaring events in 230 GHz. Finally, possible EHT observations at 345 GHz were discussed, including their theoretical advantages in terms of scatter broadening, optical depth, and resolution. Synthetic images of M87* observed at 345 GHz were also shown to illustrate the advantages. On top of improving image resolution, pushing EHT observations to higher frequencies will circumvent some of the issues regarding scatter broadening from the interstellar medium. Beam convolved simulations show that blurring is significantly less severe in 345 GHz compared to 230 GHz. Despite the higher optical depth in M87*, the sharper image will allow for improved measurements on the photon ring shape and model parameters. More importantly, data from 230 GHz and 345 GHz can mitigate degeneracies between the photon ring structure and the accretion flow. These degeneracies could not be resolved when there is only one observed frequency.

This research thesis has shown that with self-consistent GRMHD and GRRT simulations, hybrid thermal and non-thermal electron models illustrate an improvement over purely thermal models in modelling the observed M87* extended parsec-scale parabolic-shaped jet. However, the SANE regime is unable to replicate the high Lorentz factors for particles nor the wide jet opening angle. In addition parts of the M87* jet emission structure, such as limb-brightening, were not simulated. Some of the ways of improving this model which were discussed involve switching to a MAD accretion regime with radiative cooling and electron acceleration, perhaps with an MHD shock model. The GRMHD model can be expanded to include dissipative processes, such as scalar resistivity, viscosity, pressure anisotropy, and particle acceleration (Akiyama, 2019c). All considered, the effects of non-thermal electrons on the compact emission from black holes is not a fully settled question. Further investigation into the underlying physics and kinetic processes is required.

References

Abbott, B. P. et al. (2016). “Observation of Gravitational Waves from a Binary Black Hole Merger”. In: *Phys. Rev. Lett.* 116.6, p. 061102. DOI: `10.1103/PhysRevLett.116.061102`. arXiv: `1602.03837 [gr-qc]`.

Abramowicz, Marek A. and P. Chris Fragile (2013). “Foundations of Black Hole Accretion Disk Theory”. In: *Living Rev. Rel.* 16, p. 1. DOI: `10.12942/lrr-2013-1`. arXiv: `1104.5499 [astro-ph.HE]`.

Akiyama, Kazunori et al. (2019a). “First M87 Event Horizon Telescope Results. II. Array and Instrumentation”. In: *Astrophys. J.* 875.1, p. L2. DOI: `10.3847/2041-8213/ab0c96`. arXiv: `1906.11239 [astro-ph.IM]`.

— (2019b). “First M87 Event Horizon Telescope Results. IV. Imaging the Central Supermassive Black Hole”. In: *Astrophys. J.* 875.1, p. L4. DOI: `10.3847/2041-8213/ab0e85`. arXiv: `1906.11241 [astro-ph.GA]`.

— (2019c). “First M87 Event Horizon Telescope Results. V. Physical Origin of the Asymmetric Ring”. In: *Astrophys. J.* 875.1, p. L5. DOI: `10.3847/2041-8213/ab0f43`. arXiv: `1906.11242 [astro-ph.GA]`.

— (2019d). “First M87 Event Horizon Telescope Results. VI. The Shadow and Mass of the Central Black Hole”. In: *Astrophys. J.* 875.1, p. L6. DOI: `10.3847/2041-8213/ab1141`. arXiv: `1906.11243 [astro-ph.GA]`.

al., The EHT Collaboration et (2019). “First M87 Event Horizon Telescope Results. I. The Shadow of the Supermassive Black Hole”. In: *ApJL* 875, p. 1. URL: `https://iopscience.iop.org/article/10.3847/2041-8213/ab0ec7`.

Balbus, S. A. and J. F. Hawley (July 1991). “A powerful local shear instability in weakly magnetized disks. I - Linear analysis. II - Nonlinear evolution”. In: *Astrophysical Journal* 376, pp. 214–233. DOI: `10.1086/170270`.

Bardeen, J. M. and J. A. Petterson (Jan. 1975). “The Lense-Thirring Effect and Accretion Disks around Kerr Black Holes”. In: *Astrophysical Journal, Letters* 195, p. L65. DOI: `10.1086/181711`.

Bardeen, J. M., W. H. Press, and S. A. Teukolsky (Dec. 1972). “Rotating Black Holes: Locally Nonrotating Frames, Energy Extraction, and Scalar Synchrotron Radiation”. In: *Astrophysical Journal* 178, pp. 347–370. DOI: `10.1086/151796`.

Bian, Wei-Hao and Yong-Heng Zhao (2003). “Accretion rates and accretion efficiency in agns”. In: *Submitted to: Publ. Astron. Soc. Jap.* arXiv: `astro-ph/0305095 [astro-ph]`.

Bird, Sarah et al. (2010). “The Inner Halo of M87: A First Direct View of the Red-Giant Population”. In: *Astron. Astrophys.* 524, A71. DOI: `10.1051/0004-6361/201014876`. arXiv: `1009.3202 [astro-ph.GA]`.

Blandford, R. D. and R. L. Znajek (May 1977). “Electromagnetic extraction of energy from Kerr black holes”. In: *Monthly Notices of the RAS* 179, pp. 433–456. DOI: `10.1093/mnras/179.3.433`.

Bosch-Ramon, V. (2008). “Powerful non-thermal emission in black-hole powered sources”. In: *Boletin de la Asociacion Argentina de Astronomia La Plata Argentina* 51, pp. 293–304. arXiv: `0910.4412 [astro-ph.HE]`.

Bouman, Katherine L. et al. (Mar. 2016). “Computational Imaging for VLBI Image Reconstruction”. In: *The IEEE Conference on Computer Vision and Pattern Recognition (CVPR*, p. 913. arXiv: `1512.01413 [astro-ph.IM]`.

Bower, Geoffrey C. et al. (2015). “Radio and Millimeter Monitoring of Sgr A*: Spectrum, Variability, and Constraints on the G2 Encounter”. In: *Astrophys. J.* 802.1, p. 69. DOI: `10.1088/0004-637X/802/1/69`. arXiv: `1502.06534 [astro-ph.HE]`.

Carter, B. (Oct. 1968). “Global Structure of the Kerr Family of Gravitational Fields”. In: *Physical Review* 174, pp. 1559–1571. DOI: `10.1103/PhysRev.174.1559`.

Chael, Andrew, Ramesh Narayan, and Michael D. Johnson (2019). “Two-temperature, Magnetically Arrested Disc simulations of the jet from the supermassive black hole in M87”. In: *Mon. Not. Roy. Astron. Soc.* 486.2, pp. 2873–2895. DOI: `10.1093/mnras/stz988`. arXiv: `1810.01983 [astro-ph.HE]`.

Chael, Andrew, Ramesh Narayan, and Aleksander Sadowski (2017). “Evolving Nonthermal Electrons in Simulations of Black Hole Accretion”. In: *Mon. Not. Roy. Astron. Soc.* 470.2, pp. 2367–2386. DOI: `10.1093/mnras/stx1345`. arXiv: `1704.05092 [astro-ph.HE]`.

Chakraborty, Chandrachur, Prashant Kocherlakota, and Pankaj S. Joshi (2017). “Spin precession in a black hole and naked singularity spacetimes”. In: *Phys. Rev.* D95.4, p. 044006. DOI: `10.1103/PhysRevD.95.044006`. arXiv: `1605.00600 [gr-qc]`.

Craig Walker, R. et al. (2018). “The Structure and Dynamics of the Subparsec Jet in M87 Based on 50 VLBA Observations over 17 Years at 43 GHz”. In: *Astrophys. J.* 855.2, p. 128. DOI: `10.3847/1538-4357/aaafcc`. arXiv: `1802.06166 [astro-ph.HE]`.

Cunningham, C. T. and J. M. Bardeen (July 1973). “The Optical Appearance of a Star Orbiting an Extreme Kerr Black Hole”. In: *Astrophysical Journal* 183, pp. 237–264. DOI: `10.1086/152223`.

Dauser, T. et al. (Feb. 2011). “Broad emission lines for a negatively spinning black hole”. In: *Jets at All Scales*. Ed. by G. E. Romero, R. A. Sunyaev, and T. Belloni. Vol. 275. IAU Symposium, pp. 100–101. DOI: `10.1017/S1743921310015735`.

Davelaar, J. et al. (2019). “Modeling non-thermal emission from the jet-launching region of M 87 with adaptive mesh refinement”. In: arXiv: `1906.10065 [astro-ph.HE]`.

Dexter, J., J. C. McKinney, and E. Agol (Apr. 2012). “The size of the jet launching region in M87”. In: *Monthly Notices of the RAS* 421, pp. 1517–1528. DOI: `10.1111/j.1365-2966.2012.20409.x`. arXiv: `1109.6011 [astro-ph.HE]`.

D’Inverno, R. (1992). *Introducing Einstein’s Relativity.* Comparative Pathobiology - Studies in the Postmodern Theory of Education. Clarendon Press. ISBN: 9780198596868. URL: `https://books.google.co.uk/books?id=yqcT3VICuvMC`.

Doeleman, Sheperd et al. (2008). “Event-horizon-scale structure in the supermassive black hole candidate at the Galactic Centre”. In: *Nature* 455, p. 78. DOI: `10.1038/nature07245`. arXiv: `0809.2442 [astro-ph]`.

Einstein, A. (1916). “Die Grundlage der allgemeinen Relativitätstheorie”. In: *Annalen der Physik* 354, pp. 769–822. DOI: `10.1002/andp.19163540702`.

Falcke, H., F. Melia, and E. Agol (Jan. 2000). “Viewing the Shadow of the Black Hole at the Galactic Center”. In: *Astrophysical Journal, Letters* 528, pp. L13–L16. DOI: `10.1086/312423`. eprint: `astro-ph/9912263`.

Finkelstein, David (1958). “Past-Future Asymmetry of the Gravitational Field of a Point Particle”. In: *Phys. Rev.* 110 (4), pp. 965–967. DOI: `10.1103/PhysRev.110.965`. URL: `https://link.aps.org/doi/10.1103/PhysRev.110.965`.

Fishbone, L. G. and V. Moncrief (Aug. 1976). “Relativistic fluid disks in orbit around Kerr black holes”. In: *Astrophysical Journal* 207, pp. 962–976. DOI: `10.1086/154565`.

Frank, J., A. King, and D. Raine (2002). *Accretion Power in Astrophysics.* Accretion Power in Astrophysics. Cambridge University Press. ISBN: 9780521629577. URL: `https://books.google.co.uk/books?id=GGM\_t-xn8ocC`.

Gammie, Charles F., Jonathan C. McKinney, and Gabor Toth (2003). “HARM: A Numerical scheme for general relativistic magnetohydrodynamics”. In: *Astrophys. J.* 589, pp. 444–457. DOI: `10.1086/374594`. arXiv: `astro-ph/0301509 [astro-ph]`.

Gammie, Charles F., Stuart L. Shapiro, and Jonathan C. McKinney (2004). “Black hole spin evolution”. In: *Astrophys. J.* 602, pp. 312–319. DOI: `10.1086/380996`. arXiv: `astro-ph/0310886 [astro-ph]`.

Ghez, A. M. et al. (1998). “High proper motion stars in the vicinity of Sgr A*: Evidence for a supermassive black hole at the center of our galaxy”. In: *Astrophys. J.* 509, pp. 678–686. DOI: `10.1086/306528`. arXiv: `astro-ph/9807210 [astro-ph]`.

Gralla, Samuel E., Daniel E. Holz, and Robert M. Wald (2019). “Black Hole Shadows, Photon Rings, and Lensing Rings”. In: *Phys. Rev.* D100.2, p. 024018. DOI: `10.1103/PhysRevD.100.024018`. arXiv: `1906.00873 [astro-ph.HE]`.

Grenzebach, Arne, Volker Perlick, and Claus Lämmerzahl (2014). “Photon Regions and Shadows of Kerr-Newman-NUT Black Holes with a Cosmological Constant”. In: *Phys. Rev.* D89.12, p. 124004. DOI: `10.1103/PhysRevD.89.124004`. arXiv: `1403.5234 [gr-qc]`.

Harris, D. E. et al. (2009). “Variability Timescales in the M87 Jet: Signatures of E ^{2} Losses, Discovery of a Quasi Period in HST-1, and the Site of TeV Flaring”. In: *Astrophysical Journal* 699.1, pp. 305–314. DOI: `10.1088/0004-637X/699/1/305`. arXiv: `0904.3925 [astro-ph.CO]`.

Israel, Werner (1968). “Event horizons in static electrovac space-times”. In: *Commun. Math. Phys.* 8, pp. 245–260. DOI: `10.1007/BF01645859`.

Issaoun, S. et al. (2019). “The Size, Shape, and Scattering of Sagittarius A* at 86 GHz: First VLBI with ALMA”. In: *Astrophys. J.* 871.1, p. 30. DOI: `10.3847/1538-4357/aaf732`. arXiv: `1901.06226 [astro-ph.HE]`.

Issaoun, S. et al. (2019). “The Size, Shape, and Scattering of Sagittarius A* at 86 GHz: First VLBI with ALMA”. In: *Astrophysical Journal* 871.1, 30, p. 30. DOI: `10.3847/1538-4357/aaf732`. arXiv: `1901.06226 [astro-ph.HE]`.

Janiuk, Agnieszka, Petra Sukova, and Ishika Palit (2018). “Accretion in a Dynamical Spacetime and the Spinning Up of the Black Hole in the Gamma-Ray Burst Central Engine”. In: *Astrophys. J.* 868.1, p. 68. DOI: `10.3847/1538-4357/aae83f`. arXiv: `1810.05261 [astro-ph.HE]`.

Johnson, Michael D. et al. (2017). “Dynamical Imaging with Interferometry”. In: *Astrophysical Journal* 850, 172, p. 172. DOI: `10.3847/1538-4357/aa97dd`. arXiv: `1711.01286 [astro-ph.IM]`.

Kerr, Roy P. (1963). “Gravitational Field of a Spinning Mass as an Example of Algebraically Special Metrics”. In: *Phys. Rev. Lett.* 11 (5), pp. 237–238. DOI: `10.1103/PhysRevLett.11.237`. URL: `https://link.aps.org/doi/10.1103/PhysRevLett.11.237`.

Khiali, Behrouz, Elisabete M. de Gouveia Dal Pino, and Hélène Sol (2015). “Particle Acceleration and gamma-ray emission due to magnetic reconnection around the core region of radio galaxies”. In: arXiv: `1504.07592 [astro-ph.HE]`.

Kim, J. Y. et al. (2018). “The limb-brightened jet of M87 down to 7 Schwarzschild radii scale”. In: [Astron. Astrophys.616,A188(2018)]. DOI: `10.1051/0004-6361/201832921`. arXiv: `1805.02478 [astro-ph.GA]`.

Leung, P. K., C. F. Gammie, and S. C. Noble (Aug. 2011). “Numerical Calculation of Magnetobremsstrahlung Emission and Absorption Coefficients”. In: *Astrophysical Journal* 737, 21, p. 21. DOI: `10.1088/0004-637X/737/1/21`.

Luminet, J.-P. (May 1979). “Image of a spherical black hole with thin accretion disk”. In: *Astronomy and Astrophysics* 75, pp. 228–235.

McKinney, Jonathan C. and Charles F. Gammie (2004). “A Measurement of the Electromagnetic Luminosity of a Kerr Black Hole”. In: *The Astrophysical Journal* 611.2, pp. 977–995. DOI: `10.1086/422244`. URL: `https://doi.org/10.1086%2F422244`.

Menou, Kristen (2005). “Hot accretion with saturated conduction”. In: *Submitted to: Astrophys. J. Lett.* arXiv: `astro-ph/0507189 [astro-ph]`.

Miyoshi, M. et al. (Jan. 1995). “Evidence for a black hole from high rotation velocities in a sub-parsec region of NGC4258”. In: *Nature* 373, pp. 127–129. DOI: `10.1038/373127a0`.

Morgan, C. W. et al. (July 2007). “The Quasar Accretion Disk Size - Black Hole Mass Relation”. In: *ArXiv e-prints*. arXiv: `0707.0305`.

Moscibrodzka, M. and H Falcke (2013). “Coupled jet-disk model for Sgr A*: explaining the flat-spectrum radio core with GRMHD simulations of jets”. In: *Astron. Astrophys.* 559, p. L3. DOI: `10.1051/0004-6361/201322692`. arXiv: `1310.4951 [astro-ph.HE]`.

Moscibrodzka, Monika, Heino Falcke, and Scott Noble (2016). “Scale-invariant radio jets and varying black hole spin”. In: *Astron. Astrophys.* 596, A13. DOI: `10.1051/0004-6361/201629157`. arXiv: `1610.08652 [astro-ph.HE]`.

Nakamura, Masanori and David L. Meier (2014). “A Magnetohydrodynamic Model of The M87 Jet. II. Self-consistent Quad-shock Jet Model for Optical Relativistic Motions and Particle Acceleration”. In: *Astrophys. J.* 785, p. 152. DOI: `10.1088/0004-637X/785/2/152`. arXiv: `1403.3477 [astro-ph.HE]`.

Narayan, Ramesh and Insu Yi (1995). “Advection dominated accretion: Underfed black holes and neutron stars”. In: *Astrophys. J.* 452, p. 710. DOI: `10.1086/176343`. arXiv: `astro-ph/9411059 [astro-ph]`.

Narayan, Ramesh et al. (2012). “GRMHD simulations of magnetized advection-dominated accretion on a non-spinning black hole: role of outflows”. In: *Monthly Notices of the RAS* 426.4, pp. 3241–3259. DOI: `10.1111/j.1365-2966.2012.22002.x`. arXiv: `1206.1213 [astro-ph.HE]`.

Ozel, Feryal, Dimitrios Psaltis, and Ramesh Narayan (Apr. 2000). “Hybrid Thermal-Nonthermal Synchrotron Emission from Hot Accretion Flows”. In: *The Astrophysical Journal* 541. DOI: `10.1086/309396`.

Penna, Robert F., Akshay Kulkarni, and Ramesh Narayan (2013). “A new equilibrium torus solution and GRMHD initial conditions”. In: *Astron. Astrophys.* 559, A116. DOI: `10.1051/0004-6361/201219666`. arXiv: `1309.3680 [astro-ph.HE]`.

Penrose, R and R M. Floyd (Feb. 1971). “Extraction of Rotational Energy from a Black Hole”. In: *Nature* 229, pp. 177–179. DOI: `10.1038/physci229177a0`.

Petrosian, V. (1981). “Synchrotron emissivity from mildly relativistic particles”. In: *Astrophysical Journal* 251, pp. 727–738. DOI: `10.1086/159517`.

Porth, O. et al. (May 2017). “The black hole accretion code”. In: *Computational Astrophysics and Cosmology* 4, 1, p. 1. DOI: `10.1186/s40668-017-0020-2`. arXiv: `1611.09720 [gr-qc]`.

Porth, Oliver et al. (2019). “The Event Horizon General Relativistic Magnetohydrodynamic Code Comparison Project”. In: arXiv: `1904.04923 [astro-ph.HE]`.

Pu, Hung-Yi et al. (2017). “Observable Emission Features of Black Hole GRMHD Jets on Event Horizon Scales”. In: *Astrophys. J.* 845.2, p. 160. DOI: `10.3847/1538-4357/aa8136`. arXiv: `1707.07023 [astro-ph.HE]`.

Quataert, Eliot (2003). “Radiatively inefficient accretion flow models of Sgr A*”. In: *Astron. Nachr.* 324S1, pp. 435–443. DOI: `10.1002/asna.200385043`. arXiv: `astro-ph/0304099 [astro-ph]`.

Ricarte, Angelo and Jason Dexter (2015). “The Event Horizon Telescope: exploring strong gravity and accretion physics”. In: *Mon. Not. Roy. Astron. Soc.* 446, pp. 1973–1987. DOI: `10.1093/mnras/stu2128`. arXiv: `1410.2899 [astro-ph.HE]`.

Romero, G. E., F. L. Vieyro, and G. S. Vila (2010). “Non-thermal processes around accreting galactic black holes”. In: *Astronomy and Astrophysics* 519, A109, A109. DOI: `10.1051/0004-6361/200913663`. arXiv: `1006.5005 [astro-ph.HE]`.

Rosquist, Kjell, Tomas Bylund, and Lars Samuelsson (2009). “Carter’s constant revealed”. In: *Int. J. Mod. Phys.* D18, pp. 429–434. DOI: `10.1142/S0218271809014546`. arXiv: `0710.4260 [gr-qc]`.

Rybicki, G. B. and A. P. Lightman (June 1986). *Radiative Processes in Astrophysics*, p. 400.

Schieven, G. (2018). “Observing with ALMA - a Primer”. In: 1.

Schwarzschild, K. (1916). “On the Gravitational Field of a Mass Point According to Einstein’s Theory”. In: *Abh. Konigl. Preuss. Akad. Wissenschaften Jahre 1906,92, Berlin,1907* 1916.

— (1999). “On the gravitational field of a mass point according to Einstein’s theory”. In: *arXiv e-prints*, physics/9905030, physics/9905030. arXiv: `physics/9905030 [physics.hist-ph]`.

Shibata, Masaru and Yu-ichiou Sekiguchi (2005). “Magnetohydrodynamics in full general relativity: Formulation and tests”. In: *Phys. Rev.* D72, p. 044014. DOI: `10.1103/PhysRevD.72.044014`. arXiv: `astro-ph/0507383 [astro-ph]`.

Shklovsky, I. S. (Apr. 1967). “On the Nature of the Source of X-Ray Emission of Sco XR-1.” In: *Astrophysical Journal, Letters* 148, p. L1. DOI: `10.1086/180001`.

Sironi, Lorenzo, Maria Petropoulou, and Dimitrios Giannios (2015). “Relativistic Jets Shine through Shocks or Magnetic Reconnection?” In: *Mon. Not. Roy. Astron. Soc.* 450.1, pp. 183–191. DOI: `10.1093/mnras/stv641`. arXiv: `1502.01021 [astro-ph.HE]`.

Svensson, Roland (1999). “Old and new advances in black hole accretion disk theory”. In: arXiv: `astro-ph/9902205 [astro-ph]`.

Takahashi, R. (Aug. 2004). “Shapes and Positions of Black Hole Shadows in Accretion Disks and Spin Parameters of Black Holes”. In: *Astrophysical Journal* 611, pp. 996–1004. DOI: `10.1086/422403`. eprint: `astro-ph/0405099`.

Thirring, H. (1918). “Über die Wirkung rotierender ferner Massen in der Einsteinschen Gravitationstheorie.” In: *Physikalische Zeitschrift* 19.

Visser, Matt (2007). “The Kerr spacetime: A Brief introduction”. In: *Kerr Fest: Black Holes in Astrophysics, General Relativity and Quantum Gravity Christchurch, New Zealand, August 26-28, 2004*. arXiv: `0706.0622 [gr-qc]`.

Volonteri, M. et al. (Feb. 2005). “The Distribution and Cosmic Evolution of Massive Black Hole Spins”. In: *Astrophysical Journal* 620, pp. 69–77. DOI: `10.1086/426858`. eprint: `astro-ph/0410342`.

Walsh, Jonelle L. et al. (2013). “The M87 Black Hole Mass from Gas-dynamical Models of Space Telescope Imaging Spectrograph Observations”. In: *Astrophys. J.* 770, p. 86. DOI: `10.1088/0004-637X/770/2/86`. arXiv: `1304.7273 [astro-ph.CO]`.

Younsi Z., et. al. (2019). “Dynamical Covariant General-Relativistic Radiative Transfer”. In:

Younsi, Z., K. Wu, and S. V. Fuerst (Sept. 2012). “General relativistic radiative transfer: formulation and emission from structured tori around black holes”. In: *Astronomy and Astrophysics* 545, A13, A13. DOI: `10.1051/0004-6361/201219599`. arXiv: `1207.4234 [astro-ph.HE]`.

Yuan, Feng and Ramesh Narayan (2014). “Hot Accretion Flows Around Black Holes”. In: *Ann. Rev. Astron. Astrophys.* 52, pp. 529–588. DOI: `10.1146/annurev-astro-082812-141003`. arXiv: `1401.0586 [astro-ph.HE]`.